Climatology of Morphology and Cloud-Radiative Properties of Marine Low-Level Mixed-Phase Clouds

Dissertation

zur Erlangung des
Doktorgrades der Naturwissenschaften (Dr. rer. nat.)

vorgelegt beim **Fachbereich 11 Geowissenschaften / Geographie**
der **Johann Wolfgang Goethe-Universität**
in **Frankfurt am Main**

von
Jessica Danker
aus Frankfurt am Main

Frankfurt am Main (2023)
D30

Vom Fachbereich 11 Geowissenschaften / Geographie der

Johann Wolfgang Goethe-Universität als Dissertation angenommen.

Dekan: Prof. Dr. Jürgen Runge

Gutachter: Dr. Anna Possner, Prof. Dr. Corinna Hoose

Datum der Disputation: 30.11.2023

Disclaimer

I confirm that my dissertation

Climatology of Morphology and Cloud-Radiative Properties of Marine Low-Level Mixed-Phase Clouds

is the result of my own work. No other person's work has been used without acknowledgment in the main text of this dissertation. All sentences or passages quoted in this dissertation from other people's work have been specifically acknowledged by clear cross-referencing to the author and work.

Some chapters and part of chapters of this dissertation are direct citations from my paper *Danker et al.* (2022a) and its supplement *Danker et al.* (2022b). This includes text, tables, and figures. These direct citations have been clearly indicated by a grey font color of the text, including figure and table captions. To fit into the scope of this dissertation, the figure numbers have changed from *Danker et al.* (2022a), and further, some abbreviations have already been defined in previous chapters and have not been redefined. These minor changes have not been marked separately for readability.

Abstract

Marine stratocumuli cover about 40 - 60% of the ocean surface. They self-organize into different morphological regimes. The two organized cellular regimes are called open and closed mesoscale-cellular convective (MCC) clouds. In mid-to-high latitudes, open and closed cells are the two most frequent types of MCC clouds. In particular, many MCC clouds consist of a mixture of vapor, liquid droplets, and ice particles, referred to as mixed-phase clouds (MPCs). Even for the same cloud fraction, the albedo of open cells is, on average, lower than that of closed MCC clouds. Cloud phase and morphology individually influence the cloud radiative effect. Thus, this thesis investigates the relationships between the cloud phase, MCC organization, cell size, and differences regarding the cloud-radiative effect.

This thesis focuses on space-borne retrievals to achieve extensive temporal and spatial coverage. The liDAR-raDAR (DARDAR) version 2 product collocates two active and one passive satellite: CloudSat, Cloud-Aerosol Lidar and Infrared Pathfinder Satellite Observations (CALIPSO), and Moderate Resolution Imaging Spectroradiometer (MODIS). The cloud phase of DARDAR is vertically integrated to establish a single cloud phase at each data point. The MCC classification data set based on the liquid water path (LWP) of MODIS scenes is collocated with the DARDAR product to determine the MCC organization. Cell-size statistics of both MCC clouds are obtained using a marker-based image segmentation method on MODIS reflectance scenes. In addition, based on MODIS reflectance scenes, a convolutional neural network (CNN) is developed to classify open and closed MCC scenes to avoid missing mature MPCs with a low LWP.

The first part of this thesis explores the relationships between cloud phase, morphology, and cloud albedo in the Southern Ocean (SO). At a given cloud-top temperature (CTT), seasonal changes in the mixed-phase fraction, defined as the number of MPCs divided by the sum of MPC and supercooled liquid cloud (SLC) pixels, are stronger than the morphological changes. Therefore, external factors seem to influence these changes instead of morphology. The dependence of cloud phase on cloud-top height (CTH) is more substantial than on CTT in clouds with CTHs below 2.5 km. The previously observed acceleration of closed-to-open transition in MPCs, known as preconditioning, is not the primary driver of climatological cloud morphology statistics in the SO. The morphological differences in cloud albedo are more pronounced in SLCs than in MPCs. This change in albedo alters the cloud radiative effect in the SO by $21\,\mathrm{W\,m^{-2}}$ to $39\,\mathrm{W\,m^{-2}}$ depending on

season and cloud phase.

Open and closed MCC clouds exhibit larger equivalent cell diameters in the MPCs than in SLCs in austral summer, whereas, in austral winter, the SLCs are larger. The cell's aspect ratio accounts for varying CTHs. Closed cells have smaller aspect ratios than open cells, so their cell diameter is smaller, independent of CTH. While the seasonal differences in closed cells are due to changes in CTH, the seasonal aspect ratio differences in open cells are mainly caused by MPCs. With increasing aspect ratios, the cloud albedo decreases in both open and closed MCC clouds, with the most substantial decrease in open MPCs clouds. This leads to cloud-radiative changes of 60 - 75 $\mathrm{W\,m^{-2}}$ in the SO, depending on cloud phase and aspect ratio.

The established CNN exhibits a good accuracy of 80.6%, with even higher accuracies in the Open (85.5%) and Closed (87.3%) categories. The global MCC climatology based on the CNN generally agrees well with previous MCC distributions. The most notable difference occurs in the Northern Hemisphere (NH) in boreal winter, with a higher occurrence frequency of closed and open MCC clouds. This might indicate missing MPCs in previous studies based on the LWP and some restricted to warm cloud scenes. Thus, the developed CNN seems to better represent the different morphologies in MPCs than in previous classifications.

In conclusion, this thesis shows that understanding the dependencies of cloud phase, cloud morphology, and cell size is important to enhance predictions of the cloud-radiative effect and thus, it is important to evaluate how cloud phase, cloud morphology, and cell size change in a warming climate.

Kurzzusammenfassung

Marine Stratocumuli bedecken etwa 40 bis 60% der Meeresoberfläche. Sie organisieren sich selbst in verschiedenen morphologischen Regimen. Die beiden organisierten zellulären Regime werden als offene und geschlossene mesoskalig-zelluläre konvektive (MCC) Wolken bezeichnet. In mittleren bis hohen Breitengraden sind offene und geschlossene Zellen die beiden häufigsten Typen von MCC-Wolken. Viele MCC-Wolken bestehen aus einer Mischung aus Dampf, Flüssigkeitströpfchen und Eispartikeln, die als Mischphasenwolken (MPCs) bezeichnet werden. Selbst bei gleichem Wolkenbedeckungsgrad ist die Albedo offener Zellen im Durchschnitt niedriger als die von geschlossenen MCC-Wolken. Wolkenphase und -morphologie beeinflussen individuell die Strahlungswirkung von Wolken. Daher werden in dieser Arbeit die Beziehungen zwischen der Wolkenphase, der MCC-Organisation, der Zellgröße, sowie deren Unterschieden in der Wolkenstrahlungswirkung untersucht.

Diese Arbeit konzentriert sich auf weltraumgestützte Messungen, um eine umfassende zeitliche und räumliche Abdeckung zu gewährleisten. Das Produkt liDAR-raDAR (DARDAR) Version 2 setzt sich aus zwei aktiven und einem passiven Satelliten zusammen: CloudSat, Cloud-Aerosol Lidar and Infrared Pathfinder Satellite Observations (CALIPSO), und Moderate Resolution Imaging Spectroradiometer (MODIS). Die Wolkenphase von DARDAR wird vertikal integriert, um für jeden Datenpunkt eine einzige Wolkenphase zu erstellen. Der MCC-Klassifizierungsdatensatz, der auf dem Flüssigwasserpfad (LWP) von MODIS-Szenen basiert, wird mit dem DARDAR-Produkt kombiniert, um die MCC-Organisation zu bestimmen. Die Zellgrößenstatistiken beider MCC-Wolken werden mit einer markerbasierten Bildsegmentierungsmethode von MODIS-Reflektanzszenen erstellt. Darüber hinaus wird auf der Grundlage von MODIS-Reflektanzszenen ein faltendes neuronales Netzwerk (CNN) entwickelt, um offene und geschlossene MCC-Szenen zu klassifizieren, um zu vermeiden, dass ausgewachsene MPCs mit einem niedrigen LWP übersehen werden.

Im ersten Teil dieser Arbeit werden die Beziehungen zwischen Wolkenphase, Morphologie und Wolkenalbedo im Südlichen Ozean (SO) untersucht. Bei einer gegebenen Wolkenobergrenzentemperatur (CTT) sind die saisonalen Veränderungen des Mischphasenanteils stärker als die morphologischen Veränderungen. Der Mischphasenanteil ist definiert als die Anzahl der MPCs geteilt durch die Summe der MPC- und SLC-Pixel (unterkühlte (supercooled) flüssig Wolken). Daher scheinen externe Faktoren diese Veränderun-

gen zu beeinflussen und nicht die Morphologie. Die Abhängigkeit der Wolkenphase von der Wolkenobergrenzenhöhe (CTH) ist bei Wolken mit einer CTH von weniger als 2,5 km deutlicher als von der CTT. Die zuvor beobachtete Beschleunigung des Übergangs von geschlossen zu offenen Wolken in MPCs, bekannt als Präkonditionierung, ist nicht der primäre Treiber der klimatologischen Wolkenmorphologiestatistiken im SO. Die morphologischen Unterschiede in der Wolkenalbedo sind in SLCs stärker ausgeprägt als in MPCs. Diese Änderung der Albedo verändert den Strahlungseffekt der Wolken in der SO um $21\,\mathrm{W\,m^{-2}}$ bis $39\,\mathrm{W\,m^{-2}}$ je nach Jahreszeit und Wolkenphase.

Offene und geschlossene MCC-Wolken weisen im Südsommer größere äquivalente Zelldurchmesser in den MPCs als in den SLCs auf, während die SLCs im Südwinter größer sind. Das Seitenverhältnis der Zellen berücksichtigt die unterschiedlichen CTHs. Geschlossene Zellen haben ein kleineres Seitenverhältnis als offene Zellen, so dass ihr Zelldurchmesser unabhängig von der CTH kleiner ist. Während die saisonalen Unterschiede in geschlossenen Zellen auf Veränderungen der CTH zurückzuführen sind, werden die saisonalen Unterschiede im Seitenverhältnis in offenen Zellen hauptsächlich durch MPCs verursacht. Mit zunehmendem Seitenverhältnis nimmt die Wolkenalbedo sowohl in offenen als auch in geschlossenen MCC-Wolken ab, wobei der stärkste Rückgang in offenen MPC-Wolken zu verzeichnen ist. Dies führt zu Wolkenstrahlungsänderungen von $60\text{ - }75\,\mathrm{W\,m^{-2}}$ im SO, je nach Wolkenphase und Seitenverhältnis.

Das entwickelte CNN weist eine hohe Genauigkeit von 80,6% auf, mit noch höheren Genauigkeiten in den Kategorien Offen (85,5%) und Geschlossen (87,3%). Die auf dem CNN basierende globale MCC-Klimatologie stimmt im Allgemeinen gut mit früheren MCC-Verteilungen überein. Der auffälligste Unterschied tritt im Nordatlantik im Nordwinter auf, mit einer höheren Häufigkeit von geschlossenen und offenen MCC-Wolken. Dies könnte darauf hindeuten, dass MPCs in früheren Studien, die auf dem LWP basieren und einige sich auf warme Wolkenszenen beschränken, fehlen. Das entwickelte CNN scheint also die verschiedenen Morphologien in den MPCs besser darzustellen als frühere Klassifikationen.

Zusammenfassend zeigt diese Arbeit, dass das Verständnis der Abhängigkeiten von Wolkenphase, Wolkenmorphologie und Zellgröße wichtig ist, um die Vorhersage des wolkenabstrahlenden Effekts zu verbessern, und dass es daher wichtig ist, zu bewerten, wie sich Wolkenphase, Wolkenmorphologie und Zellgröße in einem sich erwärmenden Klima verändern.

Contents

Disclaimer iii

Abstract v

Kurzzusammenfassung vii

1 Introduction 1
- 1.1 Motivation . . . 1
- 1.2 Theoretical Background . . . 2
  - 1.2.1 Stratocumulus . . . 3
  - 1.2.2 Mesoscale-Cellular Convective Clouds . . . 5
  - 1.2.3 Mixed-Phase Clouds . . . 9
- 1.3 Objectives . . . 13

2 Data and Methods 15
- 2.1 DARDAR and MODIS . . . 15
- 2.2 Vertically Integrated Cloud Phase . . . 16
- 2.3 MCC Classification Dataset . . . 18
- 2.4 MCC Classification with CNN . . . 19
  - 2.4.1 Scene Selection . . . 19
  - 2.4.2 Manual Classification . . . 20
  - 2.4.3 CNN Model . . . 22
  - 2.4.4 Data Augmentation . . . 24
- 2.5 Cell Identification . . . 26
  - 2.5.1 MODIS Scene Preparation . . . 26
  - 2.5.2 Image Segmentation Methods . . . 29
  - 2.5.3 Rejection Rate . . . 35
- 2.6 Global MCC Dataset . . . 36

3 Relations Between Cloud Morphology, Cloud Phase, and Cloud Radiative Effect 37
- 3.1 Stratocumulus Climatology . . . 37
- 3.2 Link of Freezing Behavior and Cloud Phase . . . 43

3.3 Relationship between Cloud Phase, Cloud Morphology, and Cloud Albedo 50

4 Dependence of Cloud Phase and Cloud Albedo on Spatial Scales of MCC Cells 53

4.1 Spatial Scale of MCC Cells and Cloud Phase 53

4.2 Dependence of In-Cloud Albedo on Aspect Ratio 62

5 Global MCC Climatology with CNN 65

5.1 CNN Model Evaluation 65

5.2 Global MCC Climatology 68

6 Conclusions and Outlook 75

6.1 Summary 75

6.1.1 Interplay Between Cloud Morphology, Phase, and Radiative Properties 75

6.1.2 Examining Effects of MCC Cells Spatial Scales 76

6.1.3 Global MCC Climatology with CNN 77

6.2 Conclusions 77

6.3 Outlook 79

Deutsche Zusammenfassung 83

6.4 Zusammenfassung 83

6.4.1 Wechselwirkung zwischen Wolkenmorphologie, Wolkenphase und Strahlungseigenschaften der Wolken 84

6.4.2 Exploration der Auswirkungen der MCC-Zellgröße 85

6.4.3 Globale MCC-Klimatologie mit CNN 86

6.5 Fazit 87

A Supplementary Figures 89

B List of Abbreviations 101

References 103

Acknowledgments 131

Curriculum Vitae 133

1 Introduction

1.1 Motivation

Clouds cover, on average, almost 70% of Earth's surface (*Stubenrauch et al.*, 2013) and roughly account for 30% of the planetary albedo (*Trenberth et al.*, 2009). Due to their vast global coverage, their impact on the hydrological cycle, and their reflection and absorption of incoming shortwave (SW) and outgoing longwave (LW) radiation, clouds play a major role in Earth's climate and radiative balance. Considering the microphysical and dynamical complexity of clouds, no single clouds is alike, and its environmental impacts substantially vary depending on its type or height (e.g., *Arking*, 1991; *Chen et al.*, 2000; *Lohmann et al.*, 2016).

Stratocumuli prevail over the Earth's surface like no other cloud type, covering about 23% of the ocean surface in the annual mean (*Wood*, 2012). These low-level clouds with cloud-top heights (CTHs) up to 3 km exhibit a high cloud albedo (*Randall et al.*, 1984; *Ramanathan et al.*, 1989; *Hartmann et al.*, 1992; *Chen et al.*, 2000). Marine stratocumuli strongly reflect the incoming SW radiation exerting a cooling effect on Earth's climate. In addition, their warming effect in the LW radiation is smaller as cloud-top temperatures (CTTs) of low-level clouds are comparable to surface temperatures, especially in the subtropics. The global mean net cooling effect of low-level stratiform clouds cools the Earth's surface by about $30\,\mathrm{W\,m^{-2}}$ (*Chen et al.*, 2000).

The persistent large decks of marine stratocumuli self-organize into four different morphological regimes: non-organized stratiform clouds, organized open mesoscale-cellular convective (MCC) clouds, organized closed MCC clouds, and disorganized clouds (*Atkinson and Wu Zhang*, 1996; *Wood and Hartmann*, 2006). The two organized morphological regimes, open and closed MCC, occur as roughly hexagonal cells with a typical cell diameter between 10 km to 50 km (*Atkinson and Wu Zhang*, 1996). Whereas closed MCC cells are cloudy at their center, surrounded by an almost cloud-free ring, the reverse occurs in open MCC cells. Due to their morphological differences, the cloud fraction of closed MCC clouds is, on average, about 30% higher than in open cells (*Wood and Hartmann*, 2006). However, *McCoy et al.* (2017) show that even for the same cloud fraction, closed cells exhibit a higher cloud albedo than open cells. This emphasizes the importance of understanding the processes related to the occurrence of the two types of MCC clouds and their transition to quantify their radiative effects on Earth's climate. One process controlling

the transition from closed to open cells is the formation of precipitation (*Feingold et al.*, 2010) leading to a decoupling of the marine-boundary layer (MBL) (*Abel et al.*, 2017). *Yamaguchi and Feingold* (2015) show that not only the onset of precipitation but its spatial extent is essential for the closed-to-open transition in the mid-to-high latitudes. While in the subtropics, the closed-to-open transition is driven by a deepening of the MBL along with the sea surface temperature (SST) gradient with distance to the coast (*Wood and Bretherton*, 2004; *Wood*, 2012). In general, open MCC cells often occur in the wake of marine cold air outbreaks (MCAOs) and cold fronts associated with precipitation formation (e.g., *Brümmer*, 1999; *Fletcher et al.*, 2016a; *McCoy et al.*, 2017; *Geerts et al.*, 2022). MCAOs develop when cold polar air masses over ice sheets are advected to comparatively warm water masses. Cold fronts are the leading edges of low-pressure systems replacing the warm air before the front with colder air behind the front. Further, *Eastman et al.* (2021, 2022) exhibit that a strong increase in surface winds precedes the onset of precipitation in closed-to-open transitions. These morphological transitions due to environmental changes can produce substantial differences in the SW feedback with a quadrupling of CO_2 (*McCoy et al.*, 2023).

The formation of precipitation can depend on the thermodynamic phase of water in clouds. While pure liquid clouds only contain liquid water, mixed-phase clouds (MPCs) consists of a mixture of ice and supercooled liquid water. At high latitudes, many open and closed MCC clouds occur as MPCs. The phase partitioning of ice and supercooled liquid strongly impacts the cloud-radiative effect in stratocumuli (*Sun and Shine*, 1994; *Matus and L'Ecuyer*, 2017; *Korolev et al.*, 2017). Understanding the influence of phase partitioning on the cloud albedo remains uncertain due to the complex microphysics of MPCs (*McCoy et al.*, 2015; *Tan and Storelvmo*, 2019). This causes a poor representation of the cloud feedback in models (*Bony et al.*, 2006; *Zelinka et al.*, 2012, 2013). This is especially important in the Southern Ocean (SO) as the computation of climate sensitivity in this region is critical for the global climate sensitivity (*Gettelman et al.*, 2019; *Zelinka et al.*, 2020). As mixed-phase stratocumuli exhibit extensive coverage at high latitudes, the investigation of open and closed MCC MPCs and their impacts on cloud-radiative properties is the main focus of this thesis, with a particular interest in the SO region.

1.2 Theoretical Background

This section provides a detailed description of the theoretical background on stratocumuli, their dynamical processes, and morphological regimes mentioned in the Motivation. The first section describes the dynamics that drive stratocumuli and the MBL. The key processes of MCC organization in stratocumuli and their transition are illustrated in Sec-

tion 2.3. Finally, MPCs and their importance for the radiative properties of clouds are explained with a focus on the high latitudes of the SO.

1.2.1 Stratocumulus

Stratocumuli stretch over millions of square kilometers horizontally but only exhibit a small vertical extent of 200 - 500 m with CTHs below 3 km (*Driedonks and Duynkerke*, 1989; *Wood*, 2012). In general, 80% of stratocumuli are located over oceans (*Warren et al.*, 1986, 1988), explaining why most studies focus on marine stratocumuli. These thin marine low-level clouds occur at the upper part of the MBL, which is capped by a temperature inversion often accompanied by a moisture inversion (*Lilly*, 1968; *Lock*, 2009; *Sedlar and Tjernström*, 2009; *Solomon et al.*, 2011). The strength of large-scale subsidence affects the height and intensity of the inversion (*Randall et al.*, 1984; *Wood*, 2007; *Van Der Dussen et al.*, 2016). The key processes driving marine stratiform boundary layer clouds are illustrated in Fig. 1. The main driver of turbulence in the MBL is LW radiative cooling close to the cloud top (*Lilly*, 1968; *Moeng et al.*, 1996; *Mellado*, 2017). The turbulence generated by cloud-top cooling homogenizes the cloud layer through the overturning circulation in the cloud. Further, if strong enough, the turbulent mixing can lead to a well-mixed MBL coupled to the ocean surface and, thus, moisture supply (*Bretherton and Wyant*, 1997). An additional source of turbulent mixing is induced by latent heating in the warm updrafts due to condensation and by evaporative cooling in the downdrafts (*Moeng et al.*, 1992). In contrast, the SW solar heating reduces the strength of turbulent mixing by counteracting cloud-top cooling. Marine stratocumuli often produce light precipitation as drizzle or in MPCs as ice or snow (*Wood*, 2005; *Leon et al.*, 2008; *Morrison et al.*, 2012).

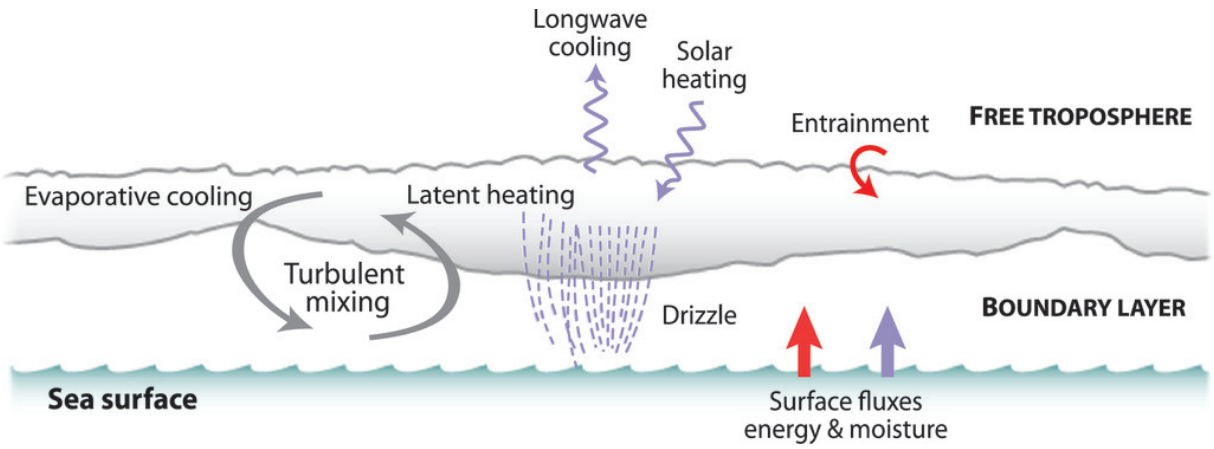

FIG. 1 Schematic representation of processes influencing the dynamics of the stratocumulus cloud deck. This figure is Fig. 2 from *Wood* (2012).

Due to the main dynamical processes, marine stratocumuli preferentially occur in regions of large-scale subsidence, strong lower-tropospheric stability, and with a great supply of surface moisture (e.g., *Wood and Bretherton*, 2006; *Sun et al.*, 2011; *Wood*, 2012). Regions of large-scale subsidence are typically connected to the general circulation or large-scale meteorological phenomena (*Bretherton and Hartmann*, 2009). The downward branches of the Hadley cells and the Walker circulation induce large-scale subsidence in the subtropics, while in the mid-latitudes, subsidence is associated with high-pressure systems or in the wake of cold fronts (*Norris*, 1998; *Norris and Klein*, 2000). The lower-tropospheric stability is defined as the potential temperature difference between 700 hPa and 1000 hPa (*Klein and Hartmann*, 1993) which is related to the inversion strength and thus, to cloud-top cooling. It is particularly strong over the cold eastern parts of the subtropical oceans (*Wood and Hartmann*, 2006). Due to the strong air-sea temperature difference in MCAOs, the energy and moisture surface fluxes increase in the MBL, favoring the occurrence of marine stratocumuli (*Brümmer*, 1999; *Abel et al.*, 2017; *Fletcher et al.*, 2016a,b; *McCoy et al.*, 2017). As a result of the link to the winter storms and MCAOs, the occurrence frequency of stratocumuli depends on the season and is, in general, higher in the winter months of the respective hemisphere (*Klein and Hartmann*, 1993; *Wood*, 2012). In addition, the seasonal cycle of stratocumuli reflects the seasonal changes in the lower-tropospheric stability (*Klein and Hartmann*, 1993; *Wood and Bretherton*, 2006).

The cloud albedo directly depends on the cloud optical thickness (COT) and, thus, the liquid water path (LWP) and cloud droplet number concentration (*Liou*, 1992; *Boucher and Rodhe*, 1994; *Boucher and Lohmann*, 1995). The increase of cloud albedo by an increase in the cloud droplet concentration due to more cloud condensation nuclei is known as the Twomey effect (*Twomey*, 1974, 1977). Thus, the contribution to the radiative effect from even small perturbations of COT in stratocumulus can be substantial (*Hartmann and Short*, 1980; *Randall et al.*, 1984). Due to their high cloud albedo particularly in comparison to the ocean surface, marine stratocumuli strongly reflect the incoming SW radiation and exert a cooling effect (*Randall et al.*, 1984; *Ramanathan et al.*, 1989; *Hartmann et al.*, 1992; *Chen et al.*, 2000). However, especially at high latitudes over sea ice and due to the absence of sunlight, the contrast between the clouds and the surface reduces and, thus, their cooling effect (*Ramanathan et al.*, 1989). The influence of the outgoing LW radiation which exhibits a warming effect, is considerably lower than the SW cooling effect due to the comparable temperature of the cloud-free MBL and the cloud tops (*Chen et al.*, 2000). This leads to a mean global net cooling effect of stratocumulus cloud of about $30\,\mathrm{W\,m^{-2}}$.

There are multiple processes leading to the dissipation or break up of marine stratocumuli. One is through cloud thinning and the dissolution of the cloud, which can be

initiated by strong large-scale subsidence lowering the inversion (*Randall and Suarez*, 1984; *Sundararajan and Tjernström*, 2000; *Van Der Dussen et al.*, 2016; *Young et al.*, 2018), moisture limitations due to a decoupling from the surface (*Bretherton and Wyant*, 1997), or cloud top entrainment of dry air above the inversion (*Randall et al.*, 1984; *Xiao et al.*, 2010). Another is through the transition from stratocumulus to cumulus clouds which can be initiated by the cloud thinning processes and further by weaker lower-tropospheric stability (*Klein and Hartmann*, 1993; *Wood and Bretherton*, 2006), an increase in the ambient concentration of aerosols (*Wood et al.*, 2011; *Xue et al.*, 2008), and the onset of precipitation which leads to a decoupling of the MBL (*Abel et al.*, 2017). The stratocumulus-to-cumulus transitions can be interpreted as the evolution of different MCC clouds in the subtropics (*Wood*, 2012).

1.2.2 Mesoscale-Cellular Convective Clouds

Marine stratocumuli self-organize into four different morphological regimes, which are detected by satellite images since their first observations in 1960 (*Krueger and Fritz*, 1961; *Agee et al.*, 1973; *Agee*, 1987). These four different morphological types are non-organized stratiform clouds, organized open MCC clouds, organized closed MCC clouds, and disorganized clouds. All four regimes are shown in a satellite image of Moderate Resolution Imaging Spectroradiometer (MODIS) Aqua of the SO in Fig. 2. The focus of this thesis is on the two organized MCC regimes of open and closed MCC clouds with distinct cells which are associated with different cloud fractions (*Agee*, 1987; *Atkinson and Wu Zhang*, 1996; *Wood and Hartmann*, 2006). The typical cell diameter of MCC clouds is 10 - 50 km.

The conceptual diagram of the dynamic and radiative processes in forming closed and open cells is displayed Fig. 3. Closed MCC cells feature cloudy cell centers of rising warm air surrounded by almost cloud-free rings of sinking air when viewed from the top by satellites (e.g., *Agee et al.*, 1973; *Atkinson and Wu Zhang*, 1996; *Wood and Hartmann*, 2006). Due to their high cloud fraction, closed cells exhibit substantial radiative cooling near the cloud top. This drives the vertical overturning circulation with localized narrow downdrafts surrounding the cell and weak broad updrafts at the cell center. Due to adiabatic cooling, the air condensate at the upper parts of the updrafts forming the cloud. The closed cells are approximately stationary in the absence of precipitation and only shift with the mean flow (*Glassmeier and Feingold*, 2017). Thus, closed MCC clouds are more stratiform, preferentially occur over relatively cool oceans with strong lower-tropospheric stability, and are mainly sustained by cloud-top radiative cooling (*Helfand and Kalnay*, 1983).

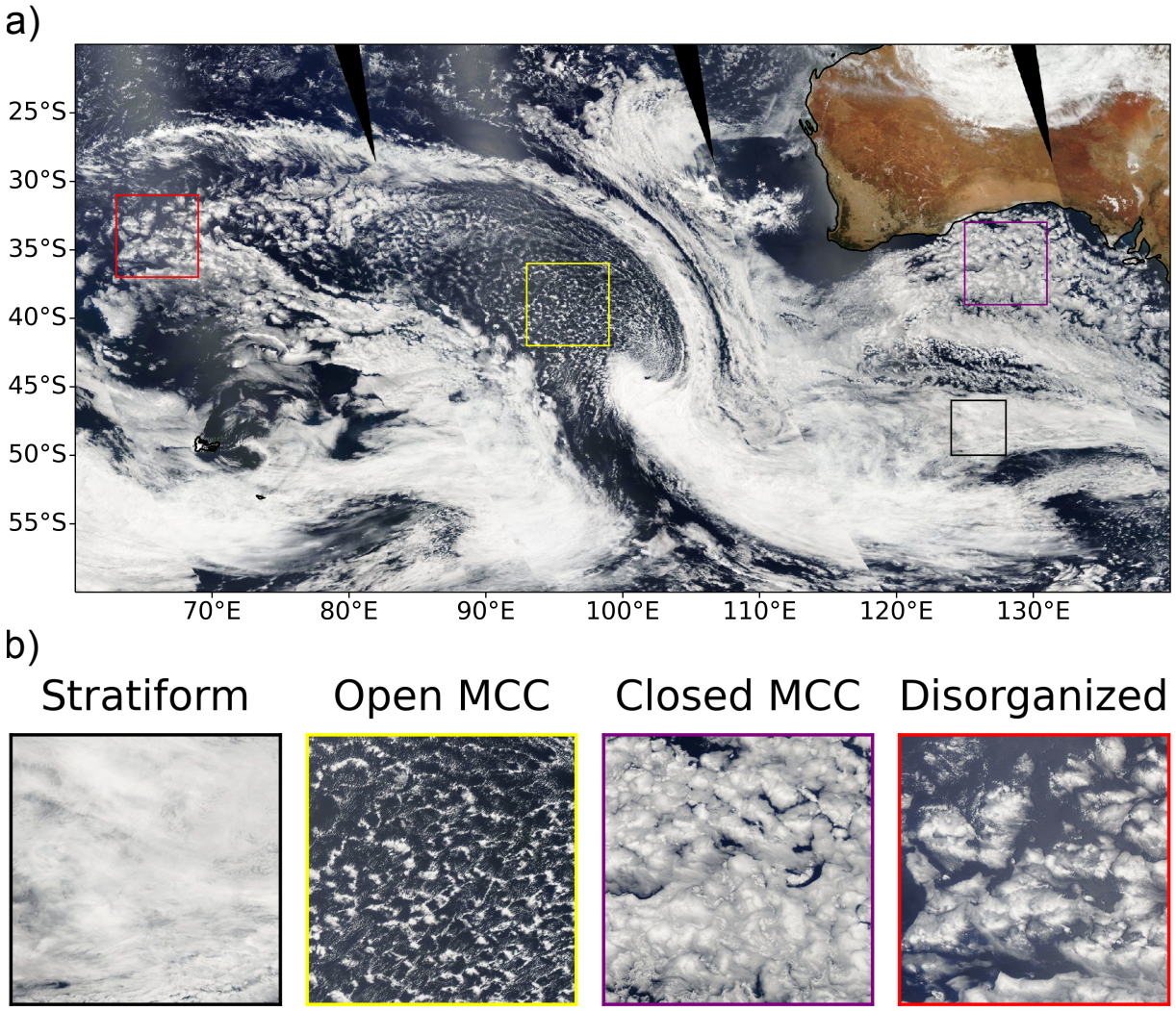

FIG. 2 (a) True color image of the SO from MODIS instrument on the Aqua satellite taken on January 5th 2023 (provided by: `https://earthdata.nasa.gov`). (b) The visual inspection identifies four organizational regimes in low-level clouds. The stratiform box has a size of 4°×4°, all other boxes have a size of 6°×6°.

In contrast, open MCC clouds exhibit narrow cloudy cell rings of rising air surrounded by almost cloud-free centers with sinking air viewed from the top. The strongest narrow updrafts merge at the intersections of typically three open cells (Fig. 3 b). Due to the stronger updrafts in open MCC cells compared to closed MCC clouds, the clouds are generally deep enough to generate precipitation (mean thickness 600 m and up to 2 km (*Jensen et al.*, 2021)). The evaporative cooling in the subcloud layer through precipitation leads to the formation of cold pools near the surface. The expanding cold pools from neighboring cells collide, enhancing the updrafts or forming new ones (*Glassmeier and Feingold*, 2017). Thus, while closed cells are more stationary, the formation of open cells is more oscillatory, where the dissipating old cells stimulate the development of new cells. Open MCC clouds are more cumulus-like, associated with stronger surface heat fluxes,

and mainly occur over relatively warm oceans in contrast to air temperature (*Helfand and Kalnay*, 1983; *Agee et al.*, 1973).

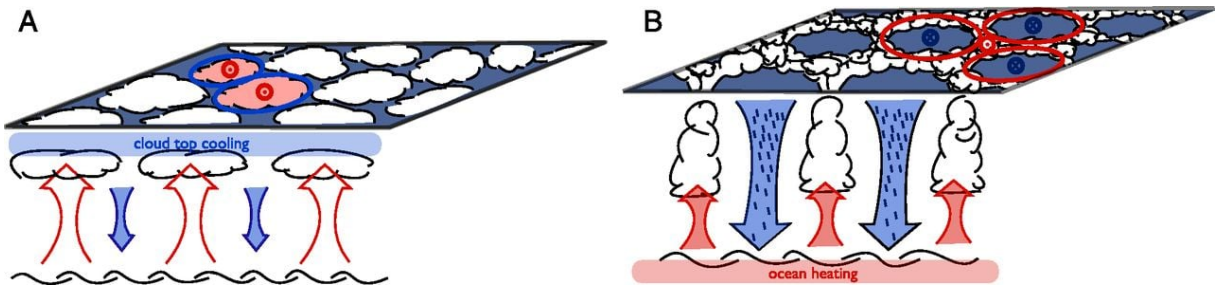

FIG. 3 Conceptual diagram of dynamic and radiative processes in (a) closed and (b) open MCC clouds. Red arrows and ⊙ indicate updrafts, while blue arrows and ⊗ display downdrafts. This figure is Fig. 1 from *Glassmeier and Feingold* (2017).

In general, based on their region of formation, both open and closed MCC organizations can be grouped into two types: (1) over relatively cold upwelling regions in the eastern parts of the tropical to subtropical oceans and (2) in MCAOs with strong air-sea temperature difference driving heat and moisture transport in the mid to high latitudes or the passage of extra-tropical cyclones (*Agee*, 1987; *Noteboom*, 2007). The first type is mainly driven by cloud-top radiative cooling and, thus, primarily associated with closed MCC cells near the west coast of continents. At the same time, open MCC clouds occur farther off the coast with increasing MBL heights and SSTs. On the other hand, the second type is dominated by strong surface fluxes due to the advection of cold air over relatively warm water masses. During MCAOs, the clouds usually first form roll-like cloud streets, which transition predominately into open MCC cells and sometimes, due to stronger subsidence, into closed MCC clouds (*Brümmer*, 1999; *Atkinson and Wu Zhang*, 1996). While MCAOs are stronger and larger in the Northern Hemisphere (NH), in the Southern Hemisphere (SH), they also occur frequently (*Fletcher et al.*, 2016a). Even though MCAOs occur in all seasons, their occurrence frequency, intensity, and spatial scale peaks in boreal winter (December to January (DJF)) in the NH, while the occurrence frequency in austral winter (June to August (JJA)) in the SH is comparable to fall (NH: September to November (SON), SH: March to May (MAM)) or spring (NH: MAM, SH: SON) in either hemisphere (*Fletcher et al.*, 2016a). Due to the different driving forces in open and closed MCC cells, open and closed MCC peak in different seasons. While open cell occurrence peaks in winter, especially in the storm tracks, closed cells occur more frequently in summer and increase with latitude (*Muhlbauer et al.*, 2014; *McCoy et al.*, 2017).

Due to the organizational differences in open and closed MCC clouds, closed MCC clouds exhibit, on average, a 30% higher cloud fraction than open cells (*Wood and Hartmann*, 2006), leading to a higher reflection of incoming SW radiation of closed MCC

clouds. However, even for the identical cloud fraction, the cloud albedo of closed MCC clouds is larger than that of open cells (*McCoy et al.*, 2017). This emphasizes the importance of understanding the transition of closed and open MCC clouds.

The two mechanisms of closed-to-open transition investigated most are cold air advection over warmer water and cloud–aerosol–precipitation interactions (*Yamaguchi and Feingold*, 2015). While the former is connected to the passage of cyclone and MCAOs (*Muhlbauer et al.*, 2014; *Fletcher et al.*, 2016b; *McCoy et al.*, 2017), already discussed above, the latter is connected to the onset of precipitation through microphysics (*Wang and Feingold*, 2009a,b; *Feingold et al.*, 2010). The formation of precipitation in closed MCC clouds leads to cloud thinning and break up of the cloud. At the same time, localized precipitation can initiate the formation of cold pools near the surface. These cold pools expand and collide near the surface, producing new updrafts and enhancing the surface fluxes. These newly formed updrafts drive the cloud rings of open MCC clouds (*Berner et al.*, 2013; *Wood et al.*, 2011). However, *Yamaguchi and Feingold* (2015) show that while precipitation is a necessary condition for closed-to-open transition, it is insufficient. Further, the spatial extent of precipitation seems to be essential for the transition from open to closed MCC clouds. *Abel et al.* (2017) show that the key process in the transition is due to a decoupling of the boundary layer induced by precipitation which depletes the LWP. In addition, aerosols can suppress precipitation in open and closed MCC clouds, influencing the transition (*Rosenfeld et al.*, 2006; *Xue et al.*, 2008). Due to aerosol perturbations, e.g., through ship tracks or advection of continental air masses, the reversed transition from open-to-closed MCC can occur (*Goren and Rosenfeld*, 2012; *Feingold et al.*, 2015). However, the reverse transition is slower, more complex, and requires the suppression of precipitation in open cells. Precipitation suppression can also be induced by stronger subsidence, reducing the cloud thickness and, thereby, precipitation formation (*Berner et al.*, 2013). *Eastman et al.* (2021, 2022) show that the closed-to-open transition is a two-step process in which the onset of precipitation is preceded by strong surface winds. This is supported by *Jensen et al.* (2021) exhibiting stronger surface winds in open MCC cells. A recent study by *McCoy et al.* (2023) reveals that these morphological transitions due to environmental changes can produce substantial differences in the SW feedback with a quadrupling of CO_2.

As closed-to-open transitions are strongly influenced by precipitation, ice processes in clouds are important as they strengthen the precipitation (*Field and Heymsfield*, 2015). In MCAOs in the mid to high latitudes, these clouds often occur as MPCs with temperatures below 0 °C (*Abel et al.*, 2017). Especially in the SO, open MCC clouds commonly occur as MPCs (*Lang et al.*, 2021), which frequently drizzle (*Ahn et al.*, 2017) and are influenced by secondary ice processes (*Huang et al.*, 2017). Moreover, simulations show precipitation

tends to increase horizontal scales (*Zhou et al.*, 2018) and cold pools, in particular in clouds with high ice water paths (IWPs) (*Eirund et al.*, 2019a).

1.2.3 Mixed-Phase Clouds

Mixed-phase clouds (MPCs) contain a mixture of supercooled liquid droplets, water vapor, and ice crystals (e.g., *Shupe et al.*, 2008; *Lohmann et al.*, 2016; *Korolev et al.*, 2017, and references therein). At temperatures below 0 °C, cloud droplets can remain as supercooled liquid droplets until −38 °C, at which homogeneous nucleation starts to occur without any foreign substance (*Vali et al.*, 2015). Warm clouds, which are purely liquid, occur at temperatures above 0 °C, while supercooled liquid clouds (SLCs) with CTTs below 0 °C can either consist of warm liquid and supercooled liquid cloud droplets or only supercooled droplets. As a result, MPCs and SLCs are confined to a temperature range from 0 °C to −38 °C and occur throughout the year in mid-to-high latitudes.

The important microphysical processes in MPCs are displayed in Fig. 4. In contrast to homogeneous freezing, heterogeneous freezing requires an ice nucleating particle (INP). An INP is needed as it reduces the energy barrier for ice formation and, thus, occurs at a lower supersaturation (e.g. *Schaefer*, 1946; *Vonnegut*, 1947; *Seinfeld and Pandis*, 2006; *Lohmann et al.*, 2016; *Vali et al.*, 2015). Heterogeneous nucleation can occur through four different modes (*Vali*, 1985; *Pruppacher et al.*, 1998). *Deposition nucleation* refers to ice nucleation directly from supersaturated vapor without a preceding liquid phase. However, with an improvement in observational capabilities, it is suggested that depositional nucleation involves pore condensation and freezing of water in tiny cavities of INPs that are not detectable macroscopically (*Marcolli*, 2014; *David et al.*, 2019; *Marcolli et al.*, 2021). *Condensation freezing* occurs when water vapor condenses on the surface of the INP and freezes subsequently. The freezing that is initiated due to the collision of an INP with a supercooled liquid cloud droplet is called *contact freezing*. Finally, *immersion freezing* refers to the freezing of an already immersed INP in a cloud droplet and seems to be the most important mode in MPCs (*Westbrook and Illingworth*, 2011; *Hande and Hoose*, 2017).

In particular, in the SO, the INP concentration is lower than in other regions and a factor 100 lower than historically thought (*McCluskey et al.*, 2018). In addition, the INP concentration is inferior to the in-cloud ice number concentration (*Sullivan et al.*, 2018). This discrepancy can be explained by secondary ice processes involving preexisting ice, which multiplies and acts as INPs in heterogeneous nucleation. In a review paper of *Korolev and Leisner* (2020), six different secondary ice processes are identified: (1) rime-splintering (Hallett–Mossop) process (*Hallett and Mossop*, 1974), (2) break-up due to

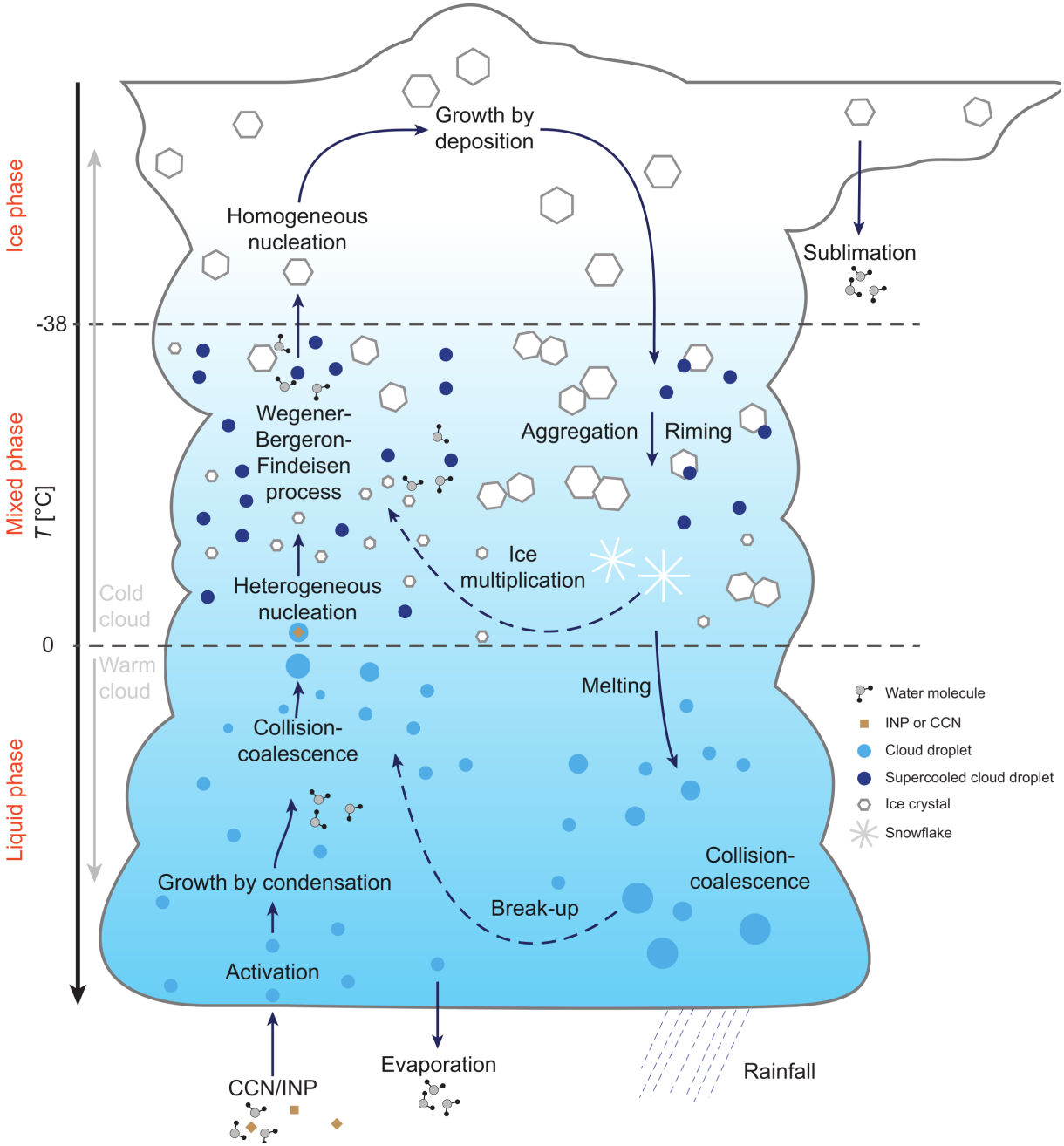

FIG. 4 Schematic of microphysical processes in warm-, mixed-, and ice-phase temperature regimes. This figure is the colored version of Fig. 8.19 from *Lohmann et al.* (2016).

ice-ice collision (*Takahashi et al.*, 1995; *Riley and Mapes*, 2009; *Mignani et al.*, 2019), (3) droplet shattering during freezing (*Korolev et al.*, 2004; *Rangno*, 2008; *Korolev et al.*, 2020), (4) fragmentation due to thermal shock (*Dye and Hobbs*, 1968), (5) fragmentation of sublimating ice (*Oraltay and Hallett*, 1989), and (6) activation of INPs around freezing drops in transient supersaturation (*Muchnik and Rudko*, 1961; *Dye and Hobbs*, 1968). These six processes of secondary ice formation are displayed in Fig. 5. Out of these six,

the first three are most investigated and seem to be most important in natural cloud environments (e.g., *Libbrecht*, 2005; *Mignani et al.*, 2019; *Sullivan et al.*, 2018; *Silber et al.*, 2021a). The relevance of secondary ice processes is temperature-dependent, as different secondary ice processes occur at different temperatures.

Once an ice crystal is formed through primary or secondary ice processes, ice crystals grow at the expense of the supercooled liquid cloud droplets (*Wegener*, 1911). This is due to the different equilibrium water vapor pressures, which are lower over ice crystals than liquid droplets. This process is part of the Wegener-Bergeron-Findeisen (WBF) mechanism (*Wegener*, 1911; *Bergeron*, 1935; *Findeisen*, 1938). In addition, ice crystals can also grow through collisions with liquid droplets which freeze upon contact referred to as riming. For ice crystals to grow sufficiently to generate precipitation, the ice number concentration in MPCs needs to be much lower than that of liquid cloud droplets (*Bergeron*, 1935; *Findeisen*, 1938). Thus, in general, the in-cloud ice number concentration is much lower than the droplet number concentration in MPCs and, thus, the IWP is lower than the LWP. Therefore, the WBF process converts supercooled liquid to ice and eventually causes the MPCs to glaciate fully unless there is enough cooling or moistening to maintain the saturation (*Korolev et al.*, 2017).

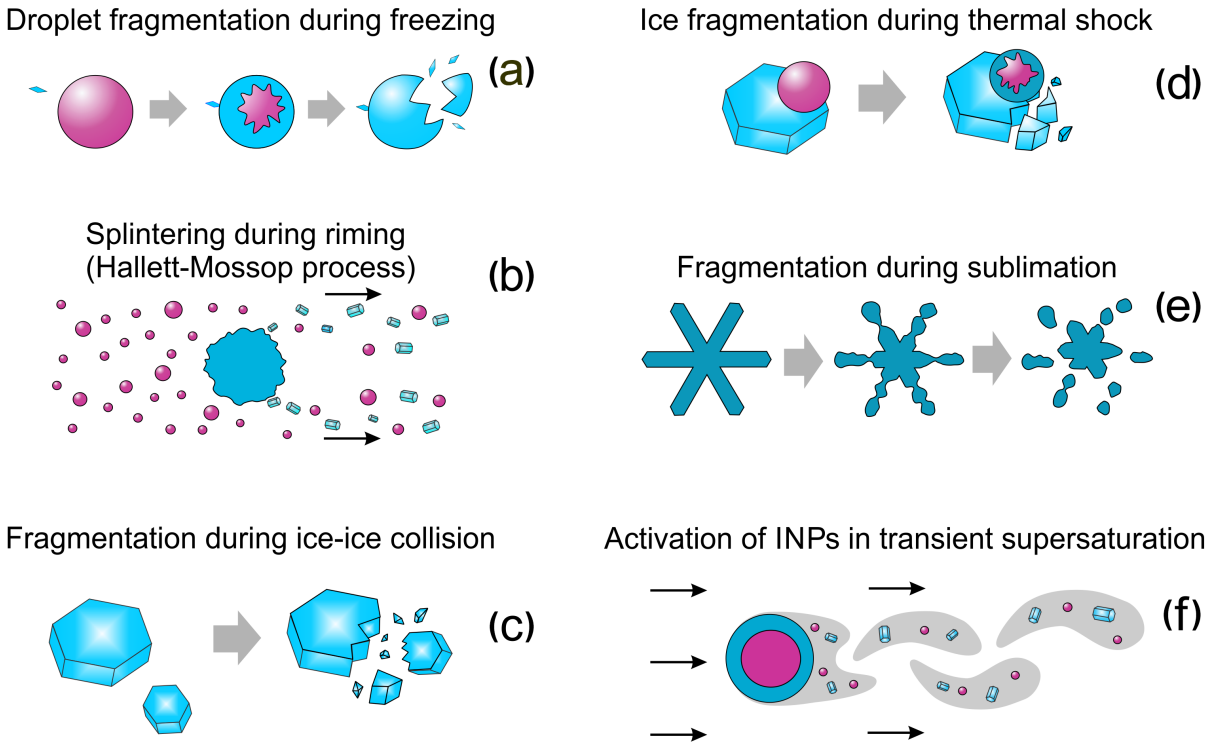

FIG. 5 Schematic of six secondary ice processes. The pink color indicates the liquid phase, and the blue is the ice phase. This figure is Fig. 16 from *Korolev and Leisner* (2020).

Due to the WBF process, the precipitation formation in MPCs is important globally considering the widespread nature of MPCs from the tropics to high latitudes (e.g., *Wang et al.*, 2013; *D'Alessandro et al.*, 2019). Especially in the SO, the precipitation of MPCs accounts for 40 - 50% of all precipitating clouds (*Mülmenstädt et al.*, 2015). Despite the fact that MPCs are microphysically unstable due to the WBF mechanism, stratiform low-level MPCs can persist from hours to weeks (*Shupe et al.*, 2006; *de Boer et al.*, 2009; *Morrison et al.*, 2011; *Stevens et al.*, 2018).

To counteract the depletion of LWP, the stratocumulus MPC needs to be coupled to the surface and a moisture supply. Typically, stratocumulus MPCs consist of a supercooled liquid layer at the cloud top required to maintain the radiative cloud-top cooling (*Shupe et al.*, 2006; *Morrison et al.*, 2012). Below the supercooled liquid top, the cloud phase is mixed with ice precipitation at the cloud base, which may evaporate before reaching the ground. A recent study by *Korolev and Milbrandt* (2022) demonstrates that there are two stages of mixed-phase, one being uniformly distributed (genuinely mixed) and the other spatially separated (conditionally mixed), which might have implications for their radiative effects. In addition, the phase partitioning between ice and liquid in stratocumuli determines the cloud radiative effect (*Sun and Shine*, 1994; *Shupe and Intrieri*, 2004; *Matus and L'Ecuyer*, 2017; *Korolev et al.*, 2017). The impact of ice formation on liquid water in the cloud is crucial as several studies show that the increase of IWP increases with the LWP (*Korolev and Isaac*, 2003; *Shupe et al.*, 2004; *Morrison et al.*, 2005; *Shupe et al.*, 2006, 2008; *Westbrook and Illingworth*, 2011).

Due to the microphysical complexity of MPCs, our knowledge of the influence on the radiative properties caused by ice-liquid partitioning remains constrained (*McCoy et al.*, 2015; *Tan and Storelvmo*, 2019). About 20% of the intermodel spread of the high-latitude LWP are caused by the uncertainties in phase partition in a warming climate (*McCoy et al.*, 2015). Moreover, another uncertainty in climate models is related to the poor

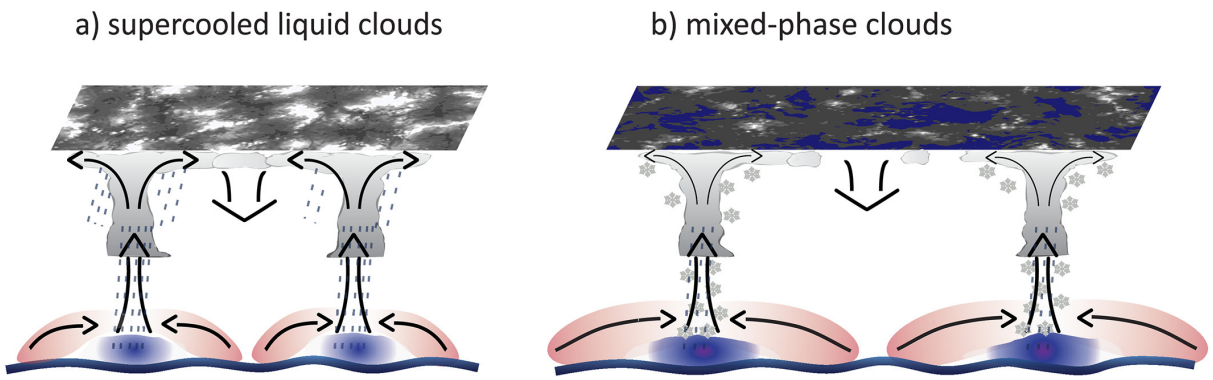

Fig. 6 Conceptual diagram of (a) SLCs and (b) MPCs with open MCC organization. This figure is Fig. 4 from *Eirund et al.* (2019a).

representation of cloud phase feedback, especially in the SO (*Bony et al.*, 2006; *Zelinka et al.*, 2012, 2013). The SO is a particularly important region for global climate sensitivity (*Gettelman et al.*, 2019; *Zelinka et al.*, 2020). This highlights the importance of improving our understanding and, thus, observations of MPCs in the SO and their impact on cloud albedo.

As both the cloud phase and the cloud morphology impact the radiative properties of stratocumuli, investigating the potential link between cloud phase and organization contributes to enhancing our understanding of MCC clouds. This potential link is first examined by *Abel et al.* (2017), *Eirund et al.* (2019a), and *Tornow et al.* (2021). A research flight in the North Atlantic shows that the shift from closed to open MPCs is connected to a transition from MPCs with a high LWP to a lower one (*Abel et al.*, 2017). In addition, the onset of precipitation is the main driver of the closed-to-open-cell transition. Based on this, *Tornow et al.* (2021) explore which ice formation processes are most effective in developing precipitation in the transition. They exhibit that the presence of ice is accelerating the transition of an overcast stratocumulus deck into a broken cloud field due to efficient riming-related effects and termed this *preconditioning*. While *Abel et al.* (2017) and *Tornow et al.* (2021) focus on the link of cloud phase on the close-to-open transition, *Eirund et al.* (2019a) investigates the cloud phase effects on the size of the cloud cells in open MCC MPCs and SLCs. They analyze the cell size differences with a model simulation of a case study in Arctic stratocumulus and find that open MPCs exhibit a larger cell size than open SLCs. This is induced through enhanced precipitation at cloud base below MPCs, leading to stronger cold pools near the surface. Due to the more intense cold pools in MPCs, the open cells expand with the cold pools resulting in larger open MPCs. Figure 6 illustrates the cold pool formation in SLCs and MPCs. However, these three studies focus on case studies with numerical models in the NH to study the link between cloud phase and morphology on a process level. Thus, to further investigate this link and preconditioning due to ice-phase processes, this thesis explores the impacts of cloud morphology and phase in four-year-long satellites-based analysis in the SO.

1.3 Objectives

This Ph.D. thesis aims to investigate differences in marine low-level MPCs and SLCs and the connections between cloud phase, cloud organization, cell size, and cloud albedo with a particular focus on the SO due to the abundance of MPCs in the polar regions. Only a few studies have examined the potential link between cloud organization and cloud phase in marine stratocumuli (*Abel et al.*, 2017; *Eirund et al.*, 2019a; *Tornow et al.*, 2021) focusing

on field campaigns in NH. I use polar-orbiting satellite data to extend this research to the entire SO and global coverage. The main methodical challenges of this project are to distinguish between MPCs and SLCs in satellite retrievals and further to identify single cells of open and closed MCC clouds and to characterize them objectively. The main research objectives of this thesis are outlined here:

1. To obtain a climatology of open and closed MCC MPCs and liquid clouds in the SO with a newly developed vertically integrated cloud phase classification based on active satellite retrievals (Chapter 3).

2. To quantify the impact of ice formation in MPCs on cloud morphology and the dependence of cloud phase on CTT, CTH, and latitude in the SO (Chapter 3).

3. To assess how the cell size of open and closed MCC clouds is affected by its cloud phase and CTH in the SO (Chapter 4).

4. To investigate the link between cloud albedo, cloud phase, and cell size in the SO and its possible implications in a changing climate (Chapters 3 and 4).

5. To establish a global classification of MCC clouds based on cloud reflectance instead of LWP of current MCC classifications (*Wood and Hartmann*, 2006) to also be able to detect ice-phase clouds with no LWP and MPCs with a very low LWP (Chapter 5).

2 Data and Methods

2.1 DARDAR and MODIS

The liDAR-raDAR (DARDAR) v2 data product (*Delanoë and Hogan*, 2010; *Ceccaldi et al.*, 2013) combines data from the Cloud-Aerosol Lidar and Infrared Pathfinder Satellite Observations (CALIPSO) and CloudSat satellites. The two products are collocated onto the CloudSat footprints (∼1.1 km). The advantage of combining lidar and radar measurements is that due to their different wavelengths, they detect different parts of the hydrometer spectrum. While lidar is sensitive to small particles and thus small liquid droplets, the radar is dominated by larger particles and, thus, mainly ice particles. In this study, DARDAR v2 is used. This product significantly reduces the overestimation of supercooled pixels in the lowest part of the troposphere compared to DARDAR v1 (*Ceccaldi et al.*, 2013). We analyze data covering the time period from 2007 to 2010 and focus on the SO (40° S to 65° S). While *Huang et al.* (2021b) report large differences in cloud phase detection between various satellite products, which struggle specifically with MPCs, they use the DARDAR v1, which is known to overestimate supercooled liquid. In contrast, DARDAR v2 is validated with several ground-based measurements in the Antarctic by *Listowski et al.* (2019), who also show that DARDAR v2 has the ability to capture the seasonal cycle of SLC fraction. Nevertheless, MPCs with very low ice crystal number concentrations, which are common in the SO might still be misidentified as supercooled liquid. Further, we chose the DARDAR product as it merges information from two active instruments and thus provides a vertically resolved cloud phase. This is in contrast to passive satellites that only resolve cloud phase at cloud top. The DARDAR cloud classification additionally requires a temperature profile in the radar mask and the strong lidar backscatter layers ($\beta_{532} > 2 \times 10^{-5}\,\mathrm{m^{-1}\,sr^{-1}}$) of the DARDAR classification algorithm. For further details on the DARDAR algorithm, see *Ceccaldi et al.* (2013). The temperature and other thermodynamic variables like SST and surface wind speeds are collocated on the CloudSat track by the European Centre for Medium-Range Weather Forecasts (ECMWF)-AUX. Moreover, in this study, we combine the DARDAR v2 product with the MODIS cloud product (MYD06_L2) Collection 6 (C6) version from the Aqua satellite (*Platnick et al.*, 2015). The LWP and the COT are provided by MODIS. Further, we derive the in-cloud albedo (Alb_{cld}) from the MODIS COT to remain consistent with DARDAR's horizontal pixel resolution of 1.1 km. Following *Berner et al.* (2015) based on

Platnick and Twomey (1994), we use the equation:

$$\mathrm{Alb}_{cld} = \frac{(1-g)\tau}{2+(1-g)\tau}, \tag{1}$$

where, COT is indicated as τ and the asymmetry parameter is g = 0.85 which assumes small water droplets. *McFarquhar and Cober* (2004) find that MPCs peak at g = 0.85 and liquid clouds at g = 0.87. Further, *Gayet et al.* (2002) show that in MPCs, the asymmetry parameter ranges from 0.82 to 0.85 (i.e. is similar to values in liquid clouds). They find higher values of g are typically found in liquid clouds with high liquid water content, whereas lower values of g (0.73–0.80) are found in ice clouds. This corresponds to findings by *Shcherbakov et al.* (2005) and *Xu et al.* (2022), who demonstrate that the asymmetry parameter is g = 0.77 in cirrus clouds in the Southern Hemisphere. As differences between liquid clouds and MPCs are similar, the asymmetry parameter g = 0.85 is used for both liquid and MPCs.

2.2 Vertically Integrated Cloud Phase

To analyze the cloud phase, we use the DARDAR cloud classification, which provides a vertically resolved cloud phase with a 60 m resolution from surface to 25.08 km. This vertically resolved cloud phase is based on a lidar and radar mask provided by the DARDAR algorithm (for details, see Tab. 1 of *Ceccaldi et al.* (2013)). Therefore, when the lidar signal is fully attenuated, the DARDAR classification can only determine the layer to be ice cloud, warm rain, or cold rain. The DARDAR classification has 17 different categories, which are displayed in the example tracks of DARDAR in Fig. 17 a and S1. In this study, the following categories of DARDAR are grouped into four categories: (1) *Ice* (ice clouds, spherical or 2D ice, and highly concentrated ice), (2) *Sup* (supercooled water and multiple scattering due to supercooled water), (3) *Mix* (supercooled + ice), and (4) *Liq* liquid warm. To reduce the vertical cloud phase into a vertically integrated cloud phase, we first identify the highest and lowest cloud levels which are categorized as *Sup*, *Mix*, or *Liq*. The height of the highest cloud level is defined as the CTH and the lowest as the liquid cloud-base height (CBH). As a result, we exclude pure ice clouds because the MCC algorithm is based on the LWP (see Section 2.3). Since we are only interested in low-level clouds, any data point with CTH above 3 km is excluded from this analysis. The surface cluttering of radar can cause noise up to 2 km which can not be clearly distinguished from the signal, especially at heights below 720 m, and thus clouds are missed (*Marchand et al.*, 2008). Even though some studies (*Liu et al.*, 2012; *Fletcher et al.*, 2016b) consider anything roughly below 1 km as ground clutter, *Mioche et al.* (2015)

show that in comparison with ground-based observation, the cloud fraction of DARDAR is 10% lower from 500 m to 1000 m, while in the range from 0 m to 500 m it is 25% lower. Thus, in this study, we consider 720 m as the threshold for surface clutter, similar to other studies (*Kay and Gettelman*, 2009; *Huang et al.*, 2017; *Noh et al.*, 2019; *Listowski et al.*, 2019). In order to correctly identify the cloud phase, however, we require one level below the liquid CBH. Thus, we restrict our analysis to clouds with a liquid CBH at 780 m or above. Moreover, we remove any multi-layer clouds, defined here as clouds with three or more consecutive vertical levels marked as clear or fill values. As the constructed vertical resolution of DARDAR is 60 m, three levels equal a distance of 240 m. This is also the oversampled vertical resolution of CloudSat (effective vertical resolution is 480 m). Thus, this distance ensures that multi-layer clouds are two separated clouds with a sufficiently large separation.

In order to assign one cloud phase to a certain data point in DARDAR, we need to reduce the DARDAR cloud classification in the vertical dimension. Therefore, all data points are classified into MPCs, liquid clouds, or clear, depending on their vertical phase distribution (Fig. 17 b). Here, we only analyze pixels. Liquid clouds are considered to be clouds that only consist of *Liq*, *Sup*, or *Sup* above *Liq* (*Sup* $\rightarrow$ *Liq*). For MPCs, we consider five different types: only *Mix*, *Mix* above *Ice* (*Mix* $\rightarrow$ *Ice*), *Sup* above *Ice* (*Sup* $\rightarrow$ *Ice*), any combination of *Sup* and *Mix* (*Sup* $\leftrightarrow$ *Mix*), and any combination of *Sup* and *Mix* above *Ice* (*Sup* $\leftrightarrow$ *Mix* $\rightarrow$ *Ice*).

Typically, the lidar signal in our cloudy pixels fully attenuates within 300 m (five vertical levels) (interquartile range = 360 m – 240 m), and thus provides information beyond the cloud-top phase. As mentioned above, the radar mask of the DARDAR classification requires the ECMWF wet bulb temperature to distinguish between the ice ($\leq 0\,^{\circ}\mathrm{C}$), and liquid ($> 0\,^{\circ}\mathrm{C}$) or rain ($> 0\,^{\circ}\mathrm{C}$) phase. Therefore, this could lead to uncertainty in the cloud-phase classification close to 0 °C, especially if the lidar signal is fully attenuated. As this affects cloud-phase classification at temperatures close to 0 °C, this should not lead to a bias in the overall cloud-phase distinction. Furthermore, for temperatures below 0 °C, the radar classification cannot distinguish between supercooled drizzle and ice. In the SO in particular, supercooled drizzle is observed in stratocumulus clouds at temperatures near $-10\,^{\circ}\mathrm{C}$ (*Mace and Protat*, 2018). Furthermore, *Silber et al.* (2019) show that at the observation station McMurdo, in Antarctica, supercooled drizzle can persist at temperatures below $-25\,^{\circ}\mathrm{C}$ for several hours. While it might be possible that the *Mix* classification of DARDAR itself is affected as this category is supercooled liquid from lidar and ice from radar. We find it unlikely that multiple layers of *Mix* could be affected since the lidar signal would fully attenuate in the presence of drizzle and the vertical lidar resolution of CALIPSO is 30 m. As most MPCs that contain *Mix* have mixed layers with a thickness

of roughly 480 m (eight vertical levels in DARDAR) (see Fig. 17a and Fig. S1), the MPCs with identified *Mix* levels from the radar retrieval are unlikely to be pure drizzle. However, the misclassification of supercooled drizzle as *Ice* could lead to false identification in MPCs when the lidar signal is fully attenuated, especially in the cloud category *Sup* → *Ice*, as the *Ice* in these clouds could be supercooled drizzle. Supercooled drizzle is reported to be misclassified as ice by several studies (*Cober and Isaac*, 2012; *Zhang et al.*, 2017, 2018; *Villanueva et al.*, 2021), particularly at temperatures above −10 °C.

To further test the uncertainties of misclassified supercooled drizzle, we checked how our results are changed if only clouds with an effective radius of $0\,\mu m < R_e < <14\,\mu m$ at cloud top are investigated. Thus, precipitating clouds should be excluded as $R_e > 14\,\mu m$ at cloud top initiates drizzle (*Han et al.*, 1995; *Rangno and Hobbs*, 2005; *Rosenfeld et al.*, 2012; *Freud and Rosenfeld*, 2012). However, we only find slight changes with this threshold (compare Fig. 19 with Fig. S2). Further, since MODIS is not able to calculate R_e in more than 50% of the identified MPCs (Fig. S4), and since we would also exclude correctly identified precipitating MPCs, the threshold of R_e is not used as a constraint in this study.

The ECMWF CTT is defined as the temperature from ECMWF at CTH. As shown in four examples in Fig. S3, our data set, which is combined with MODIS, also provides the CTT from MODIS. However, we decide to use the ECMWF CTT for two reasons: 1) because it will be more consistent with the DARDAR classification methodology, which is also based on the ECMWF temperature and further because CTH between DARDAR and MODIS varies and 2) because the MODIS CTT exhibits unrealistically large and abrupt changes of more than 10 °C within a distance of 2 km (Fig. S3). From a brief visual inspection, it seems to be related to jumps in MODIS CTH which are not detected by the active satellites. Furthermore, we find that the MODIS CTH is often higher than that of DARDAR.

2.3 MCC Classification Dataset

The MCC regime identifications are developed by applying the supervised neural network algorithm designed in *Wood and Hartmann* (2006) to C6.1 MODIS Aqua LWP swath data. The algorithm uses the power density function and power spectrum of LWP to determine whether swath sub-scenes (256 km×256 km areas) fall into one of three categories: open MCC, closed MCC, or cellular but disorganized. See *Eastman et al.* (2021) for more information on the C6.1 MCC identifications. To collocate the MCC data set with the CloudSat track, the haversine distance for all DARDAR data points to the middle of each MCC scene is calculated. The MCC regime of the nearest MCC scene within a radius of

128 km is set for each DARDAR data point.

2.4 MCC Classification with CNN

As the MCC classification described in Section 2.3 is based on the LWP, this potentially influences the detection of MPCs and ice-phase clouds, especially MPCs with a low LWP could be missed. Thus, I introduce a manual classified MCC data set, which is used to develop a MCC classification with a deep convolutional neural network (CNN) model based on the MODIS 0.86 µm reflectance band. A CNN is an artificial neural network that is commonly used in image pattern recognition (*LeCun et al.*, 2015) and is also used by *Yuan et al.* (2020) and *Lang et al.* (2022) to classify open and closed MCC among other categories and not based on the MODIS 0.86 µm reflectance band. The preparation of the manual MCC data set and the CNN model development are part of the master thesis from Christopher Reichel, which I supervised during my Ph.D. thesis (*Reichel*, 2022). Christopher Reichel tested different data augmentation methods and several different CNN model setups. In this thesis, I only use the most promising CNN model to identify MCC globally (Section 2.6). As the master thesis is not published, the Sections 2.4.1 to 2.4.4 describe in detail the setup of the classified MCC data set, and the CNN model with the best performance.

2.4.1 Scene Selection

The development of any artificial neural network requires a manually created data set that provides data that needs to be classified, in this case, an image and the corresponding classification. This section describes which data is used for the scenes (images) and how they are selected and afterward classified.

To have the possibility to combine the MCC classification of the CNN model with the cell identification from Section 2.5, the scenes are also based on the MODIS 0.86 µm reflectance band with a 1 km resolution (*Platnick et al.*, 2015). For further details on the MODIS Aqua cloud product (MYD06), see Section 2.5. Here, we use the seasons JJA and DJF of the years 2008 and 2009. As mentioned in Section 1.2.2, we focus on these two seasons because open and closed MCC clouds have the highest frequency of occurrence, respectively, in winter and summer (*Muhlbauer et al.*, 2014). To achieve a higher percentage of MCC clouds compared to other types of low-level clouds, we only select scenes in specific regions that are known to favor MCC cells. These five regions are: North Atlantic (40 - 60° N, 25 - 45° W), South East Pacific (20 - 40° S, 70 - 90° W), South East Indian (40 - 60° S, 70 - 90° E), North East Pacific (15 - 40° N, 120 - 150° W), and South

Pacific (30 - 60° S, 90 - 180° W).

To train the CNN model, we need an equal amount of open and closed MCC cloud scenes, as otherwise, the model could become biased to the classification with more scenes. As closed MCC clouds dominate the statistic in summer but are more equally distributed with open cells in winter, we use the winter season of all regions, which means DJF for the Northern Hemisphere regions and JJA for the SH regions. We also classified the summer months for the regions North Atlantic, South East Pacific, and South East Indian because we noticed a tendency towards open MCC clouds during our classification.

All scenes have a size of $224 \times 224\,\mathrm{km}^2$. This scene size can capture the cloud morphology of MCC clouds and is small enough to be computationally efficient. Moreover, this is a typical image size in CNNs (e.g., *Krizhevsky et al.*, 2012; *Kiela and Bottou*, 2014; *Simonyan and Zisserman*, 2015; *Chen et al.*, 2019). As the CTH and other cloud top properties deviate more strongly in satellite scan angles greater than 32° (*Menzel et al.*, 2010), only the inner 706 pixels across the track (of 1354 pixels) with a scan angle <32° are used from each MODIS granule. This leads to a maximum of 27 scenes per MODIS granule. However, we further filter the scenes by CTH and the land-sea mask. The MODIS Aqua MYD03 geolocation product provides the land-sea mask along with the longitude and latitude at 1 km resolution. As open and closed MCC are low-level clouds, the mean CTH of the scenes needs to be below 3.5 km. Further, all scene pixels are required to be over the ocean which is at least 5 km from the coast or deeper than 50 m (corresponding to the two land-sea mask categories: "moderate or continental ocean" and "deep ocean").

2.4.2 Manual Classification

These selected scenes are classified by five persons, hereafter classifiers, through visual inspection of each scene. The five classifiers are trained to identify the MCC morphology of open and closed cells. In total, 28645 scenes are available after filtering in JJA and DJF in 2008 and 2009. However, after three days of classifying scenes, 6944 remain unclassified. Thus, 21701 images are classified by all of the five classifiers. All 21701 scenes are categorized into one of the five categories: Open, Closed, NoMCC, Disorganized, and Error. The Open, Closed and Disorganized category is only assigned to a scene if at least 70% of a scene is covered with the respective morphology. All scenes with less than 70% of these morphologies are categorized as NoMCC. The NoMCC category further includes all other scenes that do not belong to one of the MCC regimes, such as stratiform clouds or almost cloud-free ocean scenes, except for erroneous scenes. Close to a latitude of 60° S/N in the respective winter season, there often is a detection limit of the passive satellite instrument MODIS due to the missing solar insolation and the very short daytime. This

TABLE 1 Number of scenes classified by each of the five classifiers separately divided by the categories. Table taken from *Reichel* (2022).

Classifiers	Open	Closed	Disorganized	NoMCC	Sum	Error
Classifier 1	1031	663	18	18246	19940	1698
Classifier 2	1381	1038	84	17425	19844	1721
Classifier 3	710	482	109	18455	19647	1657
Classifier 4	1683	839	100	17195	19717	1878
Classifier 5	940	705	60	13021	14666	1108

leads to scenes with precise edges and a large connected area with fill values. These scenes and scenes with apparent spurious features are classified as Error.

The classifications of all five classifiers are shown in Table 1. The scenes with the category Error are removed from the data set as we are not interested in the erroneous scenes and are only shown for completeness. Table 1 also shows the sum of the four remaining categories. Note that Classifier 5 processed about 4000 fewer scenes in total compared to Classifiers 1-4. This is caused by the loss of a file containing some classification results of Classifier 5. The lost file, however, only contained classifications during the summer months. As almost all scenes are classified as NoMCC in summer by the other four remaining classifiers, this should not affect the overall statistic of the Open and Closed categories. This is supported by the fact that for Classifier 5, the only category drastically reduced compared to the other classifiers is the NoMCC category. The category Disorganized is only detected for a couple of scenes with a maximum number of 109 by Classifier 3. This is probably due to our region selection as the selected regions have a low frequency of occurrence for disorganized cells (*Muhlbauer et al.*, 2014). All classifiers label more scenes as Open than as Closed. Even the additional classification of summer months for some regions could not entirely avoid a tendency toward the Open category. Although all classifiers categorize more Open scenes, the number of classified scenes in each category varies between the five classifiers.

To further ensure the correct classification of the scenes, a certain number of classifiers must agree on each scene's category for a scene to be included. Table 2 shows the number of scenes for which at least three or four classifiers agree on the category. In total, there

TABLE 2 Number of scenes for which at least three or four Classifiers agree on the category. Table taken from *Reichel* (2022).

Number of Classifiers in Agreement	Open	Closed	Disorganized	NoMCC
3 or more	847	550	3	18374
4 or more	405	255	0	16703

are 847 Open and 550 Closed scenes.

As the CNN model needs to be able to classify Open, Closed, and NoMCC scenes correctly, we need a training and testing data set with an equal number of scenes in each category. Thus, we can only use 550 scenes for each category. We use all 550 Closed scenes and randomly sample 550 Open and 550 NoMCC scenes. This yields a data set with a total of 1650 unique scenes, which are manually divided into 70% (1155 scenes) training and 30% (495 scenes) testing data set. The training and testing data sets individually have an equal amount among the three categories (training: 385 scenes, test: 165 scenes). Further, to train the model, the training data set is further divided into another 70% (808 scenes) training and 30% (347 scenes) validation data set. The split between the training and validation data set is automatically executed by the argument *validation_split* of the *model.fit* function from the *tensorflow* package in Python (*Pang et al.*, 2020). Unfortunately, with this argument, the data is split by taking the last, in our case, 30% of the 1155 scenes without any regard for the category. We only noticed this after the Master Thesis of *Reichel* (2022) was finished. Therefore, our training and validation data sets do not have the same number of scenes for each category. The training data set has 273 Open, 269 Closed, and 266 NoMCC scenes, and the validation data set has 112 Open, 116 Closed, and 119 NoMCC scenes. While having an unequal number of scenes is not ideal for training, the maximum difference between the categories Open and NoMCC is only 2.6% in the training data set. Thus, the CNN should not favor the category Open. To improve the performance of the model, the diversity of the training data set (808 scenes) is artificially extended by data augmentation, described in the Section 2.4.4.

2.4.3 CNN Model

In general, deep learning means that in an artificial neural network, which is a computational model consisting of multiple layers, patterns in a large data set are recognized by changing the model's internal parameters through the backpropagation algorithm (*LeCun et al.*, 2015). A CNN uses deep learning to train and consist among other layers of at least one convolutional layer. Deep CNN models can recognize complex patterns in images similar to humans (*LeCun et al.*, 2015). This section describes the CNN training process and its specific configuration. To set up to CNN, we use the *tensorflow* package in Python (*Pang et al.*, 2020). The *tensorflow* package is open-source software that is widely used and developed by Google researchers.

The training data set is split into batches to train or fit a CNN model. A batch or batch size is the number of scenes the model is trained on at one time. Here, we set the batch size to 20 scenes. This training is repeated on all 41 batches of the 808 training data

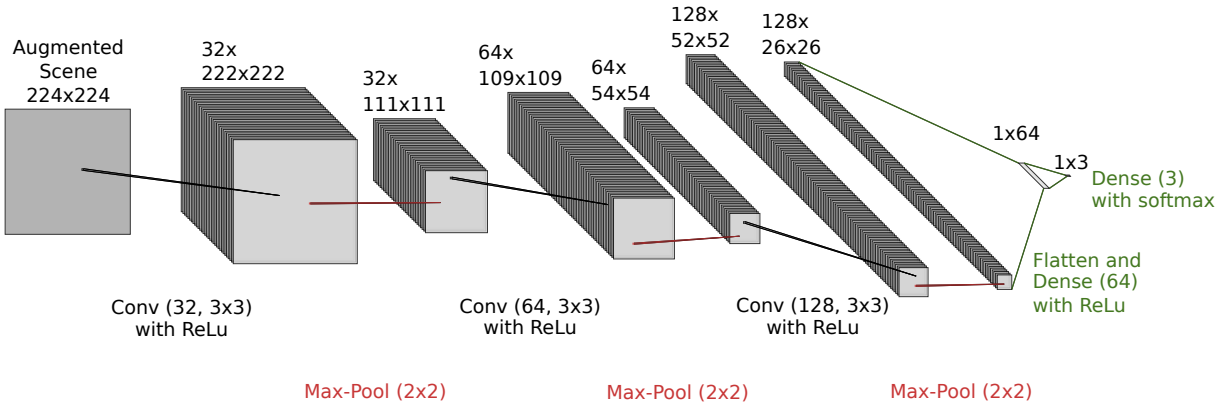

FIG. 7 Schematic representation of the CNN with three convolutional layers with max-pooling for feature extraction and two dense layers for classification. In the convolutional layer (Conv), the first number in brackets indicates the number of kernels (filters), and the second is the kernel size. The CNN architecture is produced with the online tool "NN-SVG" with the LeNet style from *LeNail* (2019).

scenes, where the last batch only has eight scenes. After each batch, the model learns to categorize the scenes with a learning rate of 0.001 with the adam optimizer. This complete run of all batches is called an epoch. At the end of each epoch, the loss and accuracy of the training and validation set are calculated. While the model is only actively trained on the augmented training data set, the accuracy of the validation data set is also used at the end of each epoch to adjust the CNN's internal parameters. Thus, the validation data set is still indirectly used to train the model and, therefore, is not used to test the model. The final CNN model is trained with 50 epochs, and due to the random augmentation of each training data set (see Section 2.4.4), 40400 differently augmented scenes are evaluated in total.

The architecture of the CNN consists of three convolutional layers, followed by a max-pooling layer. The complete architecture of the CNN is shown in Fig. 7. The three convolutional layers extract the patterns or features in the scenes and use the rectified linear unit (ReLu) activation function. The ReLu activation function is a nonlinear function that sets the negative values to zero and retains the positive values (*Gu et al.*, 2018). Each convolutional layer of the CNN has a different number of kernels (filters) but the same kernel size of 3 x 3. The number of kernels increases from the first convolutional layer to the last from 32, 64, to 128. The kernels in the first convolutional layer are designed to detect features like curves and edges in the scenes. In contrast, the following convolutional layers recognize more abstract patterns in the scenes (*Gu et al.*, 2018). The max-pooling layers after each convolutional layer have a kernel size of 2 x 2, which reduces the scene size by half in height and width by taking the maximum. The max-pooling layers are mainly used to reduce the number of parameters and, thus, increase the computational efficiency

(*Dhillon and Verma*, 2020). Further, these layers also help to prevent overfitting of the CNN. Overfitting occurs when a model cannot generalize the learned pattern but can only predict the training data set well (*Moen et al.*, 2019). However, data augmentation should also reduce this (Section 2.4.4).

The last convolutional layer has a size of 128 x 26 x 26 and is flattened to 86528 to be connected with the dense layers. The last two layers of the CNN are the dense layers that are part of the actual classification compared to the feature extraction of the convolutions layers. These dense layers are fully connected, meaning each neuron of the layer is connected to all inputs of the previous layer. The first dense layer has 64 neurons and is also activated by ReLu. The final dense layer has three neurons which are the three categories (Open, Closed, and NoMCC), the model is supposed to predict. This dense layer uses the activation function softmax, which assigns a probability to each of the three neurons. The class or neuron with the highest probability is the final prediction of a scene.

The evaluation of the CNN training is shown in Fig. 8. It shows that the training and validation accuracies asymptotically approach an accuracy of around 80% within the first 20 epochs. As the training and validation loss converge after about 15 epochs and do not spread apart with a higher number of epochs, this shows that the CNN is not overfitted. The CNN model configuration with the best validation accuracy of 83.28% at epoch 42 is saved.

2.4.4 Data Augmentation

Data augmentation is a common method in CNNs to increase the variance artificially and, thus, the training data set size by slightly modifying the scenes, i.e., rotating the

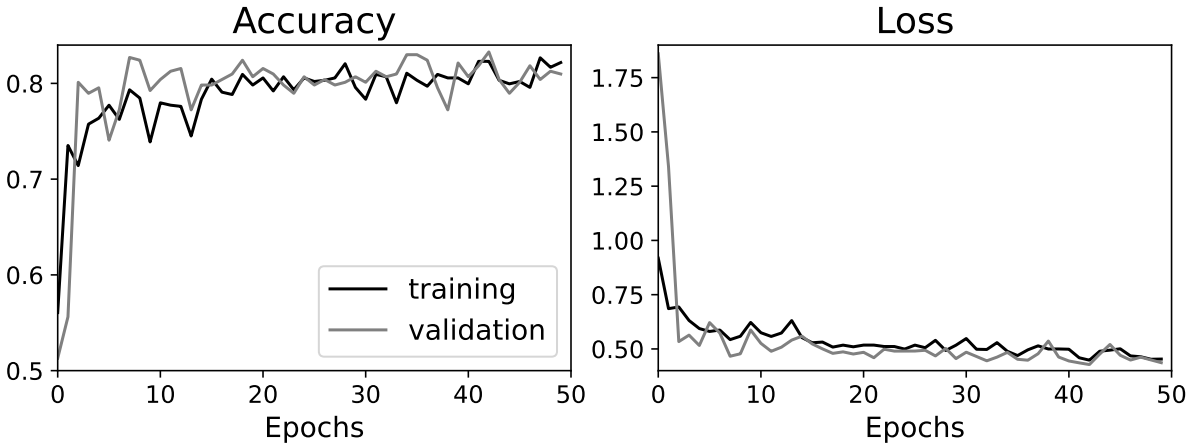

Fig. 8 Accuracy and loss for training and validation data set at each epoch. Figure adjusted from *Reichel* (2022).

image. However, it is essential that the image transformation, even though artificial and random, still provides realistic images that could have been observed in clouds over the ocean. *Perez and Wang* (2017) demonstrate the effectiveness of simple data augmentation methods such as flipping, cropping, zooming, or rotation. An example of manual data augmentation is shown in Fig. 9. Previous studies show that with a more extensive data set, the performance of deep learning models, like CNNs, improves (*Sun et al.*, 2017; *Barbedo*, 2018; *Soekhoe et al.*, 2016).

The training data set is augmented with an augmentation layer which is a function of

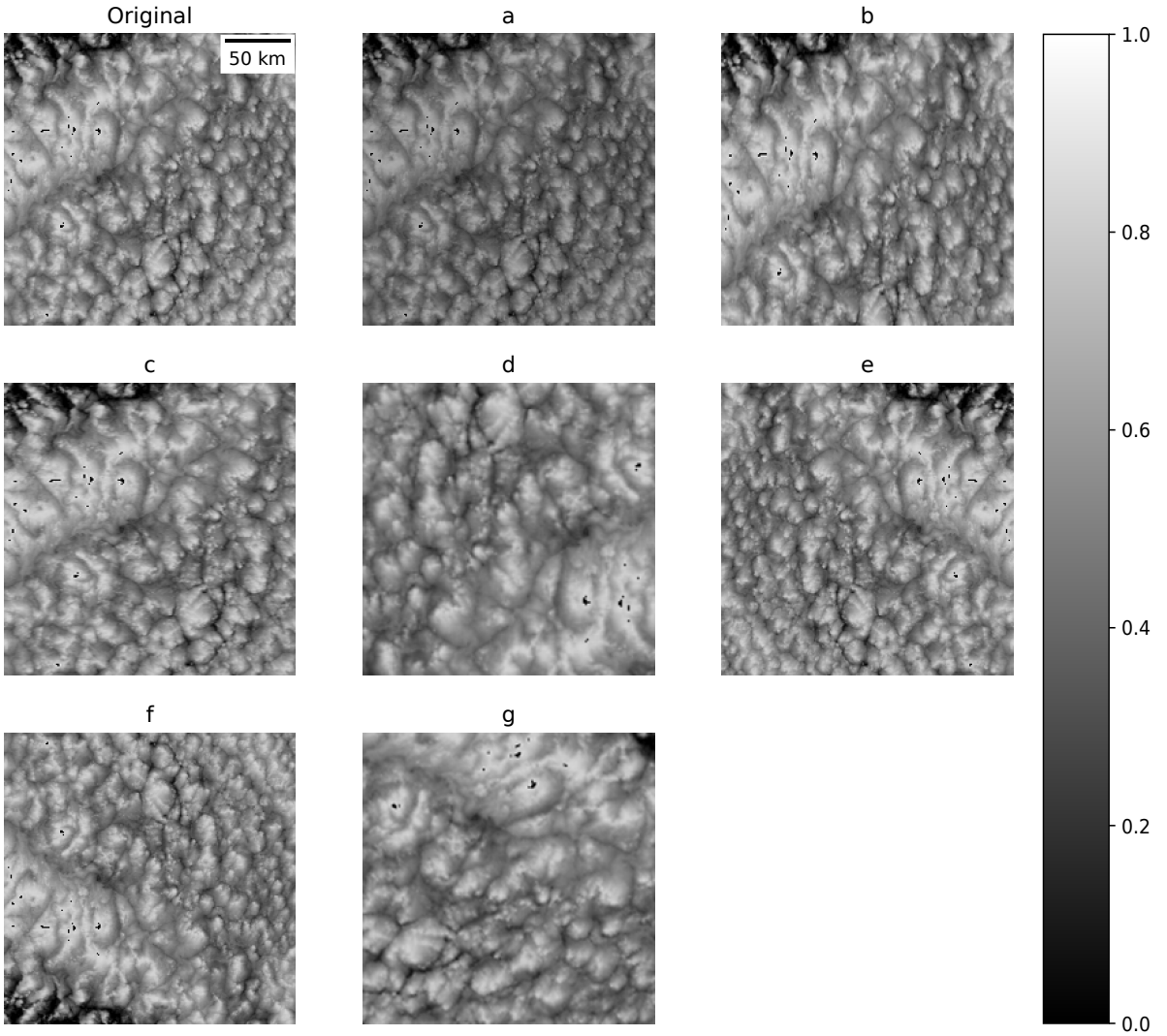

FIG. 9 Different single data augmentations (a-g) of the original scene (top left). (a) brightness, multiplied by a factor of 0.8 (b) horizontal crop, 44 pixels cropped and resized to $224\times224\,\mathrm{km}^2$ (c) vertical crop, 44 pixels cropped and resized to $224\times224\,\mathrm{km}^2$ (d) zoom, a factor of 0.3 (e) horizontal flip (f) vertical flip (g) rotation and cropping, rotated by 60°, cropped to $163\times163\,\mathrm{km}^2$ and than resized to $224\times224\,\mathrm{km}^2$. Figure taken from *Reichel* (2022)

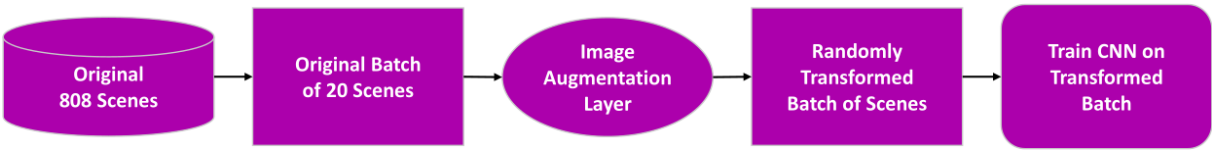

FIG. 10 The flowchart represents the data augmentation process on one batch of 20 scenes.

the *tensorflow* package in Python (*Pang et al.*, 2020). The data augmentation layer runs synchronously with the other layers of the CNNs and is more computational efficiently than an asynchronous augmentation layer. However, the preprocessing layer of data augmentation is inactive when the model is tested or evaluated. In the augmentation layer, the image transformations occur randomly while training the model. Thus, the original 808 images are randomly transformed, meaning all six transformation types occur randomly. The six types of transformation are: flipped horizontally and vertically, rotated by an angle divisible by 40°, zoomed in the range of 10 - 20%, changed in contrast by a factor 0.7, cropping of the images to the size $163 \times 163\,\mathrm{km}^2$ and being translated in width and height by a factor of 0.2. The data augmentation process is schematically shown in Fig. 10. The original 808 training data scenes are never passed to the CNN instead, a randomly transformed version of this data set is provided. Thus, the data set size is not increased as each model epoch, which is one complete run of all training data, still has an input of 808 scenes. However, due to the randomness of the transformations, each epoch is trained with a "new" version of scenes, which effectively increases the training size.

2.5 Cell Identification

This section describes how single open and closed MCC cells are automatically identified in a reflectance band of the Aqua satellite. I am interested in investigating whether the cell size of these two MCC organizational regimes is influenced by the cloud phase. The following Sections 2.5.1 to 2.5.2 define the processes from scene preparation to image segmentation and the subsequent calculation of mean cloud properties of the single cells.

2.5.1 MODIS Scene Preparation

To identify single cloud cells in MCC organizational scenes, I use the MODIS cloud product (MYD06) Collection 6.1 (C6.1) from the Aqua satellite with a 1 km and 5 km resolution in the SO (40° S to 65° S) from 2007 to 2010 (*Platnick et al.*, 2015). This time period is used as 2007 is the first full year in which CALIPSO and CloudSat joined the Afternoon Constellation (A-Train). The A-Train constellation in this time period con-

sisted of five satellites that fly close to each other in the following order: Aqua (2002), CloudSat (2006), CALIPSO (2006), PARASOL (2004), and Aura (2004). On April 17th, 2011, CloudSat temporarily left the A-Train due to a battery failure but rejoined the constellation behind CALIPSO on May 12th, 2012 (*Stephens et al.*, 2018). However, due to the positional change of CloudSat, I only investigate the time period from 2007 until 2010 for consistency of the three used satellites (and their data sets): Aqua (MODIS), CALIPSO (DARDAR), and CloudSat (DARDAR).

From the Aqua MODIS cloud product (MYD06), the following scientific retrievals are used with a 1 km resolution: corrected atmospheric reflectance, CTH, COT, LWP, and effective radius R_e at/near cloud top. From the corrected atmospheric reflectance, only the 0.86 µm reflectance band is investigated as this band minimizes the underlying surface reflectance over oceans (*Platnick et al.*, 2003). The COT and the effective radius R_e are derived from the water-absorbing visible or near-infrared (VIS/NIR: 1.6 µm, 2.1 µm and 3.7 µm) and non-absorbing SW infrared (SWIR: 1.6 µm and 2.1 µm) bands at 1 km horizontal resolution (*Nakajima and King*, 1990; *Platnick et al.*, 2003, 2017). The cloud LWP is based on the effective radius R_e and COT retrievals by assuming an idealized cloud with an increasing liquid water content from cloud base to cloud top with a constant cloud droplet number concentration (*Han et al.*, 1994). All three retrievals, COT, LWP, and effective radius R_e, depend on a correctly identified MODIS cloud phase, which only accounts for liquid or ice-phase clouds. Thus, this leads to biases in these MODIS retrievals in MPCs (*Miller et al.*, 2014) as they are treated as liquid-phase clouds. *Khanal and Wang* (2018) show that in stratiform MPCs the LWP increases by about 15% and the COT bias by about 8% at an IWP of 150 g m^{-2} caused by the phase treatment. Further, they show that most MPCs exhibit an IWP <150 g m^{-2}. Therefore, this bias in MPCs should only slightly affect the analysis of the in-cloud albedo based on COT (Section 2.1). The MODIS CTH retrievals are by about 0.5 km higher than the CTH retrieve by CALIPSO (*Baum et al.*, 2012). However, the MODIS CTH is only used to select low-level scenes, while the DARDAR is used for further investigations.

The Aqua MODIS geolocation product (MYD03) is used to retrieve longitude and latitude at 1 km resolution as the MYD06 product only contains them at 5 km resolution. The Aqua MODIS satellite swath is stored in granules that contain 5 minutes of the swath. Each MODIS granule has a size of 1354 km across the satellite track and 2030 km (every 10th granule 2040 km) along the track. Further, as the reflectance from a passive instrument like MODIS is only retrieved during day time, only day-time granules are used.

To evaluate the cloud phase of the single MCC cells, I use the DARDAR data set with the vertically integrated cloud phase described by *Danker et al.* (2022a) and in Section 2.2. This data set is based on an active instrument that retrieves data as a line

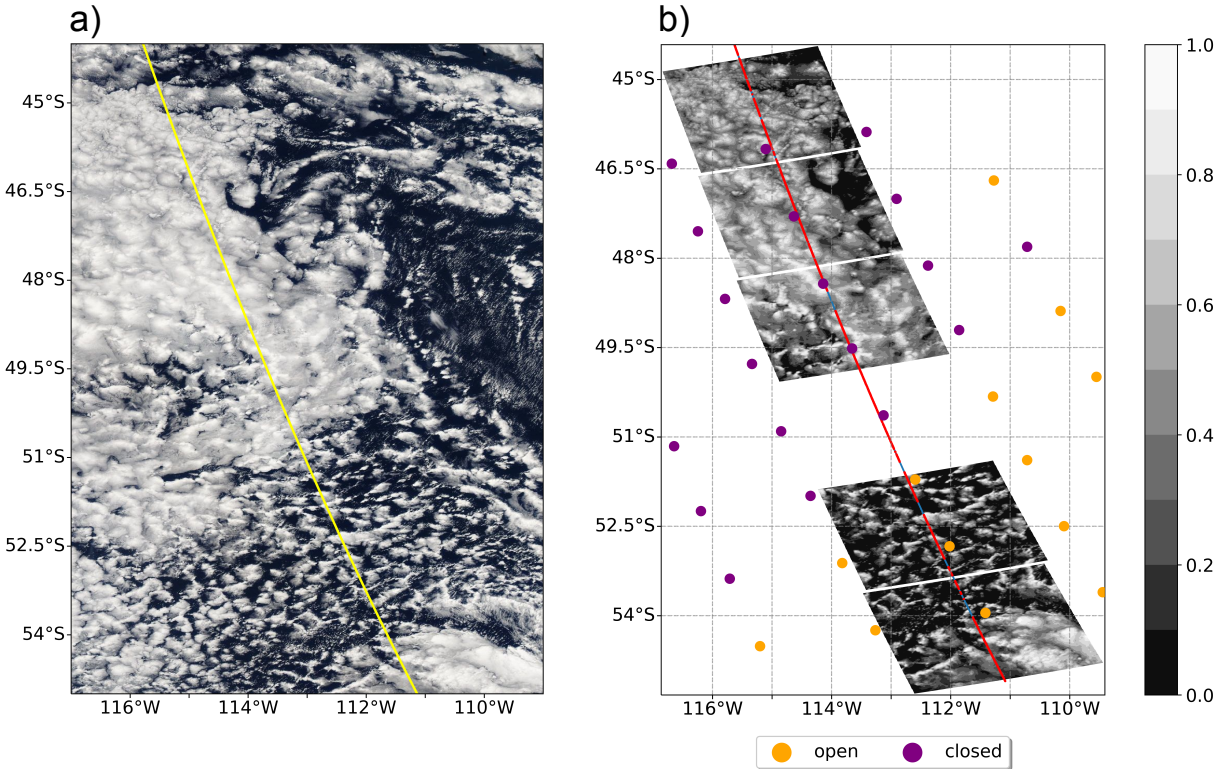

FIG. 11 (a) Visual image of MODIS Aqua on February 3rd 2007 with the yellow line indicating the DARDAR track (provided by: `https://earthdata.nasa.gov`). (b) Composite of five MODIS 0.86 µm reflectance scenes with the DARDAR track. The original data points of the MCC data set from *Wood and Hartmann* (2006) are shown for open and closed MCC categories. The valid DARDAR points are overlaid in red on the track in blue. Out of these five scenes, only four cells are identified as the southernmost scene has no peak in the 2D Fourier transformation (see Section 2.5.2). The missing scene in the middle is not passed to the segmentation as it contains both open and closed DARDAR points.

along the satellite track instead of a swath like MODIS. As I am particularly interested in MPCs, the MODIS cloud top phase can not be used as most MPCs are identified as liquid clouds due to their supercooled liquid top (*Adhikari et al.*, 2013). Thus, the scenes are cut with the DARDAR track defining the center across the track with a size of $200 \times 200\,\mathrm{km}^2$ (Fig. 11 b). The scene selection process is illustrated schematically in Fig. 12. Only oceanic scenes with at least 40% of valid DARDAR points are passed to the image segmentation described in Section 2.5.2. Here, valid DARDAR point means that the data point has to be a low-level cloud with a DARDAR CTH below 3 km and is either a MPC or liquid cloud. While I choose this value to ensure enough cloudy data points along the DARDAR track, this could potentially influence the cell diameter as scenes with very large open cells might exhibit less than the 40% valid DARDAR points due to their generally lower cloud fraction (e.g., *Wood and Hartmann*, 2006). Moreover, I also require at least 40% of

DARDAR points in each scene to be assigned to a MCC regime of either open or closed by the MCC data set described in Section 2.3. If a scene contains both open and closed MCC data points, the scene is not passed to the segmentation as shown in Fig. 11 b. Notice that due to the slightly different resolutions of MODIS (1 km) and DARDAR (1.1 km), a maximum number of 181 DARDAR points is possible in each scene.

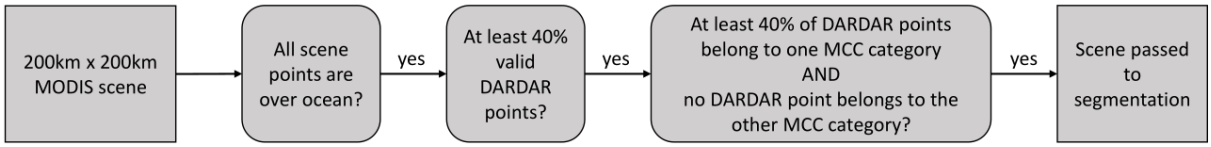

FIG. 12 The schematic representation of the scene selection process for segmentation.

2.5.2 Image Segmentation Methods

Image segmentation methods are algorithms to segment a digital image into specific areas or objects by their visible features. In the following, two marker-based image segmentation methods are conceptualized, which are used for scenes with open (watershed) and closed (random walk) MCC cells.

The conceptual description of the marker-based watershed image segmentation is gray-scale image segmented by using the image as a topographic map where the pixel's intensity is considered as its height (*Digabel and Lantuéjoul*, 1978; *Vincent and Soille*, 1991; *Parvati et al.*, 2008). Subsequently, certain regions of the image are selected as starting points (markers) in the "valleys" (regional minimum) from which the water level is increased until different water masses would connect, which provides the border of each "valley" (MCC cells). Further, there is the possibility to select regions that can not be flooded with markers as background pixels.

The other image segmentation method is the marker-based random walk segmentation (*Grady*, 2006). The random walk segmentation also requires a gray-scale image and markers that indicate the regional minima. The concept of this method is that every unmarked pixel releases a "random walker" to walk to each marked pixel and calculate the probability of which marked pixels the random walker is most like to reach first. The random walkers are biased to avoid crossing sharp intensities of pixels to account for more than pixel distance between marked and unmarked pixels. Similar to the watershed method, it is also possible to additionally mark regions that belong to the background.

A common issue of both methods is over-segmentation which means that too many segments are detected when every local minimum is considered as a marker (*Parvati et al.*, 2008; *Martini et al.*, 2014; *Gufan et al.*, 2016). To avoid this issue, the markers of each MODIS scene need to be selected carefully, as the number of markers defines the

number of cells. However, the markers must also be selected automatically to generate a global statistic. In the following, I describe how the markers are calculated.

Marker Selection

The scenes are already gray-scale images as I use only one band from the reflectance as input. To automatically select the markers of each MODIS scene, first, each scene is normalized to a range from 0 to 255 to fit the typical range of an RGB image. The step-by-step marker selection process is visualized in Fig. 14. All following image processing

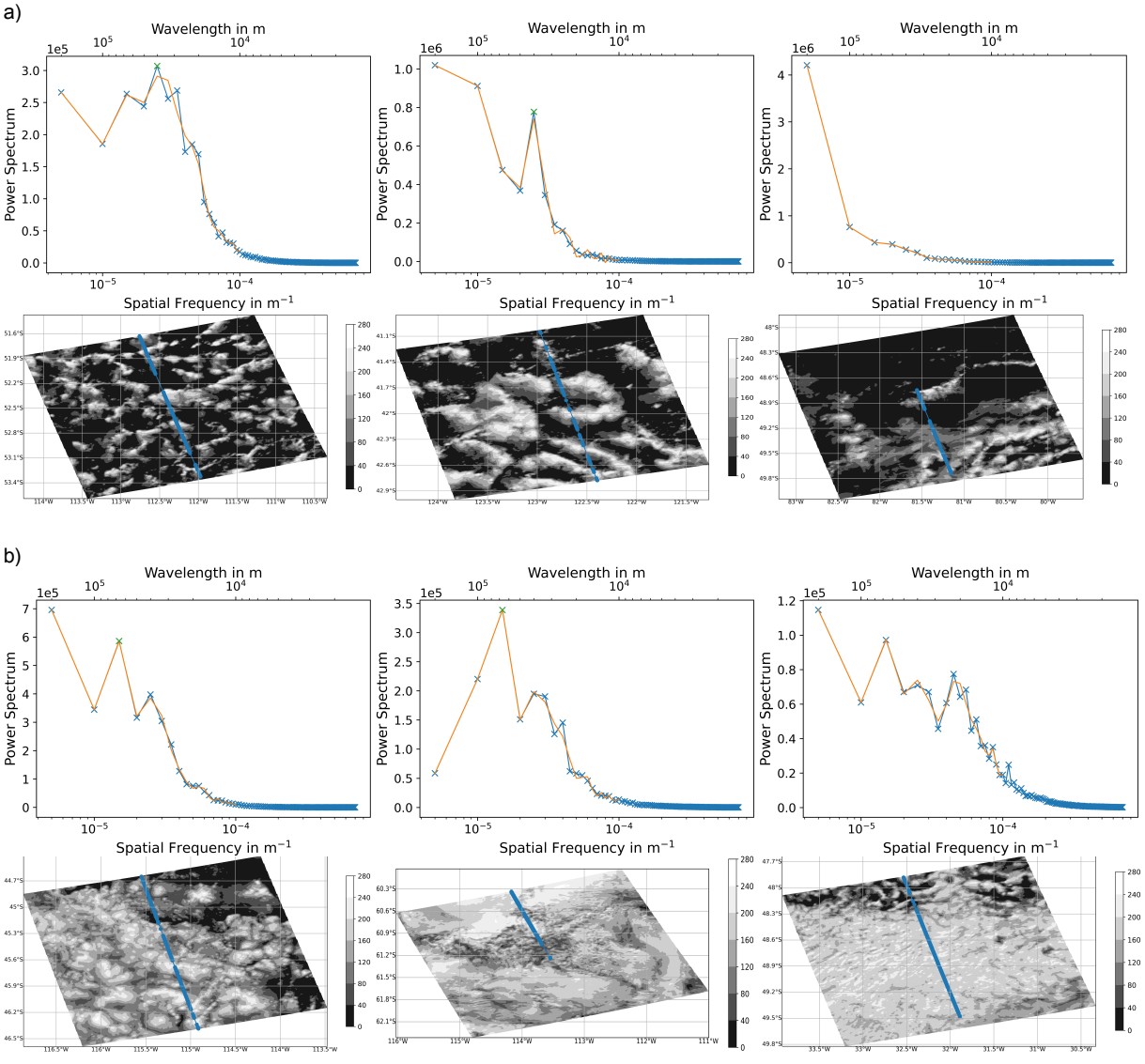

FIG. 13 (Top) Azimuthally averaged 1D power spectra of the 2D Fourier transformation of the (bottom) scenes for (a) open scenes and (b) closed scenes. The green crosses indicate peaks with a prominence of 100000. The left and middle scenes are segmented, while the right one is excluded due to the missing peak.

steps, including filtering, morphological transformations, and segmentation, are performed with the open-source Scikit-Image library in Python (*van der Walt et al.*, 2014) which is widely used in cloud detection studies (e.g., *Heikenfeld et al.*, 2019; *Yorks et al.*, 2021; *Janssens et al.*, 2021). To increase the contrast of the scenes, I normalize each scene's histogram, resulting in clearer lines (borders) of the cells. As I am not interested in detecting small turbulent details in the cells, I use a Gaussian low-pass filter with a standard deviation of 0.5, which is truncated based on the mean estimated cell diameter of each scene (*Martini et al.*, 2014). Estimating the cell diameter accounts for varying cell diameters with each scene. This estimation is calculated by finding the highest peak in the azimuthally averaged 1D power spectrum of the 2D Fourier transformation with a prominence of 100000. If a scene does not have a peak with this prominence, the scene is not further used and thus is not segmented. The prominence value is set to 100000 to avoid segmenting scenes without clear MCC structures, although classified as MCC scenes. In Fig. 13, a few example scenes and their power spectra are shown for open and closed MCC scenes. While this works very well in open scenes, there are still some more stratiform scenes of closed MCC which exhibit an identified peak in the power spectra (Fig. 13 b, middle). As these stratiform scenes are also segmented, this could lead to a bias in cell area and cause a larger cell diameter in the closed MCC clouds.

To further prepare the markers of the scenes, the scenes are binarized by a dynamic threshold calculated based on the mean of the neighboring pixels. The neighboring pixels are also defined by the estimated cell diameter. For open cell scenes, the binarization is inverted so that cloudy regions with values higher than the threshold are set to zero while values lower than the threshold (ocean regions) are set to one (Fig. 14). While ocean regions should be local minima and the cloud walls local maxima in open scenes at the end of this process (Fig. 15 a), due to the distance transformation, in the binary image, ocean regions have to be maxima and cloudy regions minima. While the reverse is true for closed scenes, in which the segmented cells should be over cloudy regions with the border over the ocean or lower intensities (Fig. 15 b). Thus, the binarization is not inverted in closed scenes.

Two morphological operations, opening and closing, are used on the binarized scenes (*Said et al.*, 2016; *Gufan et al.*, 2016). The morphological opening operation first uses erosion ($\ominus$) followed by dilatation ($\oplus$) to transform the input scenes (Img) with the same structuring elements (SE) see Eq. (2). Whereas closing has the reverse order, first dilatation followed by erosion (Eq. (3)).

$$\text{Opening} = \text{Img} \ominus \text{SE} \oplus \text{SE} \tag{2}$$

$$\text{Closing} = \text{Img} \oplus \text{SE} \ominus \text{SE} \tag{3}$$

The morphological transformation "erosion" erodes the foreground structures (pixels equal to one; white) by replacing any pixels with the background (pixels equal to zero;

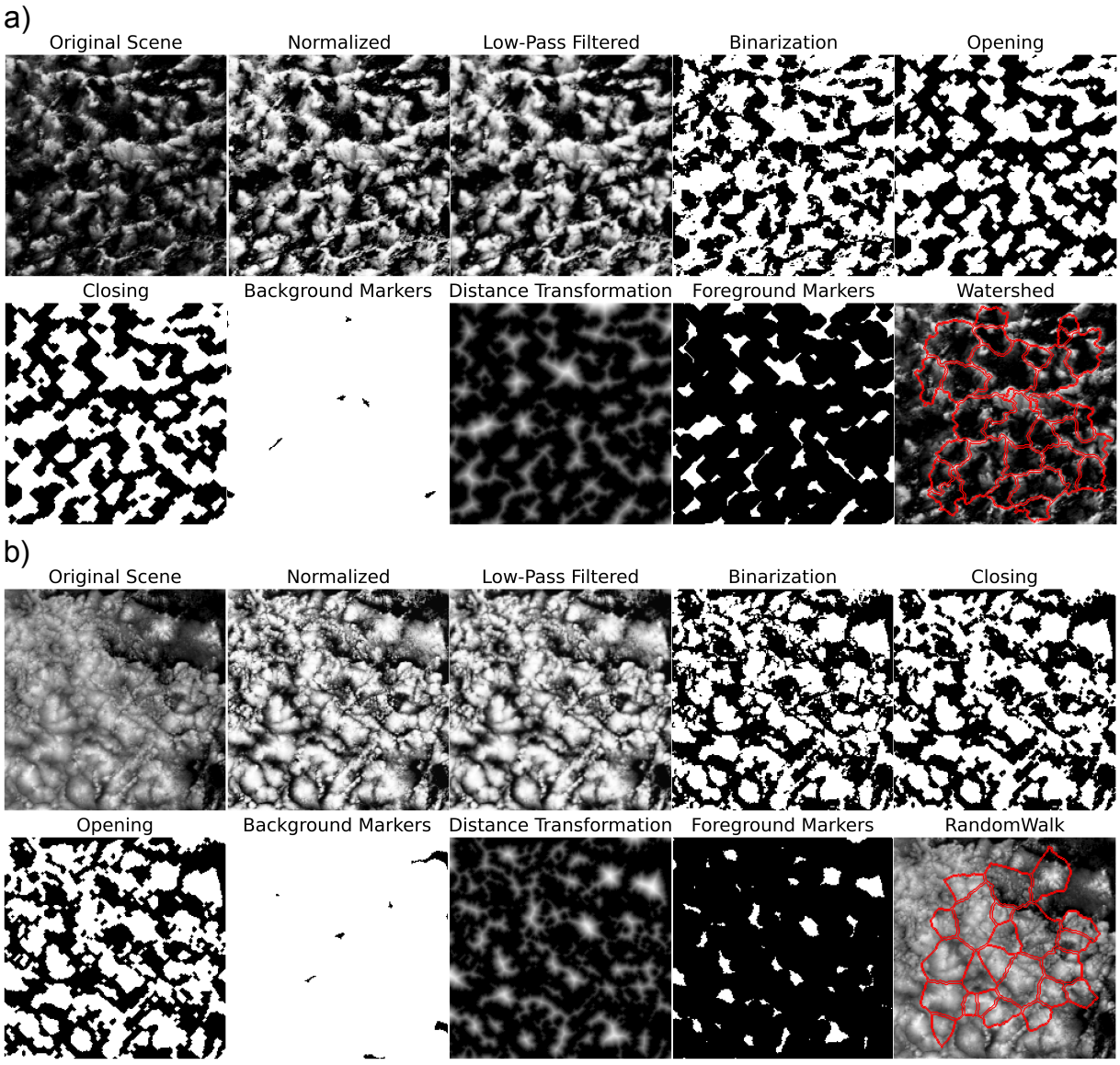

FIG. 14 Step-by-step marker selection process for examples scenes of Fig. 11 (a) open and (b) closed MCC scenes on February 3rd 2007. The step-by-step process follows the original scene, normalized histogram, low-pass filtered, binarization, (a) opening or (b) closing, (a) closing or (b) opening, distance transformation, background marker, foreground markers and segmentation with (a) watershed or (b) random walk.

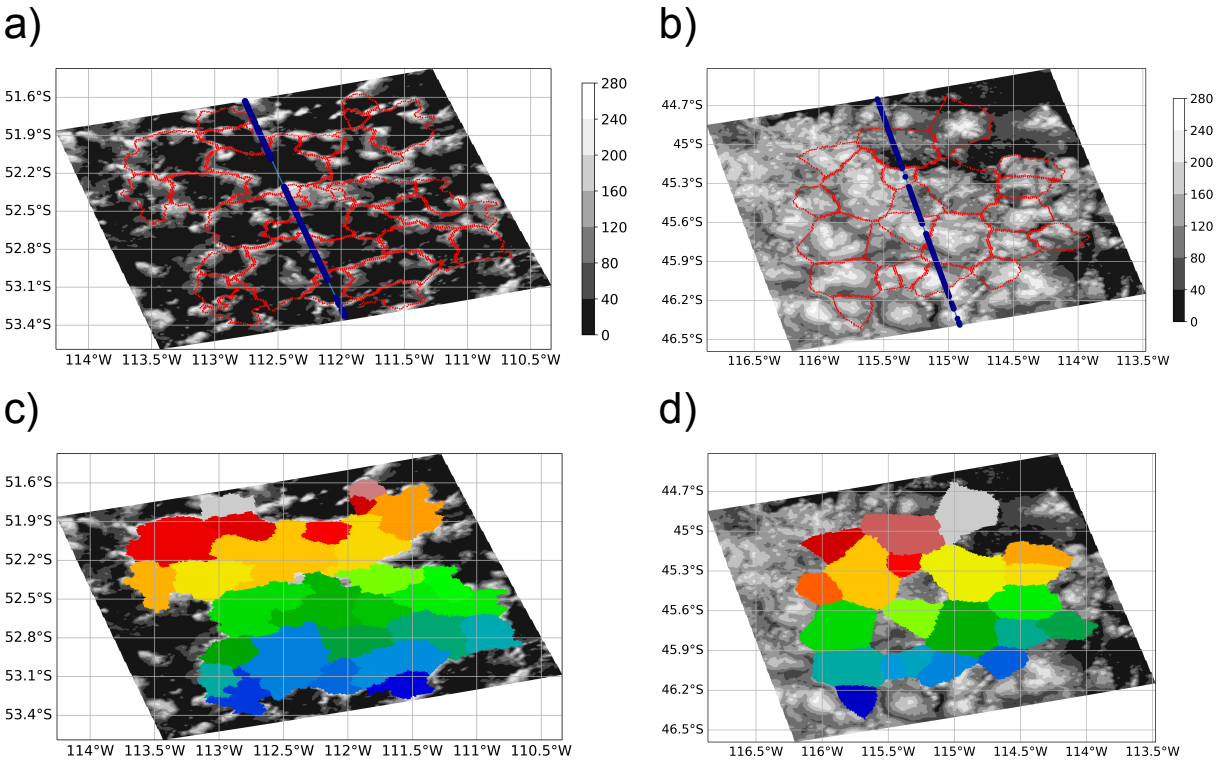

FIG. 15 (a, b) MODIS 0.86 µm reflectance of two example scenes of open and closed MCC regimes on February 3rd. The red borders indicate the identified MCC cells. (a) The open scene is segmented by the watershed image segmentation. (b) The closed scene is segmented by the random walker image segmentation. The dark blue dots on the blue line show the valid DARDAR data points on the track. (c, d) Filled cells to visualize the cells from the background.

black) if not all pixels under the structuring element are equal to one. On the other hand, the morphological transformation "dilatation" dilates the foreground structures by replacing any pixels with the foreground if any pixels under the structuring element are equal to one. In this way, opening removes foreground structures that are smaller than the structuring element, while closing removes background structures that are smaller than the structuring element. In each scene, both morphological operations are used. Open scenes are first transformed by opening and then closing with a disk-shaped structuring element with a radius of 2 pixels. In contrast, closed scenes are first transformed by closing, followed by opening with a disk-shape structuring element with a radius of 1 pixel. Thus, in both cases, I remove the noise in the cloudy areas and then in the ocean regions. The radii of the structuring elements are tested by visual inspection of a couple of test scenes. Due to the typically lower cloud fraction in open scenes, the radius is set to a larger value than in closed scenes.

To not segment the whole scene, especially when there are larger patches with no MCC organization, I will mark regions that can not be segmented and thus belong to

the background. Based on the final morphological transformation of the image (either closing for open or opening for closed scenes), I define the markers of the background in the segmentation. Therefore, this final morphological transformation of the image is dilated with a disk-shaped structuring element with a radius of 8 pixels. The radius of the structuring element is set to a relatively large value only to keep background pixels that have a distance greater than 8 km to any foreground pixels in the final morphological transformation. Any remaining connecting groups of background pixels with more than 3 pixels are used as a background maker. These small background pixel groups are discarded because they mostly result in very small and unrealistic background areas. The pixel group size is tested on multiple example scenes with a value of 3 pixels the most realistic background is achieved.

In the final step, I define the markers of the foreground by calculating the euclidean distance transformation of the final morphological transformation of the image. The maximum distance times the distance factor (open: 0.28; closed: 0.4) is used to calculate the threshold distance. The distance factor values are tested and visually verified by the resulting cell identification in multiple test scenes. In general, with an increasing distance factor, the number of identified cells decreases as fewer foreground markers remain. This could possibly bias the cell area of closed MCC cells to be larger, as the cells in scenes with too few cells might have an unrealistically large cell area. However, the different values for open and closed scenes are carefully considered and necessary to account for the more turbulent nature of the foreground area (cloudy area) in closed cells compared

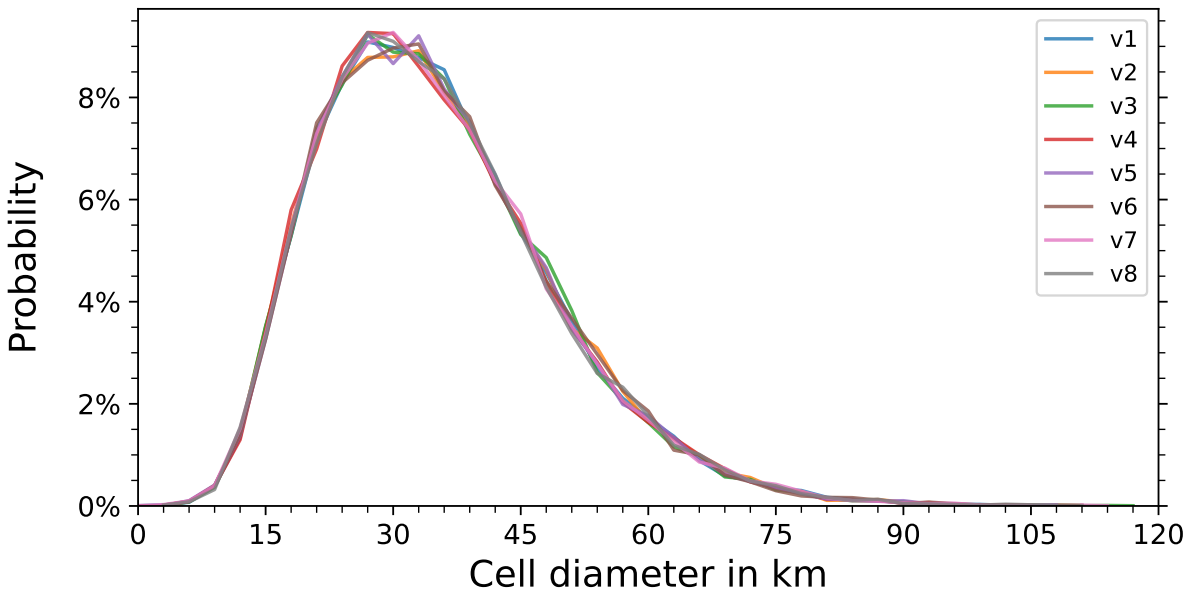

FIG. 16 Cell diameter probability density functions (PDFs) based on the eight versions of the cell identification.

to open cells (ocean area) shown in the distance transformation in Fig. 14. All pixels of the distance transformation larger than the threshold distance are set to one, while the rest is set to zero. Any remaining connecting groups of foreground pixels with more than 3 pixels are used as foreground makers, similar to the background markers.

Finally, during the image segmentation step, all scene pixels which do not belong to either foreground or background makers are segmented and labeled. The foreground markers label all cells, while the background markers all belong to the same background label. Examples of the cell identifications of the watershed segmentation for an open cell regime and the random walk segmentation for a closed cell regime are displayed in Fig. 15. Cells connected to a scene's border are removed to avoid a bias in the cell diameter.

To provide information about the uncertainties of this cell identification method, I repeatedly shift the start of cutting the scenes along the track by 25 km. This yields eight versions of the cell identification methods with slightly different scenes. Overall, the cell diameter distributions of the eight versions are very similar, as shown in Fig. 16.

Mean Cell Properties

As I investigate the cloud phase of the identified cells shown in Fig. 15, only the cells containing valid DARDAR data points are analyzed as they are located under the track. The cell diameter is the equivalent cell diameter depending on the cell area. To be consistent with the results from Chapter 3, the mean cloud properties of CTH, CTT, LWP, COT, in-cloud albedo and effective radius R_e are the means of all valid DARDAR points crossing a cell.

2.5.3 Rejection Rate

To test if mean cell properties (μ) are statistically different between two distributions, e.g., open and closed MCC cells, I introduce the rejection rate based on Welch's t-test. As I analyze eight different versions of the cell identification, Welch's t-test is performed individually for each version. Here, I use a two-tailed Welch's t-test which accounts for unequal variances and unequal sizes of the two samples with a significance level of 95% (*Welch*, 1938, 1947).

$$\begin{aligned} &H_0 : \mu_1 = \mu_2, && \text{if} \quad p \geq 0.05 \\ &H_1 : \mu_1 \neq \mu_2, && \text{if} \quad p < 0.05 \end{aligned}$$

The Null hypothesis H_0 is rejected if the p-values are below 0.05 and show that the mean

cell properties are significantly different in this version. To account for the eight versions, the rejection rate is the fraction of rejected versions for the identical test distribution properties in different versions. This means that all versions have statistically significantly different means for a rejection equal to one.

2.6 Global MCC Dataset

In order to obtain a global MCC climatology and to further verify the CNN described in the previous Section 2.4, I use the CNN to analyze the 0.86 µm reflectance band with a 1 km resolution from MODIS Aqua C6.1 (*Platnick et al.*, 2015) from 65° S to 65° N in 2008. For further details on the MODIS Aqua cloud product, see Section 2.5. Here, the longitude and latitude are not taken from the geolocation product (MYD03) but to save data storage, the 5 km resolution longitude and latitude from MYD06 are interpolated to 1 km.

To match the conditions the CNN is trained on, the MODIS granules are cut into scenes with a size of $224 \times 224\,\mathrm{km}^2$. The scan angle should be $<32°$ to retrieve reliable cloud top properties (*Menzel et al.*, 2010). This would result in taking the inner 881 pixels (s) of each granule which correspond to a scan angle (α) of 32° calculated by $s = 2 \cdot \mathrm{flight\_height} \cdot \tan\alpha$ with a flight height of 705 km of the MODIS instrument on the Aqua satellite. However, instead, I select the inner 896 pixels with a scan angle of 32.43° at the borders to fit four full scenes across the track. As the scenes are cut with an overlap of 112 km, each granule is cut into 119 scenes. Only low-level cloud scenes with a mean CTH $\leq$3.5 km in which all pixels are above the ocean are analyzed by the CNN model. The longitude and latitude in the center of each scene are saved along with one of the three CNN categories: Open, Closed, NoMCC. To retrieve the global statistic, all scene centers are binned into a 5° x 5° grid. The MCC frequency occurrence is the percentage of occurrences of open or closed MCC scenes to the total number of all low-level cloud scenes in each bin.

3 Exploring Relations Between Cloud Morphology, Cloud Phase, and Cloud Radiative Properties in Southern Ocean's Stratocumulus Clouds

3.1 Stratocumulus Climatology

Cloud morphology and reflectivity are vertically integrated quantities of a 2D cloud field. In order to explore the links between morphology, phase, and their combined potential relation to cloud albedo, a vertically integrated categorization for cloud phase was built (Fig. 17) as described in Section 2.2. Here, we address the quality and limits of our vertically integrated cloud phase and their seasonal differences. Further, the possible connections between cloud phase and organization are investigated.

According to our cloud-phase classifications, most MPCs are characterized by a *Mix* cloud layer with ice-phase precipitation below cloud base in the SO, whereas commonly in the SO, many MPCs are described as consisting of a supercooled liquid top with ice precipitation below in satellites studies (e.g., *Hu et al.*, 2010; *Morrison et al.*, 2011; *Huang et al.*, 2012; *Ahn et al.*, 2018; *Mace et al.*, 2021) and also by some ground-based and in situ measurements (e.g., *Shupe et al.*, 2008; *Niu et al.*, 2008; *D'Alessandro et al.*, 2021; *McFarquhar et al.*, 2021). Note that spaceborne studies can be based either on passive instruments which typically only cover the cloud-top phase (*Morrison et al.*, 2011) or on active instruments like lidar or radar (*Hu et al.*, 2010; *Huang et al.*, 2012; *Ahn et al.*, 2018; *Mace et al.*, 2021) which can penetrate layers below cloud top. Recently, the comparison of active satellites from CALIPSO or CloudSat with ground-based or in situ measurements shows that their products underestimate the occurrence of MPCs in the SO (*Ahn et al.*, 2018; *Mace et al.*, 2021). This is further supported by many field campaign studies that observe the presence of ice in the supercooled top layer, even at relatively high CTT ($> -5\,^{\circ}\mathrm{C}$) in MPCs (e.g., *Huang et al.*, 2017; *Ahn et al.*, 2017; *Lang et al.*, 2021; *Zaremba*

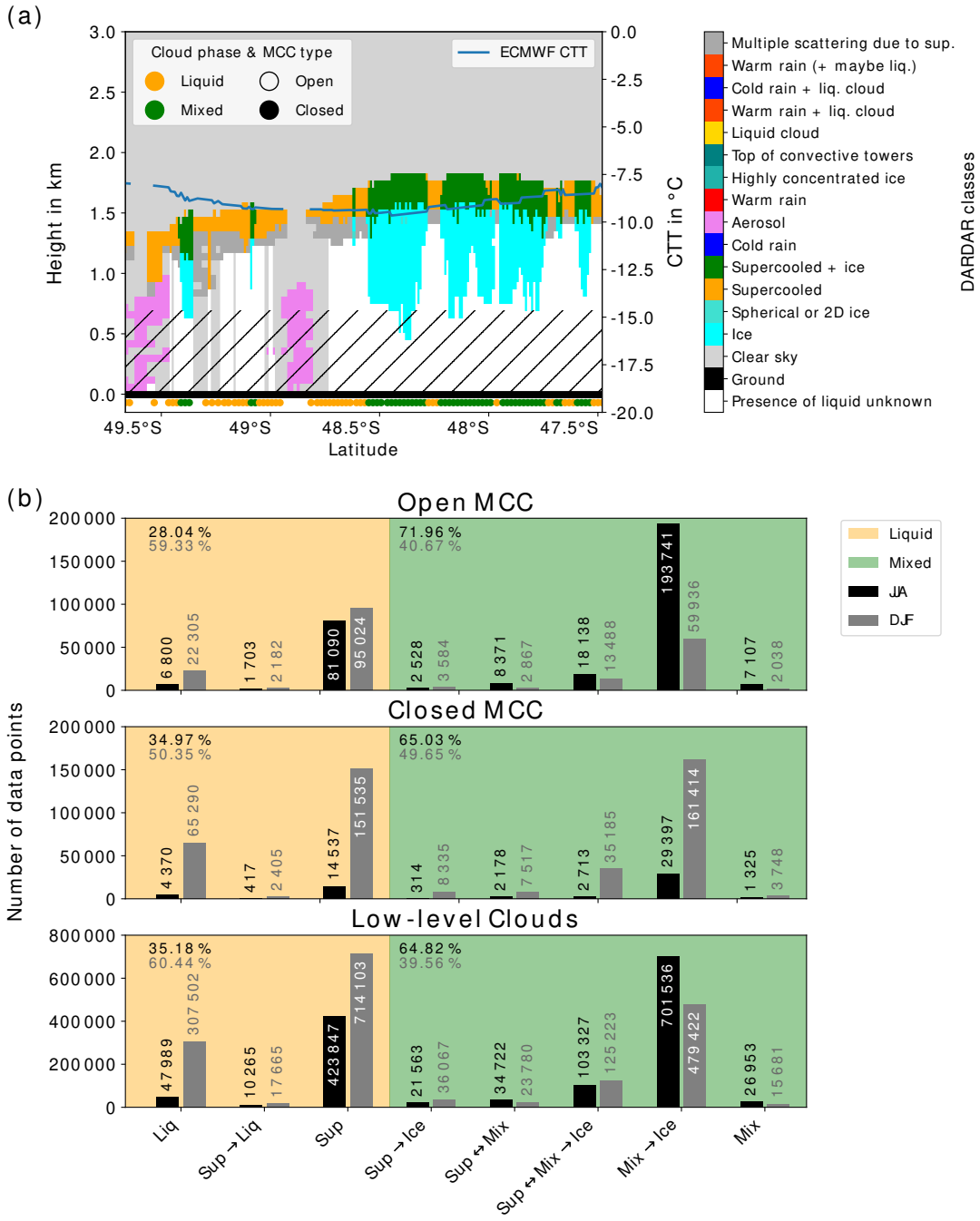

FIG. 17 (a) Example track of the DARDAR categorization on December 1, 2007. The hatched area displays levels below 720 m. The colored circles below the ground show our vertically integrated cloud-phase classification and the MCC type for every second data point.
(b) Histogram of data points of vertically integrated cloud-phase subcategories divided into liquid clouds (orange) and MPCs (green) for JJA (black) and DJF (gray) from 2007 to 2010. The overall percentage of liquid clouds and MPCs is indicated in each panel separately for JJA (black) and DJF (gray). The layer on top of the next is indicated by "→" and interchangeable layers are indicated by "↔".

et al., 2021). The previous version of DARDAR (v1) shows a tendency to detect too many liquid or supercooled liquid pixels in the lower troposphere (*Ceccaldi et al.*, 2013). As the study by *Huang et al.* (2012) uses the DARDAR v1 product, they find more supercooled liquid-topped MPCs which is likely due to the bias in the DARDAR v1 cloud classification algorithm.
While most of our MPCs (more than 95%) contain a *Mix* layer that is determined by both the radar (ice) and the lidar (supercooled liquid), we also include *Sup* over *Ice* clouds in our MPC classification. This category is the most uncertain as the phase distinction between ice and rain is solely based on the wet bulb temperature (frozen $< 0\,^{\circ}\mathrm{C}$) once the lidar has saturated and only radar retrieval is available (*Delanoë and Hogan*, 2008; *Ceccaldi et al.*, 2013). Thus, these clouds could also be pure supercooled liquid clouds with or without freezing rain below cloud base (see Section 2.2). The impact of this possible misclassification only marginally affects our MPC classification, as most MPCs contain a *Mix* cloud layer and further excluding them did not substantially alter our results.

Of our liquid low-level clouds, about 90% in austral winter and 60% in summer are supercooled at cloud top and almost all of them (99%) belong to the *Sup* category and thus remain supercooled at cloud base in the SO. We identify almost no low-level liquid clouds that show DARDAR rain categories below cloud base (∼0.5%). However, the DARDAR algorithm was not primarily designed to detect precipitation and as the CloudSat radar is contaminated by surface clutter, only heavy and moderate drizzle can be detected at heights below roughly 720 m and 860 m, respectively (*Marchand et al.*, 2008). Thus, for many liquid low-level clouds which have a CTH of around 1.2 km (Fig. 18 g–h) light drizzle rates at cloud base could have been missed at lidar saturation which explains the too low drizzle rates. If we define precipitating clouds as clouds with an effective radius of $R_e > 14\,\mu\mathrm{m}$ then roughly 10% and 3% of low-level liquid clouds are precipitating in winter and summer, respectively (Fig. S4 a and c). These values are in agreement with *Mülmenstädt et al.* (2015) who show that the rain probability of liquid clouds at all levels is roughly 10% at 45° S and 3% at 60° S. Though they use DARDAR v1 to identify the cloud phase, they use the 2C-PRECIP-COLUMN product based on retrievals from CloudSat to calculate rain probability. Further, this latitudinal gradient in precipitation is also reported by *Mace et al.* (2021) who investigate MPCs with satellite and ground-based measurements. They also show that about 33% of MPCs in the SO produce supercooled precipitation. We find similar values of 30% (winter) and 40% (summer) of MPCs that have $R_e > 14\,\mu\mathrm{m}$ (Fig. S4 a and c). Additionally, we find that on average liquid low-level clouds are 57% optically thinner than their mixed-phase counterparts calculated independent of season and thus are more unlikely to contain sufficient water content to generate precipitation. As most liquid clouds are optically thin and are not precipitating,

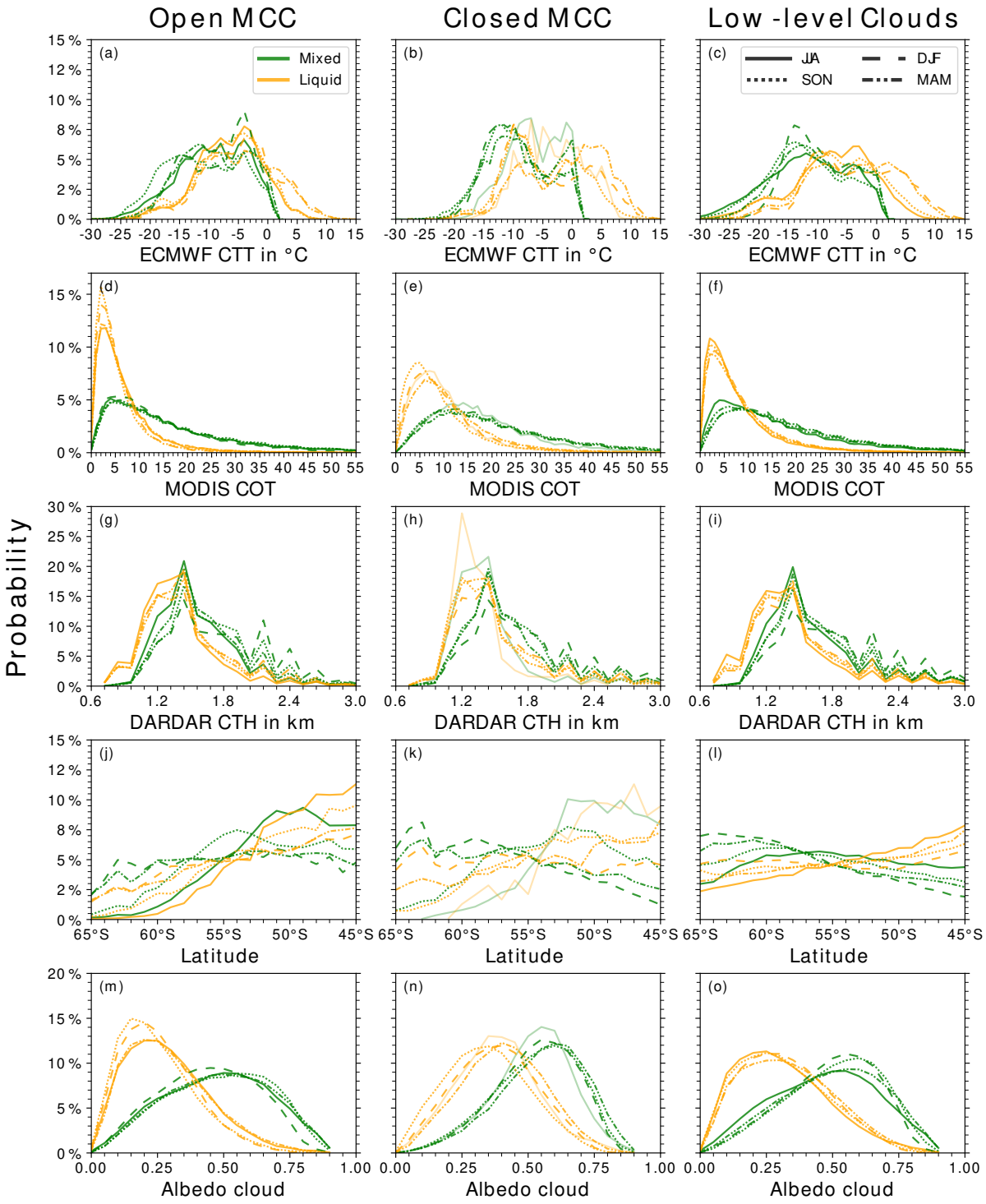

FIG. 18 Seasonal PDFs of (a–c) CTT, (d–f) COT, (g–i) CTH, (j–l) latitude and (m–o) cloud albedo for (left) open MCC, (middle) closed MCC, and (right) low-level clouds with bin width of 1 °C, 1, 120 m, 1° and 0.05, respectively. The PDFs are normalized for each cloud regime type, phase and season individually. In JJA only 5.1% of the annual closed MCC clouds occur, and therefore closed MCC in JJA are indicated by more transparent color shading.

especially in summer, this could either hint towards a mixed-phase detection bias in DARDAR, which we find unlikely as discussed above, or suggest that most optically thicker supercooled liquid clouds generate ice and become MPCs. Interestingly, liquid (and supercooled liquid) closed MCC clouds are optically thicker than open and low-level clouds. This could indicate a potential link between cloud phase and cloud morphology, however, as discussed below we find no further evidence for this link.

To further investigate the quality of the cloud phase classification, we also examine the CTT range. Figures 18 a–c display the probability density functions (PDFs) of CTT, which are normalized individually for each cloud phase and season. The normalization is also performed separately within all panels. In low-level clouds, the CTT range spans from −30 °C to 15 °C in liquid clouds and from −30 °C to 3 °C in MPCs in the SO (Fig. 18 a–c). We note that the reason for the occurrence of MPCs above 0 °C is related to the fact that in the radar mask of the DARDAR v2 algorithm, the wet-bulb temperature of 0 °C is used as a threshold (*Delanoë and Hogan*, 2010; *Ceccaldi et al.*, 2013). Seasonal changes in the CTT range are mainly found in the maximum temperature of liquid clouds above 0 °C. These temperature ranges of MPCs and liquid clouds are in agreement with other satellite studies of the SO (*Morrison et al.*, 2011; *Mason et al.*, 2014). The low-level MPCs occur most often at around −15 °C. This peak corresponds to the temperature of the growth habit of dendritic ice crystals and secondary ice processes from ice-ice collisional break-up (*Riley and Mapes*, 2009; *Mignani et al.*, 2019).

Overall, we observe a seasonal shift from predominantly MPCs (∼65%) during austral winter to predominantly liquid clouds (∼60%) during austral summer (Fig. 17). *Listowski et al.* (2019) also use the DARDAR v2 product and exhibit in their Fig. 8 that during both austral winter and summer, low-level liquid clouds occur more often than MPCs in the SO. However, in their analysis, they include low-level clouds in the range of surface cluttering which leads to limitations in identifying ice at those heights and thus could lead to a bias towards liquid clouds. If we visually confine the analysis of *Listowski et al.* (2019) to heights above 780 m in austral winter, the occurrence of MPCs is more pronounced. Thus, our findings are consistent with them if clouds with higher uncertainty in cloud phase distinction are excluded.

In addition to the seasonal cycle in cloud phase, we observe a seasonal cycle in MCC regime. As previous studies show, the predominant MCC regime shifts from open cell MCC during austral winter to closed cell MCC during summer (*Muhlbauer et al.*, 2014; *McCoy et al.*, 2017). Open cell MCC is found relatively homogeneously across the year with the lowest rate of occurrence in austral summer (16%) and the highest rate of occurrence in winter (24.4%). Meanwhile, closed cell MCC display a strong seasonal shift. *McCoy et al.* (2017) explained this seasonal shift in MCC occurrence with the varying

strength and frequency of occurrence of MCAOs. Merely 5.1% of all closed cell MCC are found in austral winter while 40.5% of all closed cell MCC occur in summer. This results in fewer than 100 clouds per 1 °C CTT bin in some bins in austral winter. Thus, if the austral winter closed MCC clouds are further subdivided by other variables e.g. CTT, CTH, or Lat, their climatology might not yield sufficient data points for a reliable statistical analysis which is indicated by more transparent colors in that panel or season in our figures (Fig. 18 b,e,h,k,n, 19, 20, and 21).

In general, both MCC regimes exhibit a similar CTT distribution (Fig. 18 a and b). Mixed-phase MCC clouds feature one peak at around −4 °C in all seasons which is especially strong in austral summer, and a second peak at roughly −15 °C which is more pronounced in closed cells. The first peak falls in the temperature range (−3 °C to −8 °C) of secondary ice production by the Hallet-Mossop process (*Hallett and Mossop*, 1974). While the second peak at −15 °C is found in many ice formation studies (*Magono*, 1962; *Takahashi et al.*, 1995; *Libbrecht*, 2005; *Mignani et al.*, 2019; *Sullivan et al.*, 2018; *Silber et al.*, 2021a), multiple ice processes can occur at this temperature range. This second peak will be extensively discussed in Section 3.2. We note that in MCC clouds the CTT range only extends down to about −20 °C to −25 °C, which is likely caused by the condition of the MCC algorithm that cloud tops need to be within 30 °C of the surface temperature (*McCoy et al.*, 2017). Further, we only identify small cloud phase seasonal changes in open and closed MCC clouds compared to the overall low-level cloud statistic (Fig. 18 c). During austral winter, we see slightly more open MPCs than low-level MPCs and during austral summer more closed MPCs.

We observe that the seasonal decrease in cloud occurrence south of 60° S is stronger in MPCs than in liquid clouds (Fig. 18 l). This is consistent with *Listowski et al.* (2019), who also find that the occurrence of MPCs is reduced to a larger degree than that of liquid clouds. This behavior is likely related to seasonal differences in sea ice extent (not shown). This connection between the sea ice edge and low-level cloud fraction is also found in other studies (*Taylor et al.*, 2015; *Wall et al.*, 2017; *Morrison et al.*, 2018). Further, the latitudinal difference in cloud organization shows that in the open cell regime, the decrease of cloud occurrence in both MPCs and liquid clouds is more substantial than in low-level clouds (Fig. 18 j). This might also be impacted by the sea ice extent as open MCC clouds are correlated with MCAOs (*McCoy et al.*, 2017), which shift equatorward in austral winter along with the sea ice edge. During austral winter, we observe a detection limit in the MCC regimes south of 60° S, as the algorithm is based on the passive MODIS Aqua satellite instrument, which depends on solar insolation for measurements. However, we do not find it likely that this limit impacts our hypothesis as the reduction of cloud occurrence at latitudes closer to the pole also appears in austral spring, which is

not impacted by this detection limit.
Overall, we are confident that our cloud phase classification of MPCs contains ice and that we can therefore trust our phase classification. Further, the climatology of SO stratocumuli as characterized by DARDAR v2 did not display any evidence that organization and cloud phase are interlinked in the full climatology. Although, we observe that closed cells remain in the SLC regime at higher COT than observed for open cell and low-level clouds.

3.2 Link of Freezing Behavior and Cloud Phase

In this section, we analyze whether different predictors of ice occurrence in stratocumuli display varied behavior in differently organized clouds. From these analyses, we can determine whether there are statistical relationships that suggest that individual freezing processes vary in their effectiveness in clouds characterized by different cloud dynamics.
Here, we analyze the cloud phase fraction between MPCs and SLCs. Their cloud phase fractions (mixed fraction and supercooled liquid fraction) are defined as the number of MPC or SLC pixels divided by their sum. The cloud phase dependence on CTT has already been studied by several other publications to find a relationship between ice formation and CTT (e.g. *Bühl et al.*, 2013; *Zhang et al.*, 2014, 2015; *Silber et al.*, 2021b,a). Thus, we restrict our analysis for the rest of this study to a CTT range from −20 °C to 0 °C. We choose this temperature range as most clouds in the open and closed MCC regime have CTTs above −20 °C. This restriction does not affect the overall distribution of MPCs and liquid clouds except for the fact at we remove all pure liquid clouds (Fig. S4). Therefore, this analysis is restricted to MPCs and clouds containing a supercooled liquid layer or only supercooled liquid, referred to as SLCs.

Overall, the mixed fraction is much higher in austral winter at the same CTT than in summer for all three investigated cloud regimes (Fig. 19). This seasonal increase in mixed fraction during austral winter could either be caused dynamically or due to increased INP availability at colder temperatures. An increase in surface fluxes or higher surface wind speeds in austral winter could indicate a dynamic reason. However, we did not find substantial seasonal changes in either SST or surface wind speed (Table 3). As described in Section 3.1 we find an equatorward shift of MPCs in austral winter (Fig. 18, Table 3). However, we find that the mixed fraction at the same CTT is independent of latitude (Fig. 20). Further, we find that the same CTTs are reached at lower CTHs in

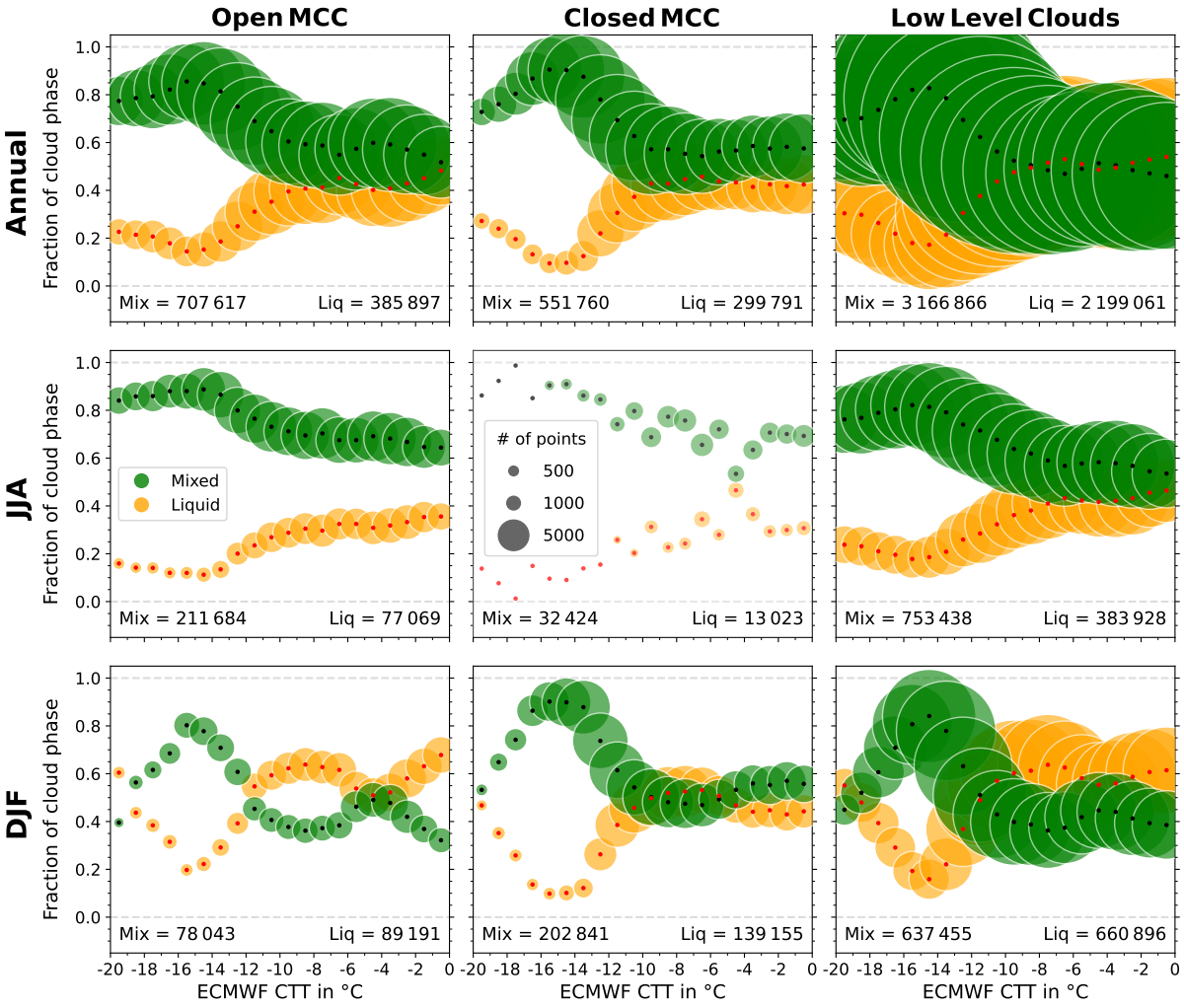

FIG. 19 Supercooled liquid and mixed fraction binned by CTT from −20 °C to 0 °C with a bin width of 1 °C (2007 - 2010) for (top) all seasons, (middle) austral winter and (bottom) austral summer in (left) open MCC, (middle) closed MCC, and (right) low-level clouds. As only 5.1% of the annual closed MCC clouds occur in JJA the panel is displayed in more transparent color shading.

austral winter than in summer (Fig. S5 and S1). Thus, we hypothesize that the vertical distribution of INP might influence the seasonal difference in mixed fractions. *McCluskey et al.* (2019) investigate the simulated vertical INP distribution based on observational data from the Clouds, Aerosols, Precipitation, Radiation, and atmospherIc Composition Over the southeRN ocean campaign (CAPRICORN) and show that independent of the season the INP concentration in the SO is higher closer to the surface as the main source of INP is sea spray aerosols (*Burrows et al.*, 2013; *DeMott et al.*, 2016; *Vergara-Temprado et al.*, 2017; *Huang et al.*, 2021a). Further, Fig. 4 of *McCluskey et al.* (2019) displays that the INP concentration is slightly lower (∼35% at the surface, ∼55% at around 3 km) at all heights in austral winter than in summer. Nonetheless, we find a higher mixed fraction

TABLE 3 Geometric mean and standard deviation factor of different cloud properties during austral winter and summer in the CTT range from −20 °C to 0 °C. The mean values are calculated separately for open MCC, closed MCC, and low-level clouds which are further subdivided into MPCs and SLCs. [The geometric standard deviation factor is shown in brackets and should be interpreted as a range from "geomean/geostd" to "geomean*geostd"].

		CTH in km	**Lat** in °S	**SST** in K	**Wind** in m s^{-1}	**LWP** in g m^{-2}	**COT**	**Alb**$_{cld}$
JJA								
Open	**MPC**	1.57 (1.22)	48.17 (1.10)	279.7 (1.01)	11.14 (1.45)	151.5 (2.29)	13.19 (2.52)	0.45 (1.64)
	SLC	1.41 (1.24)	47.15 (1.10)	280.6 (1.01)	10.52 (1.51)	47.0 (2.12)	5.38 (2.26)	0.27 (1.75)
Closed	**MPC**	1.49 (1.25)	48.38 (1.10)	278.6 (1.01)	9.10 (1.56)	164.8 (1.89)	15.98 (1.97)	0.52 (1.41)
	SLC	1.43 (1.27)	48.34 (1.10)	279.0 (1.01)	7.78 (1.67)	63.1 (1.95)	8.02 (1.96)	0.36 (1.55)
Low-Level	**MPC**	1.60 (1.25)	51.44 (1.13)	277.8 (1.02)	10.49 (1.55)	146.4 (2.29)	12.93 (2.53)	0.45 (1.66)
	SLC	1.43 (1.29)	49.66 (1.13)	279.0 (1.02)	9.46 (1.66)	48.7 (2.21)	5.81 (2.34)	0.28 (1.77)
DJF								
Open	**MPC**	1.78 (1.27)	52.68 (1.13)	279.5 (1.01)	10.76 (1.48)	95.8 (2.65)	11.22 (2.30)	0.42 (1.61)
	SLC	1.56 (1.30)	51.72 (1.12)	279.9 (1.01)	10.18 (1.48)	27.0 (2.36)	4.52 (2.08)	0.24 (1.72)
Closed	**MPC**	1.79 (1.28)	56.60 (1.10)	276.2 (1.01)	9.50 (1.60)	136.7 (2.21)	16.59 (1.99)	0.52 (1.41)
	SLC	1.64 (1.28)	56.14 (1.11)	276.2 (1.01)	8.63 (1.61)	52.3 (2.28)	8.73 (2.05)	0.37 (1.58)
Low-Level	**MPC**	1.84 (1.28)	56.21 (1.12)	276.6 (1.01)	9.08 (1.65)	114.7 (2.52)	14.12 (2.18)	0.48 (1.53)
	SLC	1.61 (1.31)	55.08 (1.12)	277.2 (1.02)	8.36 (1.68)	37.7 (2.52)	6.50 (2.23)	0.31 (1.73)

in MCC and all low clouds for CTTs above −12 °C at CTHs between 1.4 km and 2.3 km which decreases with higher CTHs (Fig. S1). Surprisingly, this behavior is not observed during austral summer. Therefore, we suggest that the increase in mixed fraction in austral winter is related to the higher mixed fraction at CTHs between 1.4 km and 2.3 km. But it remains unclear what is causing this effect as higher INP concentration closer to the surface is also found in austral summer (*McCluskey et al.*, 2019) which does not show a higher mixed fraction at lower CTHs.

In austral summer, the mixed fraction remains below 0.5 for temperatures higher than −12 °C with a secondary peak at around −5 °C in open MCC and all low-level clouds. Surprisingly, this peak is not observed in closed MCC clouds. This could potentially be related to a detection bias close to 0 °C as the mixed fraction at temperatures above −10 °C is lower for clouds with 0 µm < R_e <14 µm (Fig. S2). However, even for clouds with 0 µm < R_e <14 µm this secondary peak is barely detectable and much weaker than in open MCC and all low-level clouds. This secondary peak in open MCC and all low-level clouds in the mixed fraction occurs at temperatures at which the secondary ice production by the Hallet-Mossop process is especially active (*Hallett and Mossop*, 1974). A recent study by *Silber et al.* (2021a) in the Arctic also shows that the liquid water occurrence in clouds reduces at roughly −6 °C and −15 °C. They conclude that this is caused by a more efficient vapor growth of ice at these temperatures. Moreover, their second minimum at

−15 °C corresponds to the strong increase in the mixed fraction from −12 °C to −16 °C that we find for all cloud regimes in austral summer and the annual mean. This increase occurs across all latitudes in the SO (Fig. 20) and is also seen in austral winter, though due to the overall higher mixed fraction in winter, the increase is not as pronounced. This peak in ice formation at roughly −15 °C is found in several studies (*Magono*, 1962; *Takahashi et al.*, 1995; *Libbrecht*, 2005; *Mignani et al.*, 2019; *Sullivan et al.*, 2018; *Silber et al.*, 2021a), though there are different reasons for this increase in the numbers of ice crystals. *Takahashi et al.* (1995) find that ice-ice collisional break-up (secondary ice formation) favors this temperature range at roughly −15 °C. Further, *Mignani et al.* (2019) investigate whether an ice crystal that grows at temperatures between −12 °C and −17 °C forms due to primary or secondary ice formation. They find that only every eighth ice crystal contains an INP and thus that secondary ice formation is more important at this temperature range. Another possible way of ice formation at this temperature range would be droplet shattering. However, a modeling study by *Sullivan et al.* (2018) shows that droplet shattering seems to play only a minor role for clouds with a cloud base temperature below 12 °C (285 K) as the droplets cannot grow to a sufficient size to shatter. As our data set does not include INP information, we cannot determine which ice processes are causing the mixed fraction at −15 °C to increase.

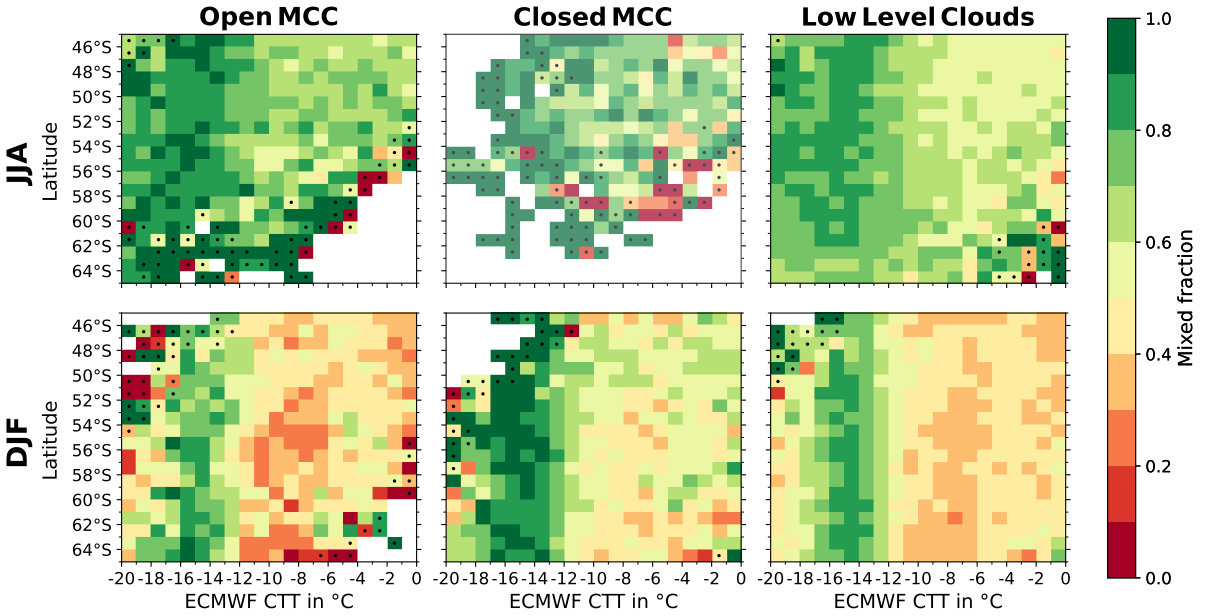

FIG. 20 Two-dimensional histograms of mixed fraction against CTT and latitude for (left) open MCCs, (middle) closed MCC, and (right) low-level clouds in austral (top) winter and (bottom) summer. Dotted bins indicate bins with less than 50 data points. As only 5.1% of the annual closed MCC clouds occur in JJA the panel is displayed in more transparent color shading.

At temperatures below −16 °C, there is a strong decrease in mixed fraction in all cloud regimes during austral summer which is less pronounced in the annual mean and austral winter. We suggest that the cause for the reduction in mixed fraction is due to a rapid glaciation of MPCs at these temperatures due to updraft or moisture limitation. A strong increase in fully glaciated clouds at these temperatures is found by *D'Alessandro et al.* (2021) who base their study on data from the Southern Ocean Clouds Radiation Aerosol Transport Experimental Study (SOCRATES) and cover the time period from 15 January to 28 February 2018. Figure 4 of *D'Alessandro et al.* (2021) shows that at roughly −17 °C the relative occurrence frequency of MPCs and SLCs decreases along with temperature, whereas the frequency of ice clouds increases rapidly at this temperature. Further, a direct comparison of SOCRATES flight observations from *D'Alessandro et al.* (2021) with our mixed fraction in Fig. S6 shows a similar trend across the CTT range in low-level clouds during January and February, though our mixed fraction shows higher values than the in-cloud flight measurements. *D'Alessandro et al.* (2021) discuss the underestimation of MPCs due to a detection limit of small ice particles (<50 µm) by the instruments. Further, their cloud phase has a spatial resolution of about 150 m, depending on the aircraft's velocity (*D'Alessandro et al.*, 2021), while our cloud phase classification has a 1.1 km resolution. Thus, one data point of our cloud phase classification would be subdivided into seven samples of their cloud phase. Further, *D'Alessandro et al.* (2021) investigate mixed-phase transects, which consist of 20 cloud phase samples, and find that these are more likely heterogeneous than other phase transects. This suggests that the mixed fraction depends on the spatial resolution of the data. Further supported by comparing the annual fractions of MPCs to SLCs in each cloud pixel (Section 3.2) to an entire cloud cell (Section 4.1), which reveals an increase in the mixed fraction from 65% in both open and closed cloudy data points to 86% in closed and 92% in open MCC cells. Thus, the direct comparison of satellite data and in-flight observations supports the rapid glaciation of MPCs at temperatures below −16 °C as soon as ice is formed via the Wegener-Bergeron-Findeisen process. *D'Alessandro et al.* (2021) suggest that this is caused by the activation of INP at these temperatures. On the other hand, we find it unlikely that CTH-dependent INP limitation is the primary cause for the decrease in mixed fraction below −16 °C at high CTHs as it seems to be unaffected by CTH (Fig. S1). Our analysis shows that the mixed fraction during austral winter is not decreasing as strongly as in summer. As a temperature-dependent activation of INP should not change with season this cannot fully explain the seasonal differences we observe. Therefore, we do not think this is a result of different INP activation within these clouds, but we propose that the supercooled liquid water is depleted due to an increased decoupling of the marine boundary layer.

In agreement with the findings of Section 3.1, the mixed fraction of closed MCC clouds

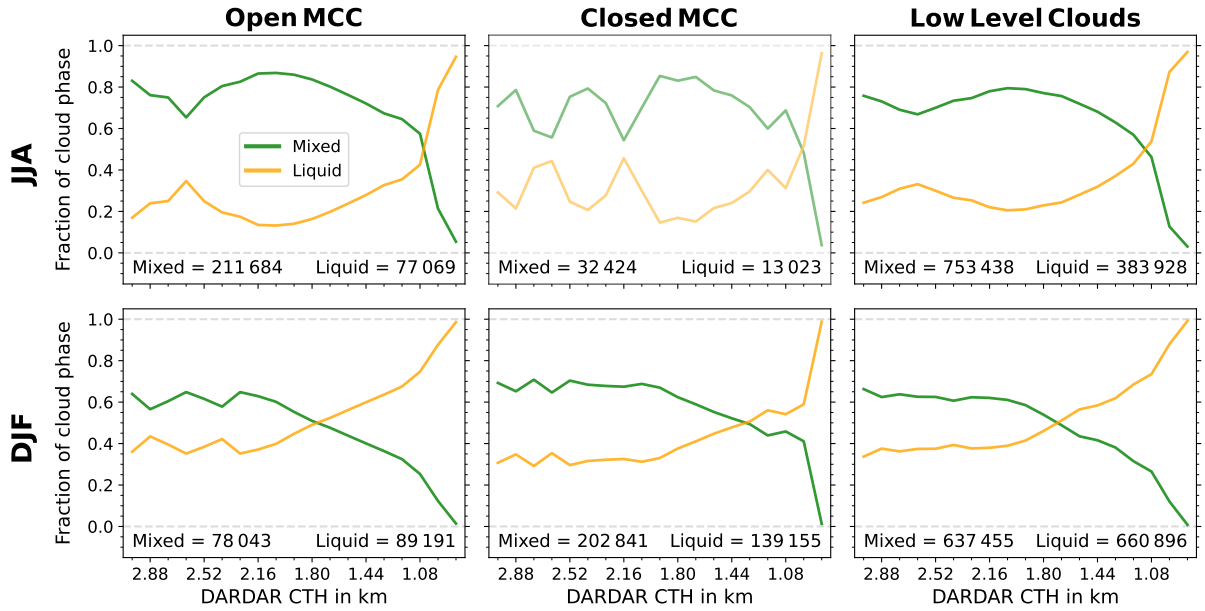

FIG. 21 Supercooled liquid and mixed fraction binned by CTH from 0.78 km to 3 km with a bin width of 0.12 km (2007 - 2010) during austral (top) winter and (bottom) summer for (left) open MCC, (middle) closed MCC, and (right) low-level clouds. As only 5.1% of the annual closed MCC clouds occur in JJA the panel is displayed in more transparent color shading.

is higher than that of open MCC clouds. *Abel et al.* (2017) show that transitions between closed and open cells in the Northern Hemisphere extratropics may be driven by precipitation as opposed to a pure boundary layer deepening. This idea is further supported by findings from *Tornow et al.* (2021) who introduce the idea of preconditioning by ice-phase processes, which accelerate the precipitation-driven transition. Early onset of precipitation by riming processes and subsequent sublimation trigger an earlier boundary layer decoupling and preconditions the boundary layer for an earlier transition. If preconditioning would be a dominant process in stabilizing the sub-cloud layer and forcing closed-to-open transitions, one would expect this to manifest in phase statistics across the two morphological regimes. However, mixed fraction curves (Fig. 19) and phase statistics show little changes with respect to cloud morphology. As the LWP:IWP ratio cannot be detected reliably in the used satellite retrievals, the mixed fraction might include MPCs with a very low ice ratio. *Eirund et al.* (2019a) find that the impact of ice formation on cloud morphology in simulated open MCC clouds is only apparent for a ratio of LWP:IWP of 1:2, which could influence our statistics. However, any differences detected in the mixed fraction are small in comparison to seasonal changes in cloud phase, which are driven by other factors than mesoscale organization. Thus, a prevalence of open MCC clouds towards MPCs, which would be consistent with accelerated transitions from closed to open MCC clouds through precipitation is not found.

We also investigate the dependence of mixed-phase occurrence upon CTH. Typically, the cloud depth is a better indicator for thermodynamic or dynamic changes in the boundary layer or radiative changes in stratocumulus clouds than the CTH (*Wood et al.*, 2008; *Bretherton*, 2015). However, even though we derive a liquid CBH to reduce the contamination of surface clutter from the radar, this CBH is highly biased in the distance from CTH because the lidar signal will be fully attenuated in clouds with a COT greater than 3.5 (*Delanoë and Hogan*, 2008). Thus, the geometrical cloud depth would also be biased as most clouds have a COT greater than 3.5 (Fig. 18 d–f). Nevertheless, the CTH might still give some insight to surface forcing and the mixing strength in the boundary layer (*Bretherton et al.*, 2010).

In general, we observe that the mixed fraction increases with CTH from roughly 0 to around 0.6 to 0.8 in all cloud regimes and during both austral winter and summer (Fig. 21). We find seasonal differences in the height at which the mixed fraction surpasses the supercooled liquid fraction. This height is lower during austral winter. As clouds with CTHs below 1 km can only have a small vertical extent, this could potentially lead to a bias towards SLC occurrence at CTHs below 1 km as thicker clouds tend to form ice as discussed in Section 3.1. However, this is the same for all seasons and cloud morphologies. Thus, differences across seasons and between open and closed cells can still be interpreted. Further, we show that MPCs appear at higher CTHs than SLCs in all cloud regimes (Table 3). This is in agreement with a field campaign study in the Arctic that shows that MPCs tend to have higher CTHs than SLCs (*Achtert et al.*, 2020). The mean CTHs between open and closed MCC clouds are similar during austral summer, whereas during austral winter at least for MPCs we see higher CTHs in open cells. Many studies show that there are CTH differences between the two morphological regimes with higher CTHs in open MCC clouds (*Muhlbauer et al.*, 2014; *Glassmeier and Feingold*, 2017; *Jensen et al.*, 2021). A study using ground-based and satellite observations in the Eastern North Atlantic shows that closed MCC clouds have a lower mean CTH (*Jensen et al.*, 2021). Further, *Glassmeier and Feingold* (2017) demonstrate in a large-eddy simulation that open cells favor deeper boundary layer heights and thus also higher CTHs. In global data, *Muhlbauer et al.* (2014) reveal that the mean CTH in open MCC clouds is about 100 m higher than in closed cells which is similar to what we see in MPCs in austral winter. However, they also investigate the mean CTH in SO which did not show a substantial mean CTH difference between open and closed cells.

Deeper boundary layers associated with higher CTHs are often decoupled and favor conditional instabilities associated with stronger vertical updrafts which in turn favor ice growth and potentially ice formation through secondary ice processes. This is shown by a SOCRATES study from *Wang et al.* (2020) which investigates generating cells in the

SO and show that within these generating cell updrafts ice particles occur more often and are also larger than outside. Thus, this favors ice precipitation inside the updraft cores. Further, they still find substantial amounts of ice outside the generating cells which suggests that turbulent mixing in the boundary layer is important to reduce differences between inside and outside of the updrafts. The stronger precipitation within updrafts is also confirmed by large eddy simulations (e.g. *Keeler et al.*, 2016; *Zhou et al.*, 2018; *Young et al.*, 2018; *Eirund et al.*, 2019b). The updraft strength can also vary depending on the organizational regime. *Wood et al.* (2011) analyze the updraft strength in MCC regimes in a case study over the Southeast Pacific and show that while open cells can reach higher updraft velocities, closed cells also exhibit moderate updrafts. Apart from the updrafts, the CTH and MPC occurrence also depends on the sources of mixing in the stratocumulus-topped boundary layer. Therefore, we test for indicators of surface-generated turbulence such as SST and ΔT (difference between SST and 2 m air temperature). However, neither variable displayed the expected trend (not shown). Thus, if there is a correlation between ice occurrence and vertical acceleration, it does not seem to be driven by surface fluxes (Fig. S7). We cannot evaluate the importance of cloud-top-generated turbulence and cloud-scale overturning circulations for CTHs in SO stratocumuli due to data limitations. However, *Lang et al.* (2022) show that cloud top generated mixing, especially in closed MCC affects the occurrence frequency during the diurnal cycle. Further, they find that wind shear due to the relatively large climatological near-surface winds in the SO may also be a stronger generator of boundary layer turbulence than in other regions. Overall, this could suggest that the mechanisms of mixing (turbulence and circulation) may play a larger role in CTH than previously thought (*McCoy et al.*, 2017).
In summary, our analysis shows that across regimes of varied subsidence, clouds that form in likely decoupled layers requiring moderate updraft cloud cores to be maintained are more likely to sustain ice formation in mixed-phase stratocumuli. Our analysis of the different freezing behavior across cloud morphologies further supports our climatological findings, which show that the sustained ice formation in MPC stratocumuli does not primarily depend on cloud morphology but is constrained by other environmental factors.

3.3 Relationship between Cloud Phase, Cloud Morphology, and Cloud Albedo

Here, we examine how cloud phase and cloud morphology may change the cloud albedo in the SO. The cloud albedo physically depends on the LWP and cloud droplet number

concentration (in liquid clouds). Variations of cloud phase, cloud fraction, and different organizational regimes can alter the LWP and the cloud droplet number concentration and hence, impact cloud albedo and COT. For the same total water content, liquid clouds typically have a higher cloud albedo than ice clouds, because liquid water droplets are smaller than ice crystals, and thus reflect more incoming solar radiation due to their greater surface area. Thus, the cloud albedo in MPCs varies depending on the phase partitioning of supercooled liquid and ice (*McCoy et al.*, 2014a,b). Further, any optically thick cloud ($\mathrm{COT} > 10$) typically contains ice, which suggests that clouds with a substantial LWP can sustain ice formation. Consistently, we find that the LWP and COT of MPCs are much higher than those of SLCs independent of organizational regime and season (Table 3). This is in agreement with other studies, which also show that supercooled liquid layers in MPCs are much thicker than in pure (supercooled) liquid clouds (*Shupe et al.*, 2006; *Achtert et al.*, 2020). In austral winter, both mixed-phase MCC clouds have a similar LWP. Whereas in austral summer, open MPCs have a lower LWP than mixed-phase closed cells. We should note that the MODIS LWP algorithm used here does not distinguish between MPCs and liquid clouds and retrieves the LWP as based on a liquid cloud. Therefore, the LWP in MPCs is likely overestimating the true LWP. This can lead to an overestimated LWP of about 15% for stratiform MPCs (*Khanal and Wang*, 2018). Not only the cloud phase influences the cloud albedo but also the cloud fraction and cloud morphology. *Loeb et al.* (2007) determine that the variability of all-sky albedo from the Clouds and the Earth's Radiant Energy System (CERES) is dominantly controlled by variations in cloud fraction. The cloud fraction of closed MCC regimes is typically higher than in open MCC regimes (*Muhlbauer et al.*, 2014). Moreover, *McCoy et al.* (2017) investigate differences in the cloud fraction albedo relation between open and closed MCC clouds and show that, in general, closed MCC clouds have a higher albedo. Additionally, they exhibit that even for the same cloud fraction, the cloud albedo of closed MCC clouds is about 0.05 higher on average than the albedo of open MCC clouds. Our analysis of in-cloud albedo confirms their findings that closed cells are more reflective than open cells (Table 3). In addition, we also see that in-cloud albedo differences between closed and open cells are even stronger in SLCs (JJA: 0.09, DJF: 0.13) compared to MPCs (JJA: 0.07, DJF: 0.10). This is caused by stronger differences between optically thin ($\mathrm{COT} < 10$) open and closed cells in SLCs compared to MPCs. Whereas in open cells roughly 80% of the SLCs are optically thin, in closed cells about 45% have COT values larger than 10. Differences in in-cloud albedo ranging between 0.07 to 0.13 correspond to a cloud-radiative effect of $21\,\mathrm{W\,m^{-2}}$ to $39\,\mathrm{W\,m^{-2}}$ when assuming typical solar insolation of $300\,\mathrm{W\,m^{-2}}$ in the SO. Thus, a reduction in ice-phase occurrence in a warming climate is likely to impact open-cell clouds more strongly than closed-cell clouds changes in clouds with larger op-

tical depth have a weaker impact on cloud scene albedo. Further, we find a considerable seasonal change in in-cloud albedo in open cells, which is not observed in closed cells. This is even stronger in open MPCs than in SLCs. This seasonal decrease of the in-cloud albedo in open clouds is correlated with a strong decrease in LWP from austral winter to summer.

4 Investigating the Dependence of Cloud Phase and Cloud Albedo on Spatial Scales of MCC Cells

This chapter investigates the cell properties of open and closed MCC clouds in the SO with a particular focus on their spatial scale in the annual mean and all seasons (JJA, SON, DJF, MAM). To obtain the equivalent cell diameter of MCC clouds, I use the cell identification method based on image segmentation of a MODIS reflectance band as described in Section 2.5. Further, I explore whether cell diameter and aspect ratio differences relate to ice formation and, thus, cloud phase. Similar to Sections 3.2 and 3.3, I restrict the CTT from −20 °C to 0 °C to focus on the mixed-phase regime in this chapter. Moreover, Section 4.2 analyzes the dependence of the cloud albedo on the aspect ratio.

4.1 Spatial Scale of MCC Cells and Cloud Phase

Overall, 90% (5^{th} to 95^{th} percentile) of open MCC clouds have a cell diameter between 18 - 65 km in the SO, while 90% of closed MCC clouds have a cell diameter between 18 - 59 km. This shows that while both organizational regimes exhibit the same 5^{th} percentile of 18 km, open MCC clouds exist as larger cells than closed MCC cells. Open MCC cells are statistically significantly larger than closed cells about 1 km in the annual mean (Tables 4 and 5). Further, open MCC clouds are larger than closed cells in all seasons but only statistically significant in austral spring (SON) and summer (DJF). The largest mean cell diameters occur in summer for both open and closed MCC clouds, with open cells being 3 km larger than closed cells. This increase in the mean cell diameter in summer is mostly caused by an increase in cells with a very large diameter (>80 km) as displayed in Fig. 22. As discussed in Section 2.5.2, there might be a bias towards larger closed MCC cells as some more stratiform scenes are segmented as closed scenes and further due to the larger distance factor compared to open scenes. In addition, due to the scene selection process (Section 2.5.1), open cells might be biased to a lower cell diameter as scenes with large cell diameters and a low cloud fraction might not be passed to the segmentation.

Table 4 Annual and seasonal mean cell diameters in km for JJA, SON, DJF, and MAM in SLCs and MPCs with CTT from −20 °C to 0 °C.

	Open	**Closed**	**Open**		**Closed**	
			MPC	SLC	MPC	SLC
Annual	37.19	36.04	37.17	37.42	36.04	36.01
JJA	35.04	33.20	34.99	36.17	32.96	35.02
SON	37.70	35.42	37.82	36.70	35.31	36.24
DJF	40.52	37.21	40.82	39.24	37.39	36.33
MAM	37.23	36.24	37.25	37.06	36.43	35.29

Table 5 Rejection rates based on hypothesis tests of the eight versions for the null hypothesis of $\mu_1 = \mu_2$ equal mean of cell diameter (shown in Table 4) for six different tests indicated by columns. A rejection rate of 1.0 indicates that all versions have statistically significantly different means. See Section 2.5.3 for more information on the rejection rate.

		Open	**Closed**	**MPC**	**SLC**
	Open vs Closed	MPC vs SLC	MPC vs SLC	Open vs Closed	Open vs Closed
Annual	1.0	0.125	0.0	1.0	0.5
JJA	0.75	0.125	0.375	0.75	0.0
SON	1.0	0.125	0.25	1.0	0.0
DJF	1.0	0.25	0.375	1.0	0.5
MAM	0.5	0.172	0.25	0.5	0.25

However, while this bias might influence the true mean cell diameter of open and closed cells, it should not affect the significantly larger open to closed MCC clouds. A previous study shows that the cell size scales with the MBL height (*Wood and Hartmann*, 2006) and finds that closed MCC cells have a larger mean field cell diameter at the same MBL height. Meanwhile, *Glassmeier and Feingold* (2017) exhibit that open MCC clouds favor deeper MBLs in contrast to closed MCC clouds and, thus, show that open cells have a larger cell diameter. This is supported by *Jensen et al.* (2021), who also observed that open MCC clouds have higher CTH and, therefore, occur at deeper MBLs. These findings are consistent with the results of larger open cells than closed cells. Further, *Lang et al.* (2018) exhibit the highest MBL with a height of 2 km in SON closely followed by DJF with height of 1.8 km at the Macquarie Island (54.62° S, 158.85° E) in the SO. Seasonal changes in the MBL height are also examined by *Chan and Wood* (2013), showing the strongest seasonal anomalies in MBL height in DJF and the lowest in JJA in the SO. The seasonal differences between *Lang et al.* (2018) and *Chan and Wood* (2013) might be due to the spatial differences of comparing station data with the entire SO. Thus, the season with the deepest MBL from *Chan and Wood* (2013) matches the seasons with the largest cells and the season with the lowest MBL with the smallest cell sizes for closed and open

MCC clouds. In conclusion, the larger open MCC clouds compared to closed cells are in agreement with other studies (*Glassmeier and Feingold*, 2017; *Jensen et al.*, 2021).

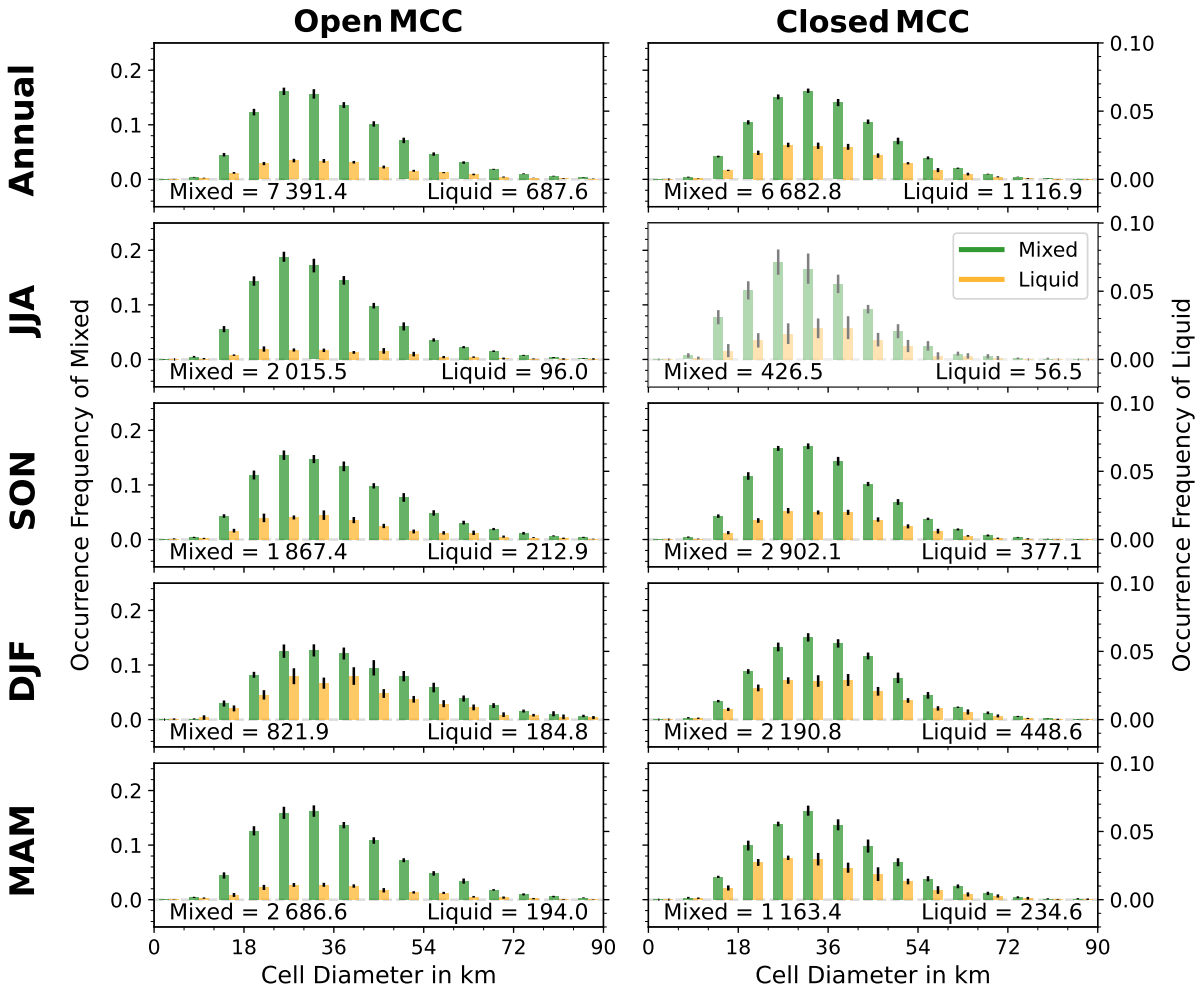

FIG. 22 Histogram of cloud phase occurrence frequency binned by cell diameter with a bin width of 6 km for CTT from −20 °C to 0 °C normalized by the sum of SLCs and MPCs. Note different y-axes for SLCs and MPCs. Numbers below the histogram indicate the mean number of identified cells for MPCs and SLCs. As only 6% of the annual closed MCC clouds occur in JJA, the panel is displayed in more transparent color shading.

To investigate the difference in the cell diameter between different cloud phases, Table 4 provides the mean cell diameters of MPCs and SLCs for open and closed MCC cells, respectively. In the annual mean, both open and closed cells show only minimal (<0.25 km) and statistically insignificant differences between MPCs and SLCs. The seasonal differences between MPCs and SLCs are in general larger up to ∼2 km in open and closed MCC clouds (e.g., JJA: closed MPC: 32.96 km and closed SLC: 35.02 km). Interestingly, I find that in austral summer (DJF), open and closed MPCs are larger than their SLC counterparts. At the same time, the reverse occurs in austral winter (JJA), where the

mean cell diameter of SLCs is larger compared to MPCs in both MCC regimes. These contrasting seasonal means explain why the annual means are indifferent. Further, the seasonal cell diameter differences within MPCs are considerably larger in open (difference between DJF and JJA: 5.8 km) and closed (4.5 km) cells than within SLCs (open: 3.0 km; closed: 1.3 km). This might be caused by the much higher occurrence of MPCs in JJA compared to SLCs (Fig. 22). This shows the importance of seasonal differences in the two MCC regimes as already observed in Section 3.2. Although the seasonal differences are stronger between MPCs and SLCs than in the annual mean, they are statistically insignificant in most of the eight versions (Table 4). However, this is most likely influenced by the substantially lower number of SLCs compared to MPCs in both regimes (Fig. 22). While the cell sizes of open and closed MCC clouds are investigated by other studies (*Agee et al.*, 1973; *Atkinson and Wu Zhang*, 1996; *Wood and Hartmann*, 2006; *Wang and Feingold*, 2009b), differences in the cell diameter depending on the cloud phase are only examined in open MCC clouds in an idealized large eddy simulation of a case study in the Arctic by *Eirund et al.* (2019a) in March (boreal spring). They find that open MPCs are about 2 km larger than open SLC caused by stronger cold pools induced by stronger precipitation in MPCs. This supports the findings of slightly larger open MPCs in austral spring (SON: 1 km), summer (DJF: 1.6 km), and fall (MAM: 0.2 km). However, as the differences are comparatively small to the mean cell diameter, the ice formation in closed and open MPCs only weakly affects the cell size in seasonal means.

While differences in the cell diameter between open and closed MPCs are statistically significant (Table 5, 4. column), this is not the case for SLCs. However, in both MPCs and SLCs, the cell diameter is larger in open than closed MCC cells in the annual and seasonal means. Thus, cloud phase distribution in the two morphological organizations can not explain the differences in cell sizes between open and closed MCC clouds.

To investigate further why open cells are larger than closed cells and the seasonal differences depending on cloud phase, the cell diameter against the CTH is displayed in Fig. 23. The aspect ratio is the ratio between cell diameter and CTH. *Wood and Hartmann* (2006) show that in open and closed MCC clouds, the aspect ratio is between 40:1 to 30:1 in the northern and southern parts of the subtropical East Pacific in shallow MBLs (<1.4 km), but this ratio breaks down for MBL heights above 1.5 km or cell diameters above 50 km. This is further supported by *Zhou et al.* (2021) showing that this constant aspect ratio only holds for shallow MBL heights in open and closed MCC clouds and that for cell size larger than 40 km, the mean MBL height is not varying with cell size. I exclude clouds with very shallow CTHs (<780 m) due to surface cluttering which influences the cloud phase detection ability (see Section 2.2 and Fig. 24). The mean cell diameter is almost constant with CTH in open and closed cells in the SO (Fig. 23), which is in agreement

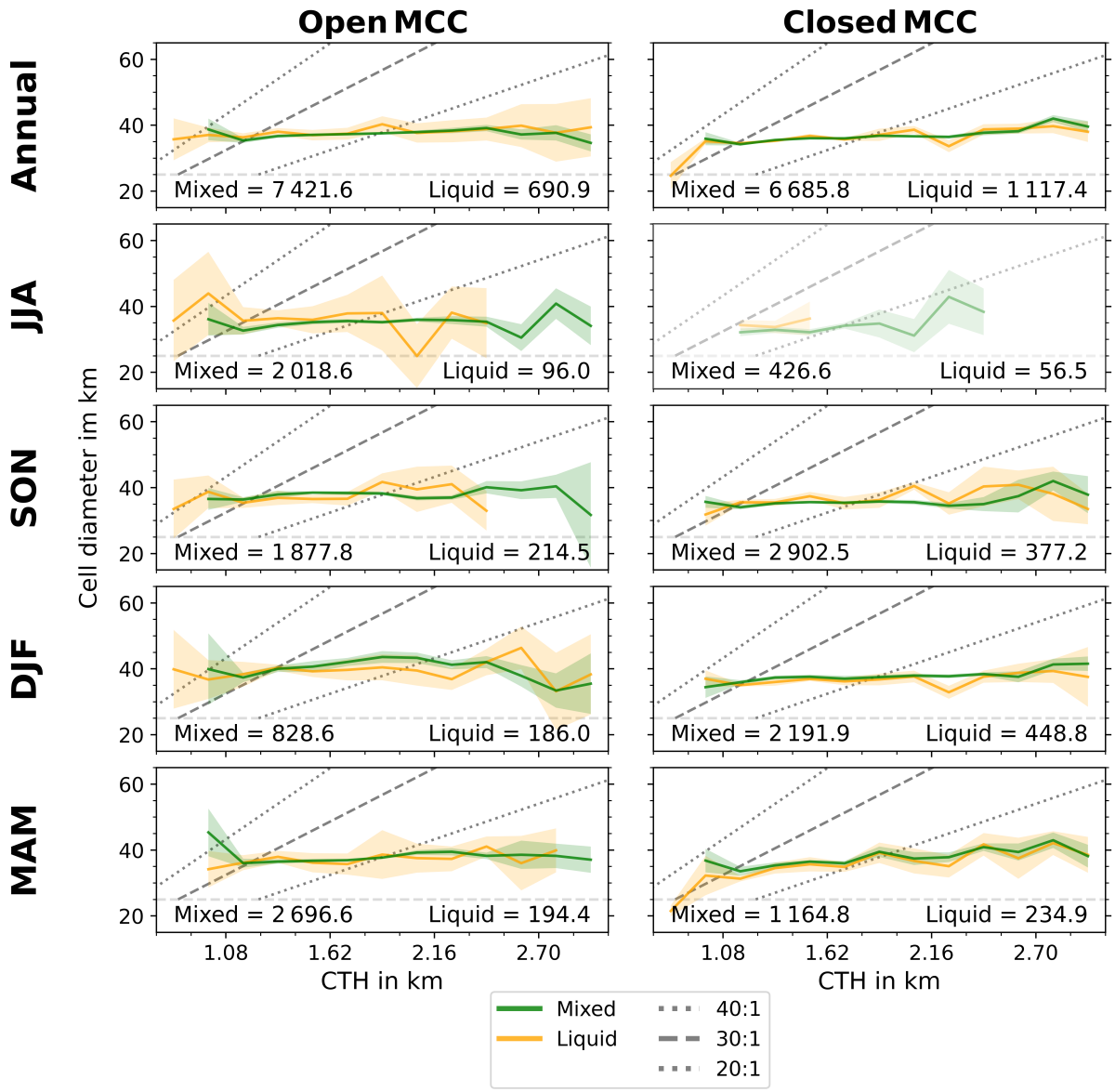

FIG. 23 Mean cell diameter as a function of CTH for SLCs and MPCs with CTT from −20 °C to 0 °C. The constant aspect ratios of 40:1, 30:1, and 20:1 are indicated as grey lines from top to bottom, respectively. Numbers below the lines indicate the mean number of identified cells for MPCs and SLCs. As only 6% of the annual closed MCC clouds occur in JJA, the panel is displayed in more transparent color shading.

with the results for deeper MBLs by other studies (*Wood and Hartmann*, 2006; *Zhou et al.*, 2021).

To further analyze the cloud size dependence on the cloud organization and phase, I investigate the aspect ratio to account for changes in CTH in single cloud cells (Tables 6 and 7). In the annual mean, SON, and DJF, open MCC clouds exhibit significantly larger aspect ratios than closed MCC cells. This means that larger open MCC cells than closed

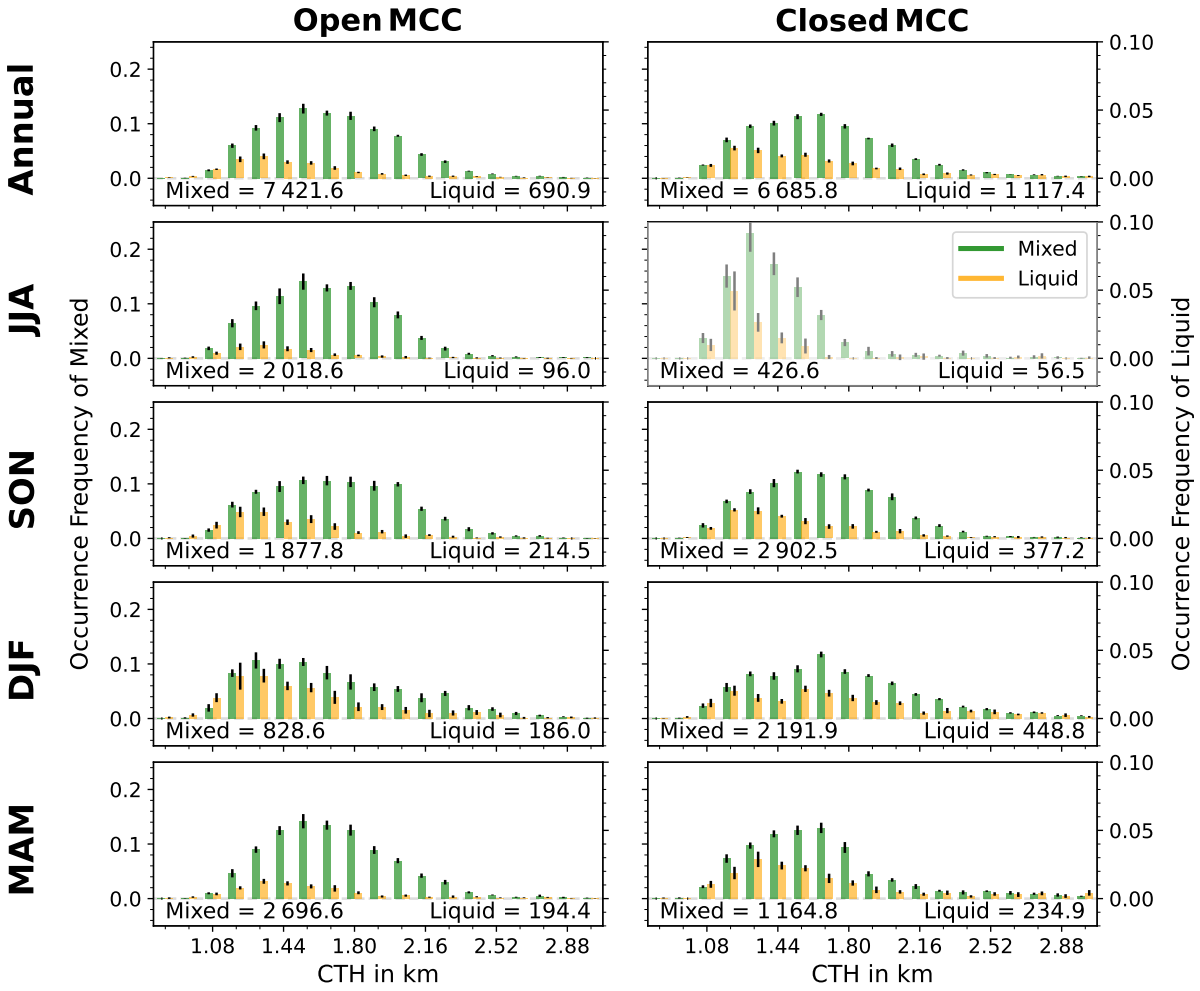

FIG. 24 Histogram of cloud phase occurrence frequency binned by CTH with a bin width of 120 m for CTT from −20 °C to 0 °C normalized by the sum of SLCs and MPCs. Note different y-axes for SLCs and MPCs. Numbers below the histogram indicate the mean number of identified cells for MPCs and SLCs. As only 6% of the annual closed MCC clouds occur in JJA, the panel is displayed in more transparent color shading.

cells occur independently of CTH (compare Tables 4 and 6). The mean aspect ratio of closed MCC cells is statistically significantly larger than that of open cells in austral winter (JJA), even though their mean cell diameter is smaller. This is caused by low CTHs (<1.3 km, see Fig. 24) of closed MCC cells in austral winter. As indicated by the more transparent color shading for closed MCC clouds in JJA, only a few cells are identified in JJA due to the lower occurrence frequency of closed MCC in winter months (Sections 3.2 and 5.2). However, as CTH and aspect ratio distributions in JJA diverge strongly from the other seasons and the annual mean (Figs. 24 and S8), I further investigate the cell aspect ratio with a different MCC classification to reduce the segmentation biases due to the MCC classification. Therefore, I use the same segmentation method (Section 2.5.2),

but the MCC type is based on most occurring MCC type in the 1°×1° gridded product of the CNN using the MODIS 0.55 µm reflectance band developed by *Yuan et al.* (2020). The mean aspect ratios and its histogram for the year 2007 are shown in Tables S1 and S2 and Fig. S9. Due to the substantially lower occurrence frequency of open MCC cells in the 1°×1° MCC data set (*Yuan et al.*, 2020; *Mohrmann et al.*, 2021) compared to the scene-based MCC data set used here (*Wood and Hartmann*, 2006; *Muhlbauer et al.*, 2014; *McCoy et al.*, 2017; *Eastman et al.*, 2021), less than 200 open cells are detected compared to almost 7000 closed cells in one year. Thus, I only compare the aspect ratios of closed MCC clouds of the two segmentation data sets with different MCC classifications. The aspect ratio distribution in JJA with the 1°×1° MCC data set is similar to the other seasons of this data set (Fig. S9) and the scene-based MCC data set (Fig. S8). Further, the mean aspect ratio in JJA is 21.65 and, thus, lower in the 1°×1° MCC data set and more comparable to the other seasons. It remains unclear why the scene-based MCC data seems to exhibit a tendency towards very low CTHs in closed MCC clouds in winter in the SO, but it might be unrealistic as this behavior is not found in the 1°×1° MCC data set. Thus, the aspect ratio values of closed MCC clouds in JJA are most likely biased to too high aspect ratios. Interestingly, the aspect ratios of open MCC cells still show seasonal differences, while in closed MCC clouds, the seasonal mean aspect ratios are similar in contrast to their cell diameter (Tables 4 and 6). Thus, while the seasonal differences in cell diameter in closed MCC cells mainly depend on changes in CTH, this is not the case

Table 6 Same as Table 4, but for aspect ratios.

	Open	**Closed**	**Open**		**Closed**	
			MPC	SLC	MPC	SLC
Annual	22.93	22.44	22.64	26.11	22.26	23.49
JJA	21.76	23.55	21.55	26.26	23.16	26.55
SON	23.10	22.13	22.76	26.12	21.81	24.63
DJF	25.60	22.41	25.26	27.11	22.37	22.60
MAM	22.74	22.80	22.58	25.04	22.84	22.63

Table 7 Same as Table 5, but for aspect ratios.

		Open	**Closed**	**MPC**	**SLC**
	Open vs Closed	MPC vs SLC	MPC vs SLC	Open vs Closed	Open vs Closed
Annual	1.0	1.0	1.0	0.625	1.0
JJA	1.0	1.0	0.75	1.0	0.0
SON	1.0	1.0	1.0	1.0	0.125
DJF	1.0	0.375	0.125	1.0	1.0
MAM	0.125	0.875	0.0	0.375	0.5

in open MCC cells.

The differences between mean aspect ratios of MPCs and SLCs in open and closed MCC clouds are examined to evaluate how this is influenced by cloud phase. The aspect ratios in SLCs are statistically significantly higher than in MPCs in both open and closed MCC cells in the annual mean. In general, I observe higher aspect ratios in SLCs than MPCs in all seasons in both regimes. However, not all are significant. The only exception is in closed MCC clouds in MAM with insignificantly higher values in MPCs than SLCs. As SLCs exhibit a significantly larger mean aspect ratio than MPCs, but not a larger mean cell diameter, this means that most larger open and closed MPCs cells occur at higher CTHs than SLCs (Fig. 24 and Section 3.2, Fig. 21).

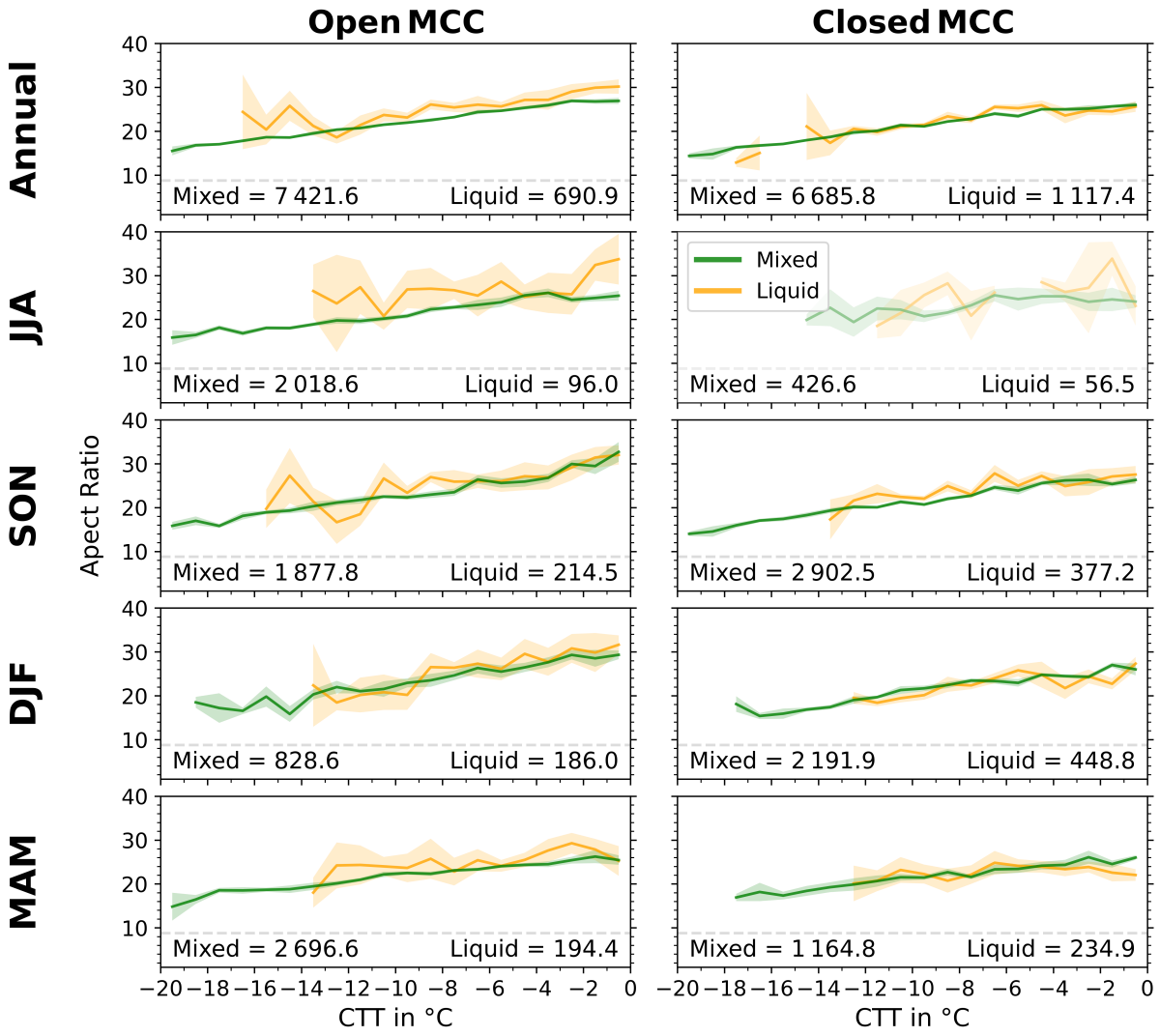

Fig. 25 Mean aspect ratio as a function of CTT for SLCs and MPCs with CTT from −20 °C to 0 °C. Numbers below the lines indicate the mean number of identified cells for MPCs and SLCs. As only 6% of the annual closed MCC clouds occur in JJA, the panel is displayed in more transparent color shading.

To further investigate what influences the aspect ratio differences between MPCs and SLCs, the dependence of the aspect ratio on CTT is analyzed in Fig. 25. In both open and closed MCC clouds, I observe a linear increase of aspect ratios with CTT independent of cloud phase. However, the CTT also depends on the CTH. This linear increase with CTT explains the larger mean aspect ratios in SLCs compared to MPCs, as the fraction of SLCs decreases drastically with lower CTT (Fig. 25 and Section 3.2, Fig. 19). Thus, MCC cells have smaller aspect ratios in deeper MBLs with lower CTT. Moreover, due to the aspect ratio dependence on CTT, the more considerable seasonal differences in open MCC aspect ratios are most likely linked to the strong seasonal changes in the mixed fraction discussed in Section 3.2 which are not as strong in closed MCC clouds. Especially, the substantially lower number of open MPCs below CTT $<-16\,^{\circ}\mathrm{C}$ in DJF compared to JJA (Fig. 19) corresponds to the season with the largest aspect ratios in open MCC clouds (Table 6).

A brief examination of the impact of other environmental meteorological conditions (not shown), e.g., estimated inversion strength (EIS), relative humidity of the free troposphere, or MCAO strength with Modern-Era Retrospective analysis for Research and Applications version 2 (MERRA-2), did not reveal any dependence on the aspect ratio. This is supported by the findings of *Zhou et al.* (2021), which show that the cell size does not depend on environmental conditions, like SST, EIS, or wind speed. Thus, while these environmental meteorological conditions are important to distinguish between the formation of open and closed MCC shown by several studies (e.g., *Wood and Hartmann*, 2006; *Muhlbauer et al.*, 2014; *McCoy et al.*, 2017; *Eastman et al.*, 2021), the impact on cell size is neglectable.

In conclusion, the cell size of single open and closed MCC cells depends on a combination of CTH and CTT in a supercooled environment with CTTs between $-20\,^{\circ}\mathrm{C}$ to $0\,^{\circ}\mathrm{C}$ in the SO. As both the mixed fraction (Section 3.2) and the aspect ratio depend on the CTT and due to the seasonal varying mixed fractions, the aspect ratios are differently affected in summer and winter. *Eirund et al.* (2019a) show that cell size increases as a function of formation time in open cells until it dissolves. Thus, the question remains whether cloud phase and, therefore, ice formation extends the lifetime of open and closed MPCs, leading to higher CTHs and lower CTTs, or whether this is caused by a faster evolution in MPCs due to stronger updrafts. Further investigations are also needed to answer whether SLCs are limited to certain CTHs due to phase changes or other dynamical effects. These questions could be examined with a Lagrangian approach of the segmentation method in geostationary satellite data similar to *Eastman et al.* (2021, 2022).

4.2 Dependence of In-Cloud Albedo on Aspect Ratio

This section focuses on how the in-cloud albedo is linked to the aspect ratios and cell size. While other studies investigate changes in albedo due to cloud morphology (*McCoy et al.*, 2017; *Abadi et al.*, 2016; *McCoy et al.*, 2023), differences in in-cloud albedo due to cell size have not been analyzed in previous studies. Similar to the results of Section 4.2, I find that closed MCC clouds have a higher in-cloud albedo than open MCC cells for both MPCs and SLCs independent of their aspect ratios. In closed MCC clouds, the in-cloud

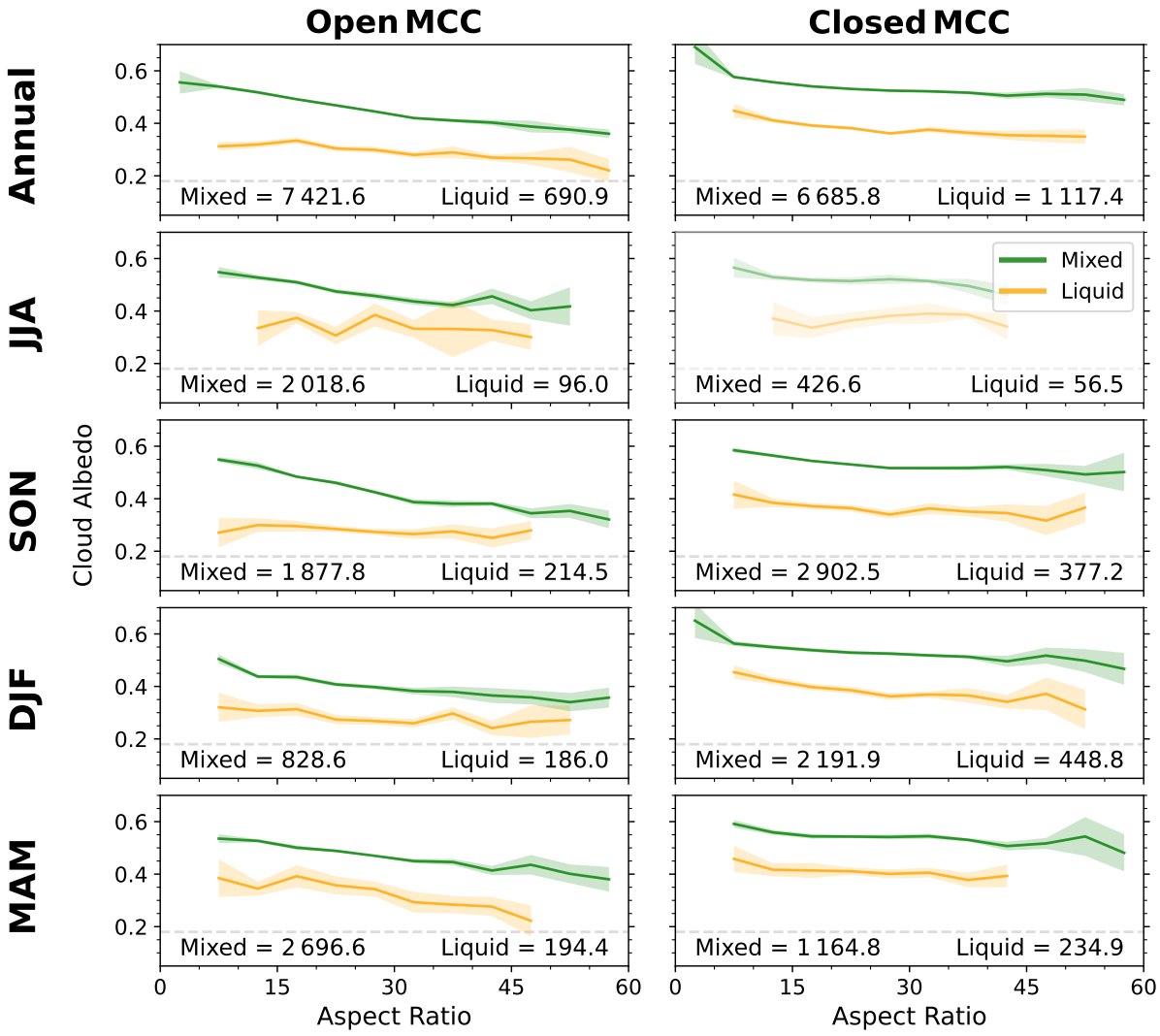

FIG. 26 Mean in-cloud albedo as a function of aspect ratio for SLCs and MPCs with CTT from −20 °C to 0 °C. Numbers below the lines indicate the mean number of identified cells for MPCs and SLCs. As only 6% of the annual closed MCC clouds occur in JJA, the panel is displayed in more transparent color shading.

albedo decreases slightly with the aspect ratio in both MPCs and SLCs (<0.1) and shows only marginal seasonal changes. This is in contrast to open MCC clouds, which exhibit a more drastic reduction of in-cloud albedo in MPCs of about 0.2 with an increase of the aspect ratio from 5 to 55 in the annual mean and austral spring (SON), while SLCs are only slightly decreasing (<0.1). A similar strong decrease of in-cloud albedo is only seen in open SLCs in austral fall (MAM). This difference between open and closed MCC clouds might be caused by less liquid remaining to be detrained at cloud top in open cells. As the in-cloud albedo is based on COT (Section 2.1), open MPCs with a higher aspect ratio are optically thinner with a lower LWP than open MPCs with a lower aspect ratio. A brief investigation of examples scenes (Fig. S11) shows that this is likely caused by optically thinner cloudy cell walls in larger open MPCs as there are close to dissolving at the end of their lifetime.

Improving the understanding of changes in cell size in MCC clouds in a changing climate is important, as low-level clouds, especially in the SO, remain the main uncertainty in climate models (*Bony and Dufresne*, 2005; *Bony et al.*, 2006, 2015). Section 4.1 shows that cell size changes are related to CTH and CTT. An increase in the height of the MBL in a warming climate, as shown by recent trends (*Díaz et al.*, 2019), would lead to changes in the aspect ratio and could, therefore, influence the cell size. However, it is unclear how it exactly affects the cell size as changes in CTT or cloud phase are also likely during climate change. Nonetheless, the changes in albedo due to changes in aspect ratio are up to 0.2, and at low aspect ratios, albedo changes associated with cloud phase are even higher (0.25). Assuming a typical solar insolation of $300\,\mathrm{W\,m^{-2}}$ in the SO, these changes in albedo relate to a cloud-radiative effect from $60\text{ - }75\,\mathrm{W\,m^{-2}}$. This emphasizes the importance of correctly predicting the cloud phase and cell sizes of MCC clouds in climate predictions.

5 Global MCC Climatology with CNN

To classify MCC clouds globally with the newly developed CNN model described in Section 2.4.3, I first evaluate the CNN model in detail. In Section 5.1, I investigate the CNN performance on the remaining test data set and discuss possible improvements for a future version. The second part of this chapter analyzes the global MCC climatology classified by the CNN. Moreover, annual and seasonal distributions of open and closed MCC occurrences are inspected and checked for consistency with the current understanding of MCC organization.

5.1 CNN Model Evaluation

To evaluate the CNN model, 495 scenes from the test data set are classified. These test data scenes have never been presented to it before. The confusion matrices summarize the results from this classification of the test data set in Fig. 27, and example test scenes of correctly predicted scenes are shown in Fig. 28. A confusion matrix shows the percentage

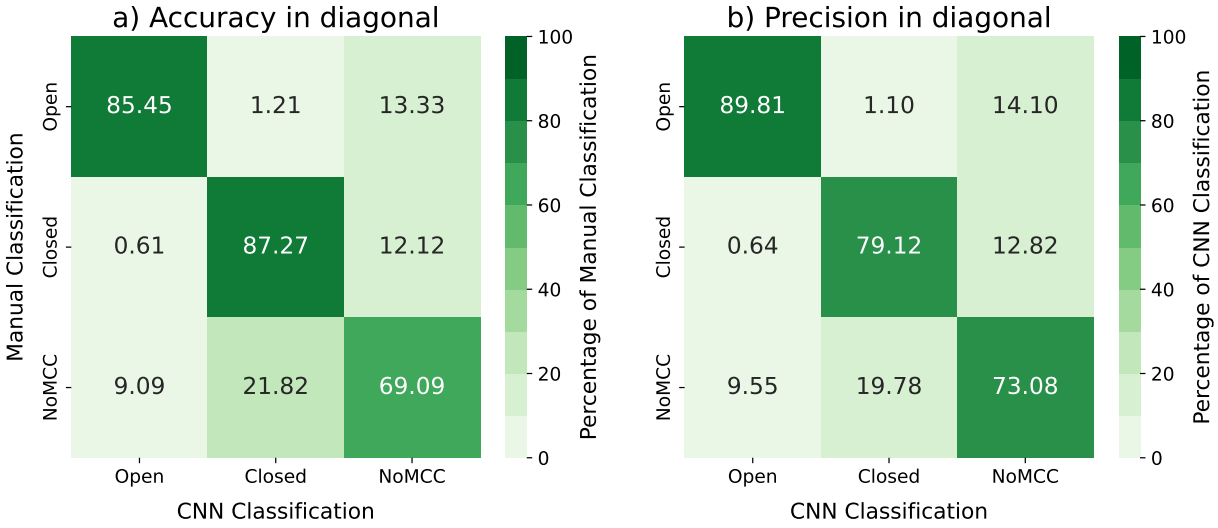

FIG. 27 Confusion matrices of the manual test data set and CNN predicted categories (a) normalized by the manual classification and (b) normalized by the CNN classification. Input data taken from *Reichel* (2022).

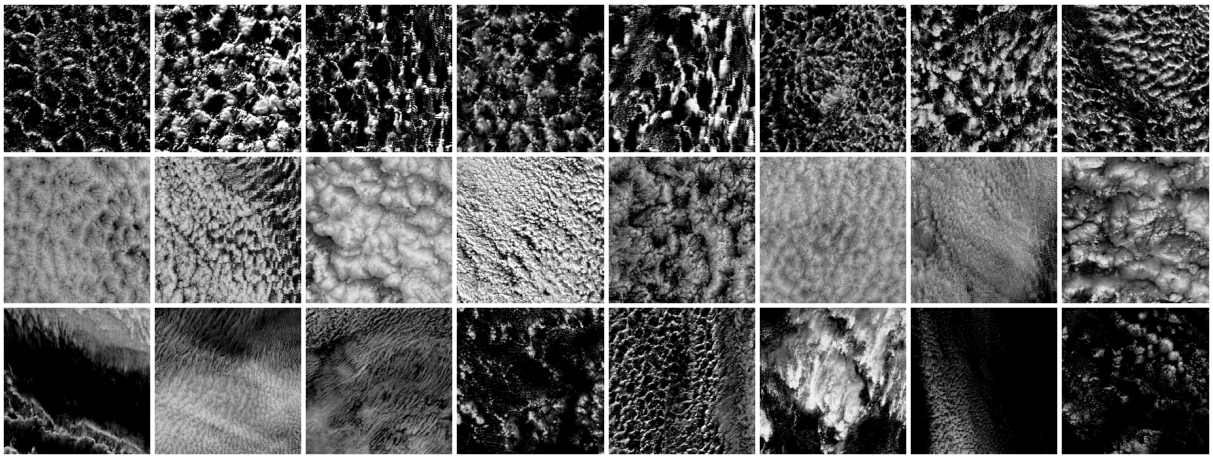

FIG. 28 Example scenes of the three categories from the test data set correctly predicted by the CNN classification. (1. row) Open test scenes, (2. row) Closed test scenes, and (3. row) NoMCC test scenes.

of correctly predicted categories in the diagonal while all incorrectly predicted classes are off the diagonal. The overall test accuracy of the CNN is 80.61%. At the same time, the test accuracies for Open and Closed are even higher with 85.45% and 87.27%, respectively. The accuracy of NoMCC scenes is lower with 69.09%. Typically, accuracy or precision values below 60% are considered poor, from 60 - 70% as fair, between 70 - 90% as good, and above 90% as very good. Thus, the overall CNN accuracy as well as the accuracies for Open and Closed are good, except for the NoMCC category which is fair. However, the NoMCC category is designed as a category for all scenes which are not Open or Closed scenes, or open and closed cell coverage with less than 70%. Thus, the NoMCC category is not as a distinct physical category which is expected to have lower accuracy, and scenes of this category are not further analyzed.

As this CNN is designed to precisely predict Open and Closed scenes, chances of misclassification between Open and Closed categories should be minimal. As shown in Fig. 27, the percentage of misclassification from Open to Closed is only 1.21%, and the percentage of the reverse case is even lower with 0.61%. As described in Section 2.4.2, we, the classifiers, also categorize scenes with open and closed MCC structure with less than 70% coverage as NoMCC (see Fig. 28, 3. row, 5. column). About 9% and 22% of NoMCC test scenes are misclassified as Open and Closed, respectively. In Fig. 29, the first two rows show these scenes that in the test data set are classified as NoMCC but are "misclassified" by the CNN as Open and Closed. However, most of these test NoMCC scenes show at least partial structures of the organization of open and closed MCC cells. Therefore, the precision of both Open (89.81%) and Closed (79.12%) would improve by using a test data set in which the NoMCC category has no scenes with partial MCC organizations. The last two rows from Fig. 29 display the manually classified Open and Closed scenes,

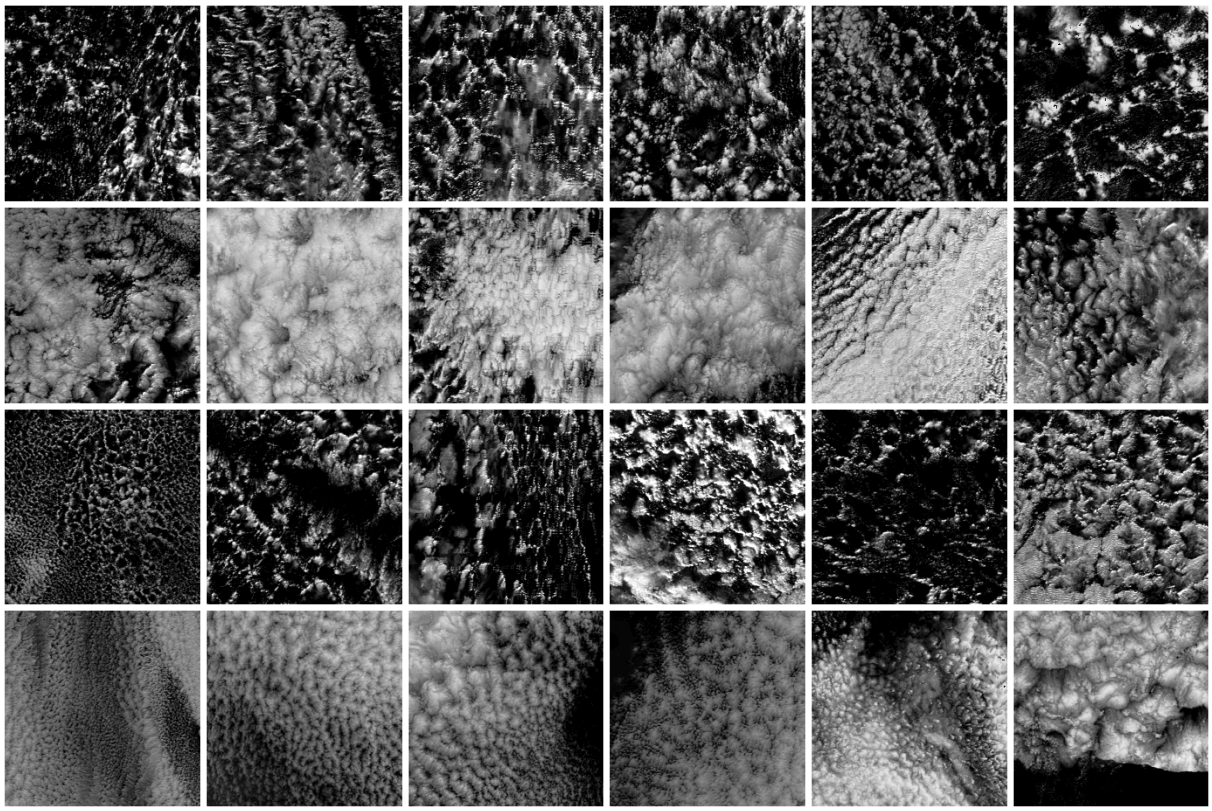

FIG. 29 Example scenes of four different misclassification groups between manual and CNN classification. (1. row) NoMCC test scenes classified as Open. (2. row) NoMCC test scenes classified as Closed. (3. row) Open test scenes classified as NoMCC. (4. row) Closed test scenes classified as NoMCC. Figure inspired by *Reichel* (2022).

which are classified as NoMCC by the CNN. About 13% of both categories are misclassified as NoMCC. Most Open scenes misclassified as NoMCC display tiny cells, substantial variance in brightness, or thick cell walls. In most of the Closed scenes misclassified as NoMCC, the closed MCC organization varies in cell size within a scene, decreasing and fading into a clear area.

In conclusion, the CNN archives a good precision for both Open and Closed. Though the precision of Open is higher than of Closed, this is probably caused by randomly having more NoMCC scenes with some coverage of closed cells than open cells in the test data set. To improve accuracy and precision in a future version of the CNN, the randomly taken 550 NoMCC scenes need to be reevaluated. Any scenes with partial coverage of open and closed MCC organization in the NoMCC category should be removed from all training, validation, and test data sets and replaced by other scenes of the remaining NoMCC group. While the threshold in the Open and Closed category of at least 70% coverage is important to define the MCC scene, any open or closed MCC scenes with less than 70% coverage should be removed from the NoMCC category in a future CNN version. As visible in

some scenes in Fig. 29 (e.g., open: 1. row, 1. column compared to 3. row, 3. column; closed: 2. row, 2. column compared to 4. row, 6. column), scenes in different test categories are very similar but are supposed to be categorized differently by the CNN. Further, in a future version, the categories should have identical distributions in the training and validation data set to avoid biasing the model to one category. However, as the difference between the categories is small and the sums of each category from the training and validation data set, which both adjust the model parameters, are equal, the model bias to one category is most likely weak. Overall, I show that the model is reasonably accurate at predicting scenes with open and closed MCC structure.

5.2 Global MCC Climatology

To understand the different types of MCC organization, it is important to know the frequency and location of the MCC regimes. The global MCC frequency of occurrence in 2008 is investigated annually and seasonally for open and closed MCC organizations to evaluate the CNN model (Section 2.4). All low-level cloud scenes between 65° S to 65° N are binned into a 5° x 5° grid by their central latitude and longitude. The fraction of occurrences of open or closed MCC scenes to the total number of all evaluated scenes defines the MCC frequency of occurrence in each grid box.

In general, the low latitudes are known for their persistent decks of stratocumuli (e.g., *Atkinson and Wu Zhang*, 1996; *Klein and Hartmann*, 1993; *Wood*, 2012) which are driven by large-scale subsidence and increased stability. In Fig. 30, the stratocumulus-dominated regions are indicated by white outlined boxes. While marine stratocumulus in mid-to-high latitudes span around the globe, in the subtropics they are confined to the eastern parts of the ocean basin roughly 5° off the coast. The displacement off the coast by around 5° is connected to the depth of the MBL which deepens with distance to the coast (*Wood and Bretherton*, 2004; *Wood*, 2012), especially visible in open MCC clouds. As seen in Fig. 30, the stratocumulus regions agree well with the annual occurrence frequency of open and closed MCC cells.

In the annual global mean, closed MCC clouds occur more frequently than open MCC clouds. Overall, closed MCC occurrence increases from ±30° N with increasing latitude (Fig. 30). The highest occurrence frequency of closed MCC clouds is found at high latitudes close to 65° S. Previous studies show that the mid-to-high latitudes are associated with a high frequency of closed MCC clouds (*Muhlbauer et al.*, 2014; *McCoy et al.*, 2017; *Mohrmann et al.*, 2021; *Lang et al.*, 2022, 2023). Additionally, there are three regions west of the continents in the tropics and subtropics (Northeast Pacific, Southeast Pacific, and Southeast Atlantic) with frequent occurrence of closed MCC clouds. This matches the

occurrences of closed MCC clouds shown by other studies (*Klein and Hartmann*, 1993; *Wood and Hartmann*, 2006; *Muhlbauer et al.*, 2014; *Mohrmann et al.*, 2021).

The global distribution of open MCC occurrence is mostly confined to the mid-latitudes between ±30° N and ±60° N (Fig. 30). The highest frequencies of open cells are located in the center of this band which is associated with the storm tracks between ±40° N and

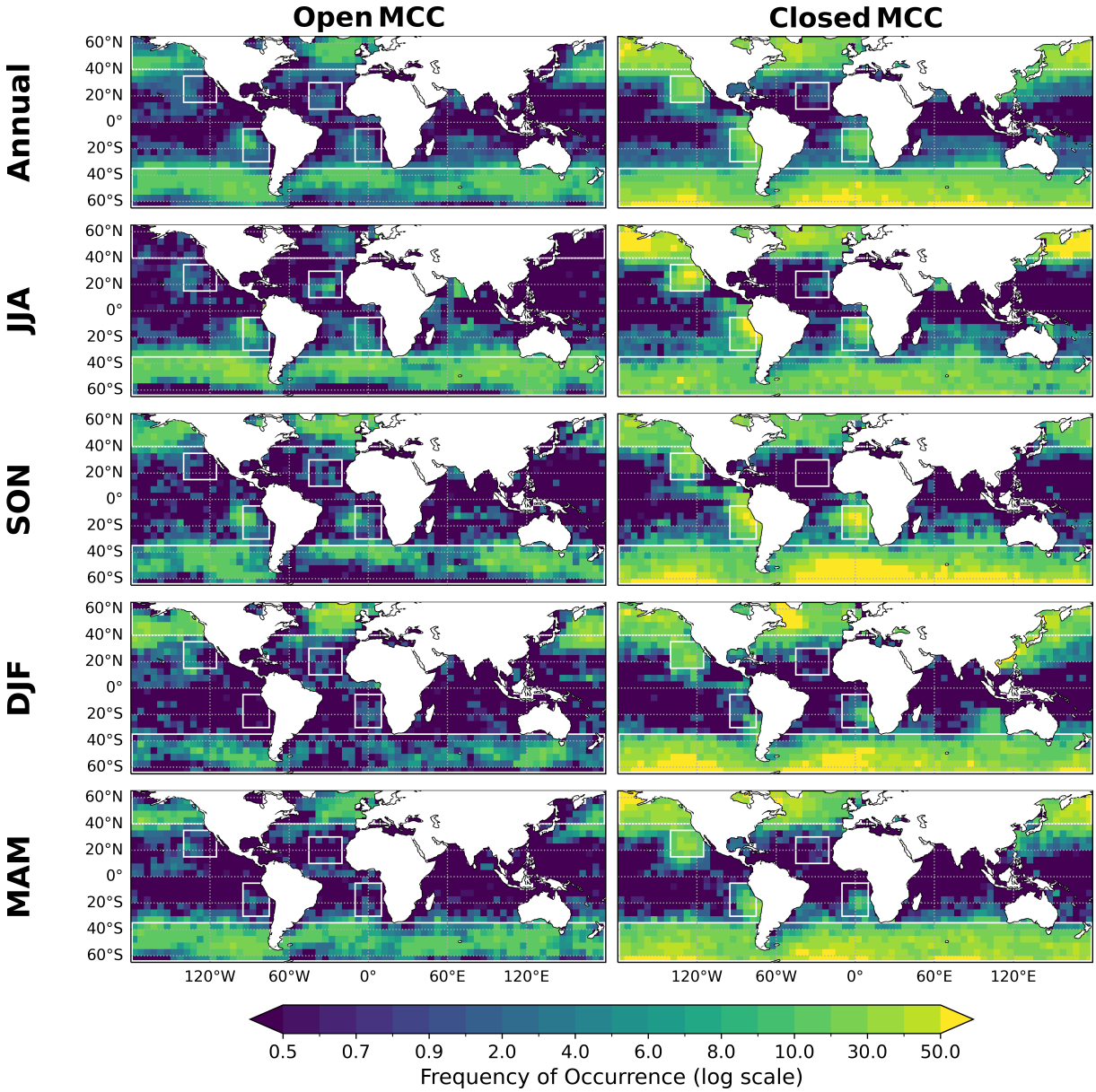

FIG. 30 Annual and seasonal global distribution of open and closed MCC frequency of occurrence based on the MODIS Aqua 0.86 µm reflectance band from 2008. Within 65° S to 65° N, all low-level cloud scenes with a mean CTH ≤3.5 km are binned into 5° x 5° bins. The frequency of occurrence is the percentage of occurrences of open or closed MCC scenes to the total number of all low-level cloud scenes. White outlined boxes indicate regions dominated by stratocumulus based on *Klein and Hartmann* (1993).

±50° N and MCAOs. *McCoy et al.* (2017) investigate the link between MCAOs with the occurrence of open and closed MCC clouds. They find a strong correlation between the MCAO index and open MCC clouds and, therefore, show that open MCC clouds favor lower static stability and stronger surface forcing. Further, open MCC clouds also display secondary peaks of occurrence in the eastern parts of oceans in the subtropics. However, these regions of open cells are shifted away from the continents and are west of the subtropical regions of closed cells. This regional pattern is also observed in previous studies (*Wood and Hartmann*, 2006; *Muhlbauer et al.*, 2014; *McCoy et al.*, 2017; *Mohrmann et al.*,

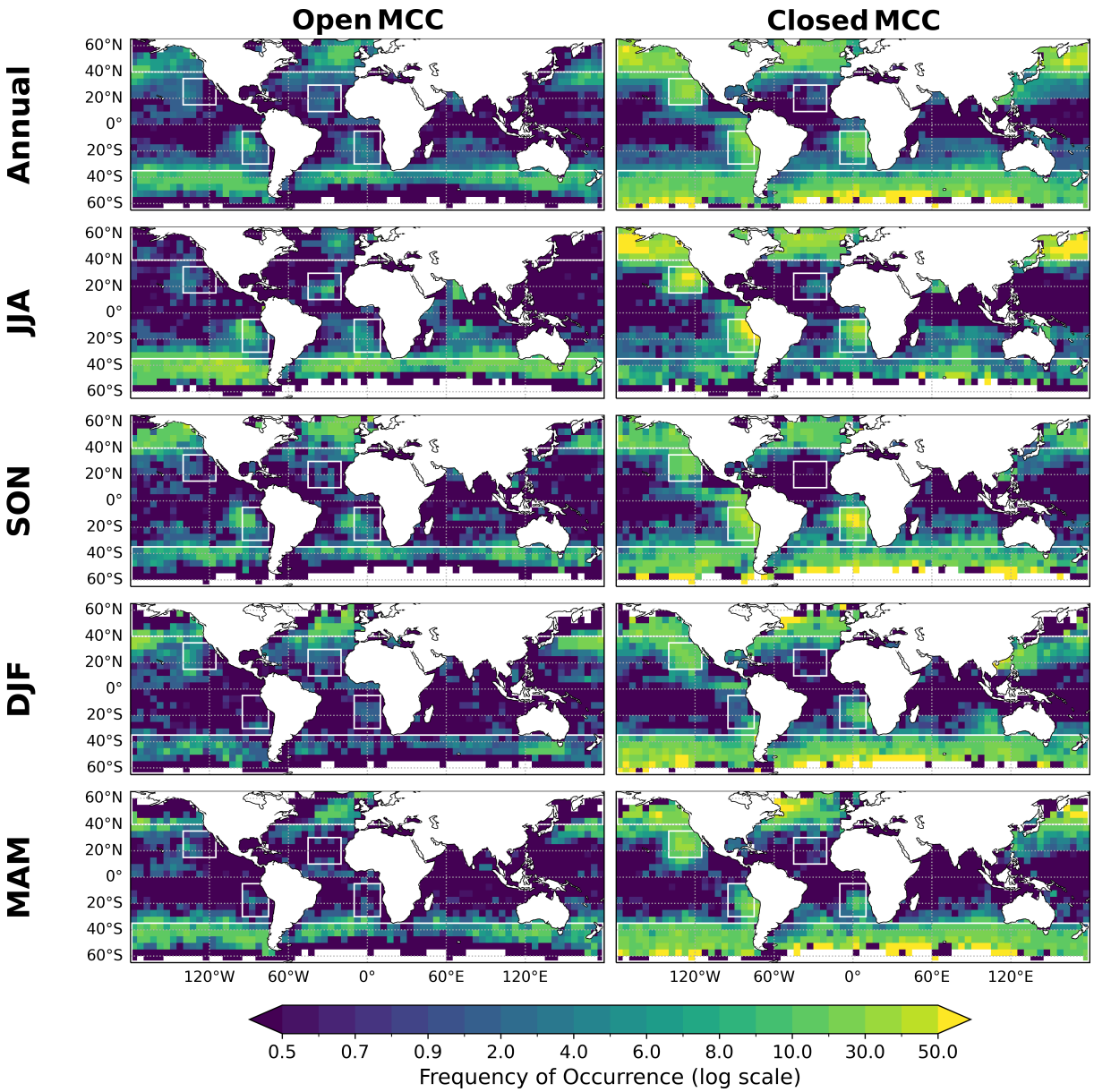

FIG. 31 Same as Fig. 30, but only cloud scenes with a mean CTT above 0 °C are passed to the CNN. White boxes over the ocean indicate that no scenes are passed to the CNN.

2021) and associated with a transition from closed to open MCC clouds (*Eastman et al.*, 2022).

In the NH, the closed MCC occurrence frequency peaks in boreal summer (JJA), especially at high latitudes in the North Pacific. While in the SH, the highest frequency of closed MCC occurs in austral spring (SON). However, austral summer (DJF) only shows a slightly weaker occurrence frequency. This matches the seasonal peaks of closed MCC occurrence by *Muhlbauer et al.* (2014). Further, it is also similar to *McCoy et al.* (2017) and *Lang et al.* (2022, 2023), which also exhibit the highest occurrence frequency of closed MCC clouds in summer in the SH. Interestingly, I observe a region of a high frequency (above 50%) of closed MCC cells during boreal winter (DJF) over the Labrador Sea, which is not apparent in other climatologies (*Muhlbauer et al.*, 2014). This area is known for MCAOs during winter, in which clouds develop from roll-like stratocumulus cloud streets near the coast to sometimes closed MCC cells and then typically to open MCC cells (*Raasch and Schröter*, 2001). Further, I verified the frequently observed closed MCC clouds from the CNN by visually inspecting this area using satellite images from January 2008. Closed MCC cells occur 14 out of 31 days over the Labrador Sea during this January. These closed cells often develop from cloud streets, which should also be identified as closed MCC clouds by *Muhlbauer et al.* (2014) (*Wood and Hartmann*, 2006; *McCoy et al.*, 2017). Thus, a possible explanation could be that these closed MCC clouds are MPCs which could be missed in their MCC classification, which is based on LWP and restricted to scenes with warm clouds (CTT>273 K) in *Muhlbauer et al.* (2014). To further investigate this, Fig. 31 shows the same global climatology of open and closed MCC clouds as Fig. 30 but only scenes with a mean CTT>273 K are passed to the CNN. Figure 31 reveals that especially over the Labrador Sea there are almost no warm cloud scenes explaining the lower occurrence of closed MCC clouds in *Muhlbauer et al.* (2014). Further, Fig. 32 displays the MCC data set used in *McCoy et al.* (2017) for the year 2008 which is not restricted to warm cloud scenes but based on the LWP (see Section 2.3). In comparison to the results of the developed CNN (Fig. 30), the occurrence frequencies of closed cells are lower in both the North Atlantic and North Pacific in Fig. 32. This would support the hypothesis that MCC classification based on LWP miss MPCs with a low LWP which are detected by the CNN used here. Nevertheless, the overall seasonal distribution of closed MCC clouds coincides with previous studies (*Wood and Hartmann*, 2006; *Muhlbauer et al.*, 2014; *McCoy et al.*, 2017; *Mohrmann et al.*, 2021; *Lang et al.*, 2022, 2023).

Seasonally, the highest occurrence frequency of open MCC clouds is observed during winter in both hemispheres. In the SH, open MCC cells shift equatorward from austral summer (DJF) to winter (JJA). Both, the higher frequency and the equatorward shift in

winter are influenced by more frequent MCAOs, which shift equatorward during winter with the edge of sea ice (Section 3.1). The strong correlation of open cells and MCAOs is already established by *McCoy et al.* (2017). The seasonal open cell distribution findings generally agree with other works (*Muhlbauer et al.*, 2014; *McCoy et al.*, 2017). However, the overall occurrence frequency of open cells is lower in Fig. 30 than in Fig. 32 based on *McCoy et al.* (2017). This agrees with recent findings by *Yuan et al.* (2020) and *Mohrmann et al.* (2021) who also show much lower open occurrence frequency than *McCoy et al.* (2017). These differences in the occurrence frequency of open MCC cells

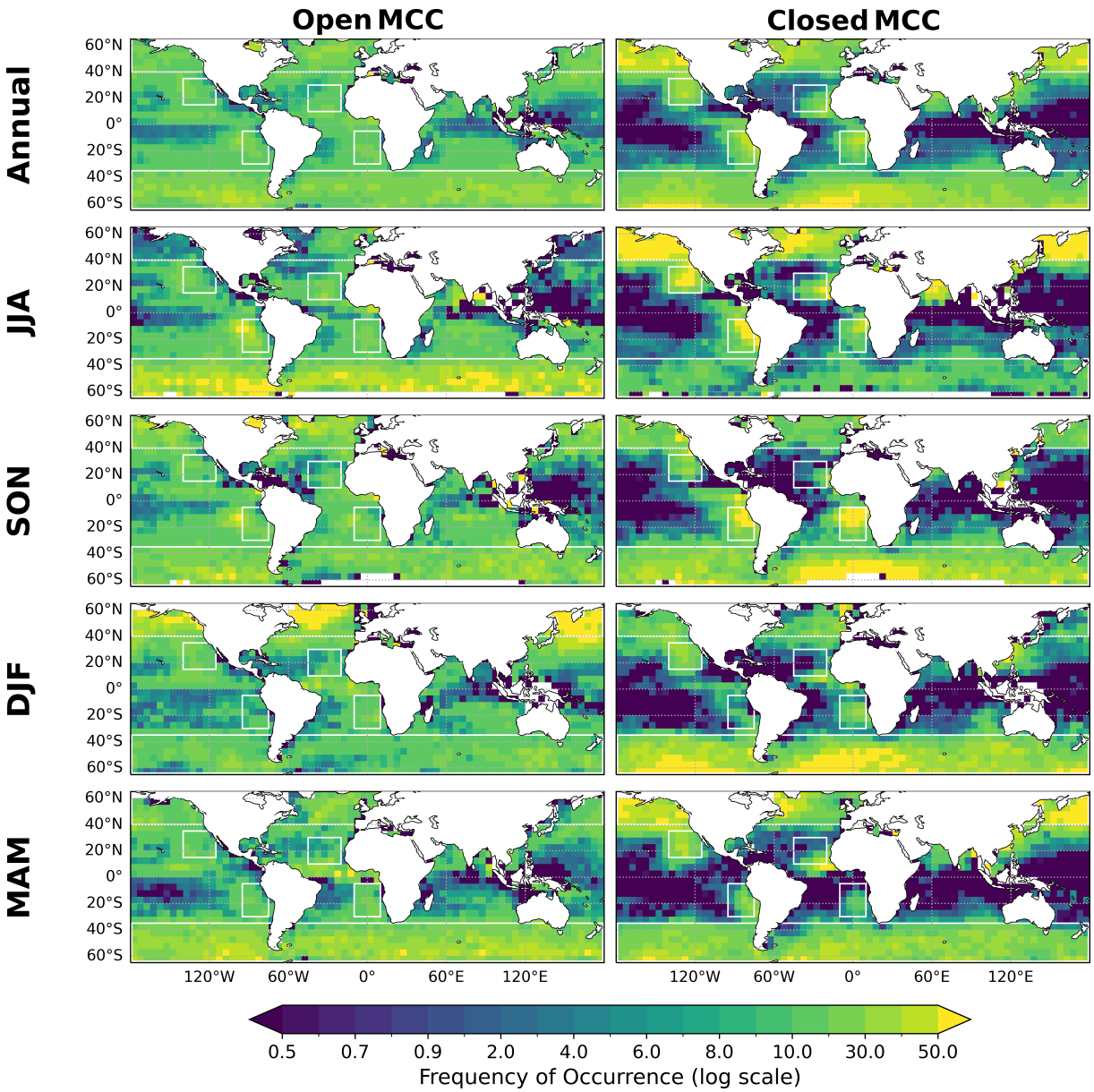

FIG. 32 Annual and seasonal global distribution of open and closed MCC frequency of occurrence based on the MCC data set from *McCoy et al.* (2017) for the year 2008.

in different classification methods reveal the difficulty of distinguishing open MCC cells from disorganized convection. To differentiate between open MCC clouds and disorganized convection is especially challenging, as the transition from open to disorganized regimes is very smooth. Thus, whether a scene is considered as open with large cells or already as disorganized is subjective. This influences the training data set which impacts the occurrence frequency of open MCC clouds in different classifications and explains the higher occurrence frequency of open MCC clouds in *Muhlbauer et al.* (2014) and *McCoy et al.* (2017) (as displayed in Fig. 32) in comparison with the developed CNN and other works (*Yuan et al.*, 2020; *Mohrmann et al.*, 2021). *Lang et al.* (2022, 2023) exhibit the maximum of open MCC clouds in austral spring (SON) in a part of the SO, south of Australia. In contrast to others, they find a higher occurrence of open than closed MCC clouds in this part of the SO in all seasons. Nevertheless, in their data, open MCC clouds occur almost as frequently in austral winter as in spring (*Lang et al.*, 2022, 2023). In the NH, the highest frequency occurrence in boreal winter (DJF) agrees well with *Muhlbauer et al.* (2014) except for a region in the North Atlantic, east of Greenland and the eastern part of the North Pacific. There, I find an occurrence frequency of open cells, which is lower in *Muhlbauer et al.* (2014). This might again be related to the setup of their MCC classification, which could miss MPCs with a low LWP and CTT below 273 K.

In summary, I show that the developed CNN model used to create the global MCC climatology is able to produce a realistic occurrence of open and closed MCC clouds. Further, I detected hints for missing MPCs in the NH, which should be better represented in the developed CNN based on the MODIS 0.86 µm reflectance band instead of the LWP (Sections 2.3 and 2.4.3).

6 Conclusions and Outlook

6.1 Summary

Marine stratocumuli cover vast areas of the SO and are globally the most dominant cloud type by area coverage. The main objective of this thesis is to explore cloud phase differences in their self-organized morphological regimes and evaluate connections between cloud phase, cloud morphology, cell size, and cloud albedo in the SO. While the influence of the cloud phase on the cloud morphology in the NH is analyzed by a small number of case studies with numerical models (*Abel et al.*, 2017; *Eirund et al.*, 2019a; *Tornow et al.*, 2021), so far, it has not been examined in the SH or with extensive spatial coverage. Thus, this thesis investigates the link between cloud phase and morphology with spaceborne lidar-radar retrievals focusing on the SO.

Using polar-orbiting satellite retrievals has the advantage of covering almost the entire globe. While passive satellites have higher coverage than active satellites, their cloud phase instruments can only classify the cloud phase at cloud top. Thus, to evaluate the cloud phase in this thesis, active satellite retrievals are used to avoid missing MPCs with a supercooled layer at cloud top. The evaluation of the newly developed vertically integrated cloud phase classification based on the DARDAR v2 shows that its results are similar to previous studies (e.g., *Huang et al.*, 2017; *Lang et al.*, 2021; *Zaremba et al.*, 2021).

6.1.1 Interplay Between Cloud Morphology, Phase, and Radiative Properties

The first part of this thesis investigates the relationships between cloud phase and morphology in the SO. At a given CTT, seasonal changes in the mixed-phase fraction are more significant than any morphological changes. These seasonal changes seem to depend on the nucleation rate of INPs. The dependence of cloud phase on CTH is more substantial than on CTT, particularly in clouds with CTHs below 2.5 km. This suggests that deeper and more decoupled MBLs have a tendency to generate ice in supercooled environments. Overall, these changes seem to be more impacted by external factors rather than morphology.

The hypothesis of preconditioning is formulated by *Abel et al.* (2017) and *Tornow et al.*

(2021) and states that the closed-to-open transition is favored in MPCs compared to SLCs in case studies. Thus, this could conclude in a preference of open MCC clouds to occur as MPCs. However, this cannot be confirmed by the mixed fraction of open and closed MCC clouds. As the LWP:IWP ratio is not investigated, the mixed fraction might include MPCs with low IWPs, which can influence the impact of ice formation on cloud morphology (*Eirund et al.*, 2019a). Thus, these results suggest that preconditioning seems not to impact closed-to-open transitions in the general climatology of marine stratocumulus.

The examination of the link between cloud morphology and in-cloud albedo reveals substantial in-cloud albedo differences between open and closed cells from 0.07 to 0.13, depending on cloud phase and season. This is consistent with the results from *McCoy et al.* (2017), which show higher albedo in closed MCC clouds than in open clouds, even for the same cloud fraction. These seasonal and cloud-phase-dependent differences in in-cloud albedo can drive changes in the cloud radiative effect of $21\,\mathrm{W\,m^{-2}}$ to $39\,\mathrm{W\,m^{-2}}$ in the SO. Moreover, the cloud phase differences within the MCC organizations reveal that in-cloud albedo differences are more pronounced in SLCs than MPCs in both MCC regimes.

6.1.2 Examining Effects of MCC Cells Spatial Scales

To examine how the cell sizes of MCC cells are influenced by cloud phase, I establish an automatic image segmentation method based on $200\times200\,\mathrm{km^2}$ MODIS 0.86 µm reflectance scenes (*Platnick et al.*, 2015). The equivalent mean cell diameter in open and closed MCC clouds is similar in MPCs and SLCs in the annual mean. However, the seasonal cell diameter differences between MPCs and SLCs are significant. While in austral summer, the mean cell diameter of MPCs is larger than of SLCs, in austral winter, MPCs are smaller than SLCs in both MCC organizations. The seasonal changes in cell size in MPCs are larger in both MCC regimes than in SLCs, highlighting the importance of seasonal differences in the two MCC regimes. Even though the automatic segmentation method is carefully tested and designed to avoid biasing the cell diameters, remaining small biases cannot be excluded.

To account for varying CTHs in cloud cells, the aspect ratios are analyzed to gain further insights into the dependence of cell size on cloud morphology and phase. Closed MCC clouds exhibit smaller aspect ratios than open MCC cells in the annual mean. Thus, closed MCC cells are smaller than open cells independent of CTH. I find that the seasonal differences observed in cell diameter are not apparent in the aspect ratio of closed MCC clouds, while they are apparent in open MCC clouds. Therefore, changes in CTH mainly explain the seasonal differences in cell diameter in closed MCC cells, whereas, in open

MCC cells, the seasonal variations are independent of CTH.

The in-cloud albedo decreases in both open and closed MCC clouds with increasing aspect ratios. The most substantial decrease is found in open MPCs. Further, differences in the in-cloud albedo due to cloud phase changes are typically around 0.2 and up to 0.25 at low aspect ratios. Cloud albedo changes of 0.2 - 0.25 relate to cloud-radiative effects from 60 - 75 $\mathrm{W\,m^{-2}}$, emphasizing the correct prediction of MCC cloud cell size and cloud phase in climate models.

6.1.3 Global MCC Climatology with CNN

Detecting MCC organization independent of cloud phase is essential to investigate MPCs with low LWPs or ice-phase clouds. Thus, a CNN is established based on $224\times224\,\mathrm{km^2}$ MODIS scenes from the 0.86 µm reflectance band as part of the master thesis from *Reichel* (2022). The overall test performance of the CNN shows a accuracy of 80.6%, with even higher accuracies in Open (85.5%) and Closed (87.3%) categories. The misclassifications between Open and Closed categories are very low, with less than 1.2%. The evaluation of the CNN shows that the scene classification of both Open and Closed can be trusted.

To enhance our understanding of different MCC organizations, the annual and seasonal global MCC occurrence frequencies in 2008 are classified with the CNN. In general, closed MCC clouds increase with latitude from ±30° N towards high latitudes, while open MCC clouds mainly occur within the storm tracks, peaking roughly at ±45° N. Overall, the global MCC climatology is in accordance with other MCC distributions (*Wood and Hartmann*, 2006; *Muhlbauer et al.*, 2014; *McCoy et al.*, 2017; *Mohrmann et al.*, 2021; *Lang et al.*, 2022, 2023). The most notable difference in frequency occurs in the NH in boreal winter. Compared to studies based on the LWP (*Muhlbauer et al.*, 2014; *McCoy et al.*, 2017), I exhibit an increase in closed and open MCC clouds in the NH. This increase of MCC in the NH during winter might be caused by missing MCC MPCs as the study from *Muhlbauer et al.* (2014) is restricted to warm cloud scenes (CTT >273 K) and MPCs with a low LWP might not be detected (*Muhlbauer et al.*, 2014; *McCoy et al.*, 2017).

6.2 Conclusions

Overall, changes in cloud phase, morphology, or cell size can have significant implications in a warming climate by altering the cloud-radiative properties. Especially in the SO, low-level clouds remain the key uncertainty in global climate models (*Bony and Dufresne*, 2005; *Bony et al.*, 2006, 2015; *Zelinka et al.*, 2020; *Schuddeboom and McDonald*, 2021). In general, global climate models predict a decrease in cloud cover leading to a positive

feedback which amplifies the warming through a reduced albedo (*Clement et al.*, 2009; *Qu et al.*, 2015; *Myers and Norris*, 2016; *Norris et al.*, 2016; *Myers et al.*, 2021; *Zelinka et al.*, 2020). The possible cloud morphology feedback is hypothesized by *McCoy et al.* (2017). They argue that a weakening in MCAO strength, found by *Kolstad and Bracegirdle* (2008), in the NH could lead to less open and more closed MCC cells if the results from *Kolstad and Bracegirdle* (2008) can be assumed globally. This correlation between MCAOs and cloud morphology (Fig. S7) and the differences of in-cloud albedo (Table 3 and Fig. 26) between open and closed MCC cells may partially offset the cloud feedback and lead to an overall reduced decline of low-level clouds.

In addition to changes in cloud morphology in a warming climate, a shift of cloud phase to more warm liquid clouds and less MPCs and SLCs is expected in mid-to-high latitudes. Previous studies defined the cloud phase feedback as a negative feedback which results in optically thicker clouds with a higher albedo (*Storelvmo et al.*, 2015; *Gettelman and Sherwood*, 2016). However, recent studies (*Murray et al.*, 2021; *Wall et al.*, 2022) show that the cloud phase feedback only marginally contributes to the overall cloud feedback as it depends on the optical thickness of MPCs which are often already optically thick. Nevertheless, the phase shift can lead to a longer lifetime due to a lower precipitation efficiency in liquid clouds (*Tan and Storelvmo*, 2019; *Mülmenstädt et al.*, 2021). While this thesis did not find any evidence that open cells occur more often within MPCs than closed cells, precipitation is one of the key drivers of the closed-to-open transition (*Yamaguchi and Feingold*, 2015; *Abel et al.*, 2017; *Eastman et al.*, 2021, 2022). Thus, the ice-to-liquid conversion could lead to less precipitation in warm MCC clouds and to fewer transitions from closed to open MCC clouds in warm clouds. Therefore, this could potentially lead to even more closed MCC clouds compared to open cells and in turn to a higher albedo than by the cloud morphology feedback alone. In conclusion, these two feedbacks might lead to an overall positive feedback. However, this is a very complex system with many other environmental factors changing with climate change, e.g., an increase in INPs (*Murray et al.*, 2021; *Twohy et al.*, 2021), in MBL height (*Díaz et al.*, 2019) or in cloud lifetime (*Tan and Storelvmo*, 2019), which are not discussed here. Overall, this shows the importance of enhancing cloud prediction in global climate models.

In summary, this thesis shows that seasonal changes in drivers of cloud formation impact SO stratocumulus cloud phase more strongly than differences in cloud morphology and thus cloud-driven dynamics. Both cloud phase and morphology seem to be mostly controlled by other environmental factors. Cloud-phase changes can alter the in-cloud albedo by up to 0.25 at low aspect ratios relating to a cloud-radiative effect of $75\,\mathrm{W\,m^{-2}}$ in the SO. This thesis emphasizes understanding the dependencies of cloud phase, morphology, and cell size to enhance predictions of the cloud-radiative effect.

6.3 Outlook

The findings of this thesis highlight the importance of improving our understanding of cloud phase, organizational transitions, and cell size to enhance predictions of changes in the cloud-radiative effect in the open and closed MCC cells. This section describes the remaining open questions and suggests future research avenues:

- **Investigating large-scale subsidence**
  As stated in Section 3.2, due to limitations in satellite retrievals, it was not possible to evaluate the influence of cloud-top-generated and boundary-layer turbulence on CTHs in SO stratocumuli. To further investigate the hypothesis that the MCC occurrence and accelerated updraft speeds are linked to ice formation, I suggest examining the large-scale subsidence which influences the turbulent cloud-top entrainment induced by cloud-top radiative cooling (*Mellado*, 2017). The effects of increased large-scale subsidence in Arctic mixed-phase stratocumuli yield a strengthening of the MBL, a reduction of cloud-top entrainment, and an increase of LWP and IWP (*Young et al.*, 2018). Due to increased cloud-top cooling, the convective overturning circulation within the cloud is accelerated, which could lead to stronger updrafts in the cloud core. I propose to analyze the large-scale subsidence with a reanalysis data set from National Centers for Environmental Prediction (NCEP), which has a spatial resolution of 2° and temporal resolution of 6 h, in combination with spaceborne retrievals to identify large-scale trends.

- **Global statistics of cloud phase and cell size**
  To investigate whether the findings of cloud phase and cell size are constrained to the SO or extend globally, I propose to extend the analysis to global coverage. In the SO, the open cells are larger than closed MCC cells independently of CTH. In contrast, *Wood and Hartmann* (2006) find that closed MCC cells are larger than open cells in the northern and southern parts of the subtropical East Pacific. Thus, investigating the cell size with the segmentation method in the subtropical regions might reveal contrasting results to the SO or differences between the cell size methods.
  As in general MPCs are mainly confined to higher latitudes, the seasonal differences in cloud phase depending on CTT should be inspected with a focus on high latitudes in the NH (45° N to 65° N). As the evaluation of the CNN in Section 5.2 indicates the possibility of missing MPCs, especially in the NH, with the MCC data set based on LWP, it should be considered to change the MCC classification to the established CNN in Section 2.4 or the 1°×1° MCC gridded product developed by *Yuan et al.* (2020).

- **Lagrangian segmentation approach**
  As mentioned in Section 4.1, it remains unanswered how cloud phase influences the cell size. This dependence could potentially extend the lifetime of open and closed MPCs, which might explain the higher CTHs and lower CTT. Otherwise, it could lead to a faster cloud evolution in MPCs due to stronger updrafts. To investigate the temporal evolution of clouds, polar-orbiting satellites are insufficient as they only detect a certain cloud once a day. Thus, a higher temporal resolution is needed, which is achieved by geostationary satellites e.g., Himawari-8, with a temporal resolution of 10 min. While the transition from closed to open cell regimes is explored with a Lagrangian approach in MODIS data by *Eastman et al.* (2021, 2022), I suggest a similar Lagrangian approach combined with the single cell segmentation in geostationary satellites to examine the lifetime of a single MCC cell.

- **Cell segmentation with different MCC data set**
  To reduce possible biases in the cell size in the cell identification method, I propose to address the selection of closed MCC scenes. As discussed in Section 2.5.2, some closed MCC scenes identified by the MCC data set from *Wood and Hartmann* (2006) display more stratiform clouds than cellular organization. This could lead to larger cell areas and bias the cell diameter. A simple test that would be computationally efficient is to run the CNN on all selected closed MCC scenes before segmentation. While this adjustment of the cell segmentation could be easily adapted, it would not solve missing MPCs with a low LWP. Thus, using a MCC classification method based on reflectance like the $1°\times1°$ MCC data set (*Yuan et al.*, 2020) or the established CNN could provide more insight into these MPCs. However, as the $1°\times1°$ MCC data set detects substantially fewer open MCC occurrences as discussed in Section 4.1, it might be better to use the CNN to identify MCC clouds in the cell segmentation focusing on differences in open and closed cells.

- **CNN model improvements**
  To improve the accuracy and precision of the CNN, the NoMCC category needs to be carefully reevaluated. As examined in Section 5.1, the randomly chosen 550 NoMCC scenes used to train, valid, and test the CNN include ambiguous scenes partly displaying MCC organization with less than 70% coverage. These ambiguous scenes should be removed from the randomly selected NoMCC scenes and replaced by unambiguous scenes from the remaining unused NoMCC scenes (17824 scenes). As discussed in Section 5.1, while the condition of at least 70% coverage of open and closed MCC scenes is important as a threshold, any open or closed MCC scenes with less than 70% coverage should be removed from the NoMCC category in a future

CNN version due to very similar scenes in different test categories. Thus, only the NoMCC category should be reevaluated. A manual reclassification of the NoMCC category, however, should be selected by at least three classifying individuals to be consistent with the rest of the manually classified data set.
Another issue that should be addressed is the unequal number of training and validation scenes due to the *validation_split* argument, which takes the last 30% without any regard for the category. To avoid an unequal amount of scenes, the split between training and validation should be prepared manually and randomly before passing it to the *model.fit* function from the *tensorflow* package in Python (*Pang et al.*, 2020). In addition, similar to *Yuan et al.* (2020), it might be advantageous to use a pre-trained deep CNN model, which is better at extracting features, as the base of the developed CNN.

Deutsche Zusammenfassung

6.4 Zusammenfassung

Marine Stratocumuli bedecken weite Teile des Ozeans und sind flächenmäßig die dominierende Wolkenart. Sie ordnen sich selbst in verschiedenen morphologischen Regimen an (*Wood and Hartmann*, 2006). Die beiden organisierten zellulären Regime werden als offene und geschlossene mesoskalig-zelluläre konvektive (MCC) Wolken bezeichnet. In mittleren bis hohen Breitengraden sind offene und geschlossene Zellen die beiden häufigsten Typen von MCC-Wolken (*Muhlbauer et al.*, 2014). Viele MCC-Wolken bestehen aus einer Mischung aus Dampf, flüssigen Tröpfchen und Eispartikeln, die als Mischphasenwolken (MPCs) bezeichnet werden. Selbst bei gleichem Wolkenbedeckungsgrad ist die Albedo offener Zellen im Durchschnitt niedriger als die von geschlossenen MCC-Wolken. Wolkenphase und -morphologie beeinflussen individuell den Strahlungseffekt von Wolken (*McCoy et al.*, 2017).

Das Hauptziel dieser Arbeit ist es, die Unterschiede zwischen den Wolkenphasen in ihren selbstorganisierten morphologischen Regimen zu erforschen und die Zusammenhänge zwischen Wolkenphase, Wolkenmorphologie, Zellgröße und Wolkenalbedo im Südlichen Ozean (SO) zu bewerten. Während der Einfluss der Wolkenphase auf die Wolkenmorphologie in der Nordhemisphäre (NH) durch eine kleine Anzahl von Fallstudien bereits mit numerischen Modellen analysiert wurde (*Abel et al.*, 2017; *Eirund et al.*, 2019a; *Tornow et al.*, 2021), wurde dieser bisher nicht in der Südhemisphäre (SH) oder mit umfassender räumlicher Abdeckung untersucht. Daher wird in dieser Arbeit der Zusammenhang zwischen Wolkenphase und -morphologie mit weltraumgestützten Lidar-Radar-Messungen im SO untersucht. Darüber hinaus werden die Auswirkungen der Wolkenphase auf die Größe der einzelnen Wolkenzellen in beiden Organisationsregimen untersucht. Obwohl frühere Studien die Unterschiede in der Zellgröße in offenen und geschlossenen MCC-Wolken analysiert haben, konzentrieren sich die meisten Studien auf den mittleren Zelldurchmesser ganzer Wolkenszenen (*Wood and Hartmann*, 2006; *Zhou et al.*, 2021) oder wie kleine Zellgrößen in gröberen Modellauflösungen dargestellt werden können (*Martini et al.*, 2014). Schließlich analysieren wir die globale MCC-Klimatologie auf der Grundlage des 0,86 µm-Reflektanzsbandes von MODIS, das im Gegensatz zu dem in den Kapiteln 3 und 4 verwendeten MCC-Datensatz (*Wood and Hartmann*, 2006), auch MPCs mit einem niedrigen Flüssigwasserpfad (LWP) detektiert.

Die Verwendung polarumlaufender Satelliten hat den Vorteil, dass sie fast den gesamten Erdboden abdecken. Passive Satelliten haben zwar eine größere Abdeckung als aktive Satelliten, ihre Wolkenphasenmessgeräte können jedoch nur die Wolkenphase an der Wolkenobergrenze (CTH) klassifizieren. Daher werden für die Auswertung der Wolkenphase in dieser Arbeit aktive Satellitenmessungen verwendet, um zu vermeiden, dass MPCs mit einer unterkühlten (bzw. supercooled) Schicht an der Wolkenobergrenze übersehen werden. Die Auswertung der neu entwickelten vertikal integrierten Wolkenphasenklassifikation auf der Grundlage von liDAR-raDAR (DARDAR) v2 zeigt, dass die Ergebnisse mit denen früherer Studien vergleichbar sind (e.g., *Huang et al.*, 2017; *Lang et al.*, 2021; *Zaremba et al.*, 2021).

6.4.1 Wechselwirkung zwischen Wolkenmorphologie, Wolkenphase und Strahlungseigenschaften der Wolken

Im ersten Teil dieser Arbeit werden die Beziehungen zwischen der Wolkenphase und der Morphologie im SO untersucht. Bei einer bestimmten Wolkenobergrenzentemperatur (CTT) sind die jahreszeitlichen Veränderungen des Mischphasenanteils signifikanter als alle morphologischen Veränderungen. Diese saisonalen Veränderungen scheinen von der Keimbildungsrate der eiskeimbildenden Partikel (INPs) abzuhängen. Die Abhängigkeit der Wolkenphase von der CTH ist deutlicher als von der CTT, insbesondere bei Wolken mit einer CTH von weniger als 2,5 km. Dies deutet darauf hin, dass tiefere und stärker entkoppelte marine Grenzschichten (MBLs) dazu neigen, in unterkühlten Umgebungen Eis zu bilden. Insgesamt scheinen diese Veränderungen eher von äußeren Faktoren als von der Morphologie beeinflusst zu werden.

Die Hypothese der Präkonditionierung wird von *Abel et al.* (2017) und *Tornow et al.* (2021) formuliert und besagt, dass die Umwandlung von geschlossen zu offen in MPCs im Vergleich zu unterkühlten (bzw. supercooled) flüssigen Wolken (SLCs) in Fallstudien bevorzugt wird. Daraus könnte man schließen, dass offene MCC-Wolken bevorzugt als MPCs auftreten. Dies kann jedoch durch den Mischungsanteil offener und geschlossener MCC-Wolken nicht bestätigt werden. Da das LWP:IWP (Eiswasserpfad)-Verhältnis nicht untersucht wird, könnte der Mischungsanteil auch MPCs mit geringem IWPs enthalten, die die Auswirkungen der Eisbildung auf die Wolkenmorphologie beeinflussen können (*Eirund et al.*, 2019a). Somit deuten diese Ergebnisse darauf hin, dass die Präkonditionierung keinen Einfluss auf die Umwandlung von geschlossener zu offener Wolke in der allgemeinen Klimatologie von marinem Stratocumulus zu haben scheint.

Die Untersuchung des Zusammenhangs zwischen Wolkenmorphologie und In-Wolken-Albedo zeigt erhebliche Unterschiede in der In-Wolken-Albedo zwischen offenen und geschlossenen Zellen von 0,07 bis 0,13, je nach Wolkenphase und Jahreszeit. Dies steht im Einklang mit den Ergebnissen von *McCoy et al.* (2017), die eine höhere In-Wolken-Albedo in geschlossenen MCC-Wolken als in offenen Wolken zeigen, selbst bei gleichem Bedeckungsgrad. Diese saisonalen und wolkenphasenabhängigen Unterschiede in der In-Wolken-Albedo können zu Änderungen der Wolkenstrahlungswirkung von $21\,\mathrm{W\,m^{-2}}$ bis $39\,\mathrm{W\,m^{-2}}$ im SO führen. Darüber hinaus zeigen die Wolkenphasenunterschiede innerhalb der MCC-Organisationen, dass die Unterschiede in der In-Wolken-Albedo in SLCs stärker ausgeprägt sind als in MPCs in beiden MCC-Regimen.

6.4.2 Exploration der Auswirkungen der MCC-Zellgröße

Um zu untersuchen, wie die Zellgrößen von MCC-Zellen durch die Wolkenphase beeinflusst werden, habe ich eine automatische Bildsegmentierungsmethode auf der Grundlage von $200\times200\,\mathrm{km^2}$ Moderate Resolution Imaging Spectroradiometer (MODIS) 0,86 µm-Reflexionsszenen entwickelt (*Platnick et al.*, 2015). Der äquivalente mittlere Zelldurchmesser in offenen und geschlossenen MCC-Wolken ist in MPCs und SLCs im Jahresmittel ähnlich. Allerdings sind die jahreszeitlichen Unterschiede im Zelldurchmesser zwischen MPCs und SLCs erheblich. Während im Südsommer der mittlere Zelldurchmesser der MPCs größer ist als der der SLCs, sind die MPCs im Südwinter in beiden MCC-Organisationen kleiner als die SLCs. Die saisonalen Veränderungen der Zellgröße in MPCs sind in beiden MCC-Regimen größer als in SLCs, was die Bedeutung der saisonalen Unterschiede in den beiden MCC-Regimen unterstreicht. Obwohl die automatische Segmentierungsmethode sorgfältig getestet und so konzipiert wurde, dass eine Verzerrung der Zelldurchmesser vermieden wird, können verbleibende kleine Verzerrungen nicht ausgeschlossen werden.

Um die unterschiedlichen CTHs in den Wolkenzellen zu berücksichtigen, werden die Seitenverhältnisse analysiert, um weitere Erkenntnisse über die Abhängigkeit der Zellgröße von der Wolkenmorphologie und -phase zu gewinnen. Geschlossene MCC-Wolken weisen im Jahresmittel ein kleineres Seitenverhältnis auf als offene MCC-Zellen. Geschlossene MCC-Zellen sind also unabhängig von der CTH kleiner als offene Zellen. Ich konnte feststellen, dass die beobachteten jahreszeitlichen Unterschiede im Zelldurchmesser sich nicht auf das Seitenverhältnis geschlossener MCC-Wolken auswirken, während sie bei offenen MCC-Wolken erkennbar sind. Daher sind die jahreszeitlichen Unterschiede im Zelldurchmesser in geschlossenen MCC-Zellen hauptsächlich auf Veränderungen der CTH zurückzuführen, während in offenen MCC-Zellen die jahreszeitlichen Schwankungen unabhängig

von der CTH sind.

Die In-Wolken-Albedo nimmt sowohl in offenen als auch in geschlossenen MCC-Wolken mit zunehmendem Seitenverhältnis ab. Der stärkste Rückgang ist in offenen MPCs zu verzeichnen. Darüber hinaus liegen die Unterschiede in der In-Wolken-Albedo aufgrund von Wolkenphasenänderungen typischerweise bei 0,2 und bei niedrigen Seitenverhältnissen bei bis zu 0,25. In-Wolken-Albedo-Änderungen von 0,2 - 0,25 entsprechen Wolkenstrahlungseffekten von 60 - 75 $\mathrm{W\,m^{-2}}$, was die korrekte Vorhersage der MCC-Wolkenzellengröße und der Wolkenphase in Klimamodellen unterstreicht.

6.4.3 Globale MCC-Klimatologie mit CNN

Die Erkennung der MCC-Organisation unabhängig von der Wolkenphase ist für die Untersuchung von MPCs mit niedrigen LWPs oder Eisphasenwolken unerlässlich. Aus diesem Grund wurde im Rahmen der Masterarbeit von *Reichel* (2022) ein faltendes neuronales Netzwerk (CNN) auf der Grundlage von $224\times224\,\mathrm{km^2}$ MODIS-Szenen aus dem 0,86 µm-Reflexionsband erstellt. Die Testleistung des gesamten CNN zeigt eine Genauigkeit von 80,6%, mit noch höheren Genauigkeiten in den Kategorien Offen (85,5%) und Geschlossen (87,3%). Die Fehlklassifikationen zwischen offenen und geschlossenen Kategorien sind mit weniger als 1,2% sehr gering. Die Auswertung des CNN zeigt, dass man sich auf die Szenenklassifizierung von Offen und Geschlossen verlassen kann.

Um unser Verständnis der verschiedenen MCC-Organisationen zu verbessern, werden die jährlichen und saisonalen Häufigkeiten des globalen MCC-Vorkommens aus dem Jahr 2008 mit dem CNN klassifiziert. Im Allgemeinen nehmen geschlossene MCC-Wolken mit der geografischen Breite ab ±30° N in Richtung hoher Breiten zu, während offene MCC-Wolken hauptsächlich innerhalb der Sturmzugbahnen auftreten und ihren Höhepunkt etwa bei ±45° N erreichen. Insgesamt stimmt die globale MCC-Klimatologie mit anderen MCC-Verteilungen überein (*Wood and Hartmann*, 2006; *Muhlbauer et al.*, 2014; *McCoy et al.*, 2017; *Mohrmann et al.*, 2021; *Lang et al.*, 2022, 2023). Der auffälligste Unterschied in der Häufigkeit tritt in den NH im Nordwinter auf. Im Vergleich zu Studien, die auf dem LWP basieren (*Muhlbauer et al.*, 2014; *McCoy et al.*, 2017), zeige ich eine Zunahme von geschlossenen und offenen MCC-Wolken in der NH. Diese Zunahme von MCC in der NH während des Winters könnte durch fehlende MCC-MPCs verursacht werden, da die Studie von *Muhlbauer et al.* (2014) auf warme Wolkenszenen (CTT >273 K) beschränkt ist und MPCs mit einem niedrigen LWP möglicherweise nicht erkannt werden (*Muhlbauer et al.*, 2014; *McCoy et al.*, 2017).

6.5 Fazit

Insgesamt können Veränderungen der Wolkenphase, Wolkenmorphologie oder Zellgröße in einem sich erwärmenden Klimasystem erhebliche Auswirkungen haben, da sie die Strahlungseigenschaften der Wolken verändern. Vor allem im SO bleiben niedrige Wolken die größte Unsicherheit in globalen Klimamodellen (*Bony and Dufresne*, 2005; *Bony et al.*, 2006, 2015; *Zelinka et al.*, 2020; *Schuddeboom and McDonald*, 2021). Im Allgemeinen prognostizieren globale Klimamodelle eine Abnahme der Wolkenbedeckung, was zu einer positiven Rückkopplung führt, die die Erwärmung durch eine geringere Albedo verstärkt (*Clement et al.*, 2009; *Qu et al.*, 2015; *Myers and Norris*, 2016; *Norris et al.*, 2016; *Myers et al.*, 2021; *Zelinka et al.*, 2020). Die mögliche Rückkopplung der Wolkenmorphologie wird von *McCoy et al.* (2017) vermutet. Sie argumentieren, dass eine Abschwächung der Stärke von marinen Kaltluftausbrüchen (MCAO), die von *Kolstad and Bracegirdle* (2008) in der NH gefunden wurde, zu weniger offenen und mehr geschlossenen MCC-Zellen führen könnte, wenn die Erkenntnisse von *Kolstad and Bracegirdle* (2008) global angenommen werden können. Diese Korrelation zwischen MCAOs und Wolkenmorphologie (Fig. S7) und die Unterschiede in der In-Wolken-Albedo (Table 3 and Fig. 26) zwischen offenen und geschlossenen MCC-Zellen könnten die Wolkenrückkopplung teilweise ausgleichen und zu einem insgesamt geringeren Rückgang der niedrigen Wolken führen.

Zusätzlich zu den Veränderungen der Wolkenmorphologie in einem sich erwärmenden Klimasytem wird eine Verschiebung der Wolkenphase hin zu mehr warmen Flüssigwolken und weniger MPCs und SLCs in mittleren bis hohen Breiten erwartet. In vorherigen Studien wurde die Rückkopplung der Wolkenphase als negative Rückkopplung definiert, die zu optisch dickeren Wolken mit einer höheren Albedo führt (*Storelvmo et al.*, 2015; *Gettelman and Sherwood*, 2016). Neueste Studien (*Murray et al.*, 2021; *Wall et al.*, 2022) zeigen jedoch, dass die Wolkenphasenrückkopplung nur geringfügig zur gesamten Wolkenrückkopplung beiträgt, da sie von der optischen Dicke der MPCs abhängt, die häufig bereits optisch dick sind. Dennoch kann die Phasenverschiebung aufgrund einer geringeren Niederschlagseffizienz in flüssigen Wolken zu einer längeren Lebensdauer führen (*Tan and Storelvmo*, 2019; *Mülmenstädt et al.*, 2021). Während in dieser Arbeit keine Belege dafür gefunden wurden, dass innerhalb von MPCs durch Präkonditionierung häufiger offene Zellen als geschlossene Zellen auftreten, ist Niederschlag einer der wichtigsten Treiber der Umwandlung von geschlossen zu offen Zellen (*Yamaguchi and Feingold*, 2015; *Abel et al.*, 2017; *Eastman et al.*, 2021, 2022). Somit könnte die Eis-zu-Flüssig-Umwandlung zu weniger Niederschlag in warmen MCC-Wolken und zu weniger Übergängen von geschlossenen zu offenen MCC-Wolken in warmen Wolken führen. Dies könnte daher möglicherweise zu noch mehr geschlossenen MCC-Wolken im Vergleich zu offenen Zellen und damit zu einer höheren Albedo führen als durch die Rückkopplung der Wolkenmorphologie allein.

Zusammenfassend lässt sich sagen, dass diese beiden Rückkopplungen zu einer insgesamt positiven Rückkopplung führen könnten. Es handelt sich jedoch um ein sehr komplexes System mit vielen anderen Umweltfaktoren, die sich mit dem Klimawandel verändern, z.B. eine Zunahme der INPs (*Murray et al.*, 2021; *Twohy et al.*, 2021), der MBL-Höhe (*Díaz et al.*, 2019) oder der Wolkenlebensdauer (*Tan and Storelvmo*, 2019), die hier nicht diskutiert werden. Insgesamt zeigt dies, wie wichtig es ist, die Wolkenvorhersage in globalen Klimamodellen zu verbessern.

Abschließend zeigt diese Arbeit, dass jahreszeitliche Veränderungen bei den Einflussfaktoren für die Wolkenbildung die SO-Stratocumulus-Wolkenphase stärker beeinflussen als Unterschiede in der Wolkenmorphologie und damit die wolkengetriebene Dynamik. Sowohl die Wolkenphase als auch die Wolkenmorphologie scheinen hauptsächlich durch andere Umweltfaktoren gesteuert zu werden. Veränderungen der Wolkenphase können die In-Wolken-Albedo bei niedrigen Seitenverhältnissen um bis zu 0,25 verändern, was mit einem Wolkenabstrahleffekt von $75\,\mathrm{W\,m^{-2}}$ im SO einhergeht. Im Fokus dieser Dissertation steht das Verständnis der Abhängigkeiten von Wolkenphase, Morphologie und Zellgröße, um die Vorhersage des Wolkenstrahlungseffekts zu verbessern.

A Supplementary Figures

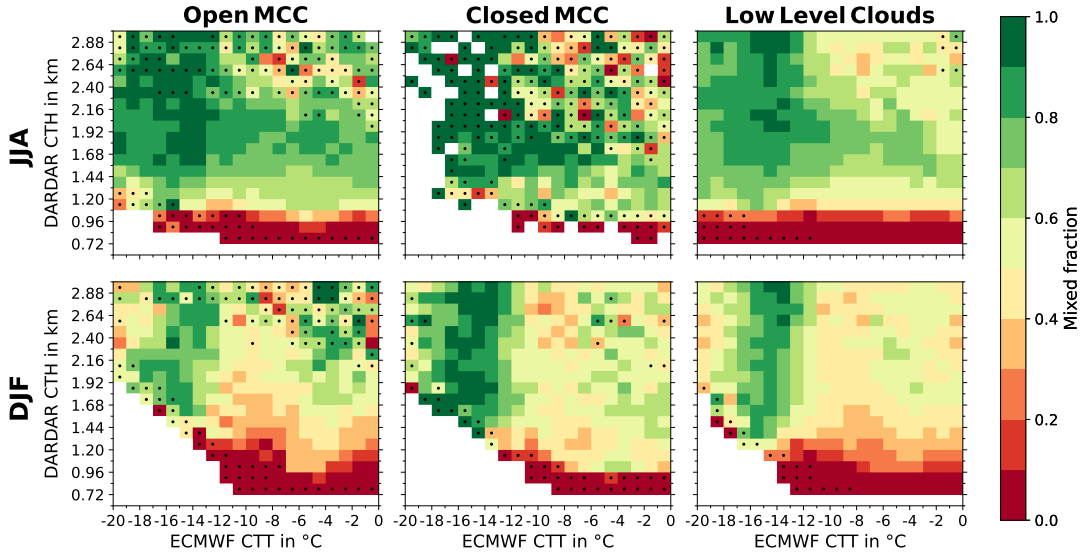

FIG. S1 Two-dimensional histograms of mixed fraction against CTT and CTH for (left) open MCC, (middle) closed MCC, and (right) low-level clouds in austral (top) winter and (bottom) summer. Dotted bins indicate bins with less than 50 data points.

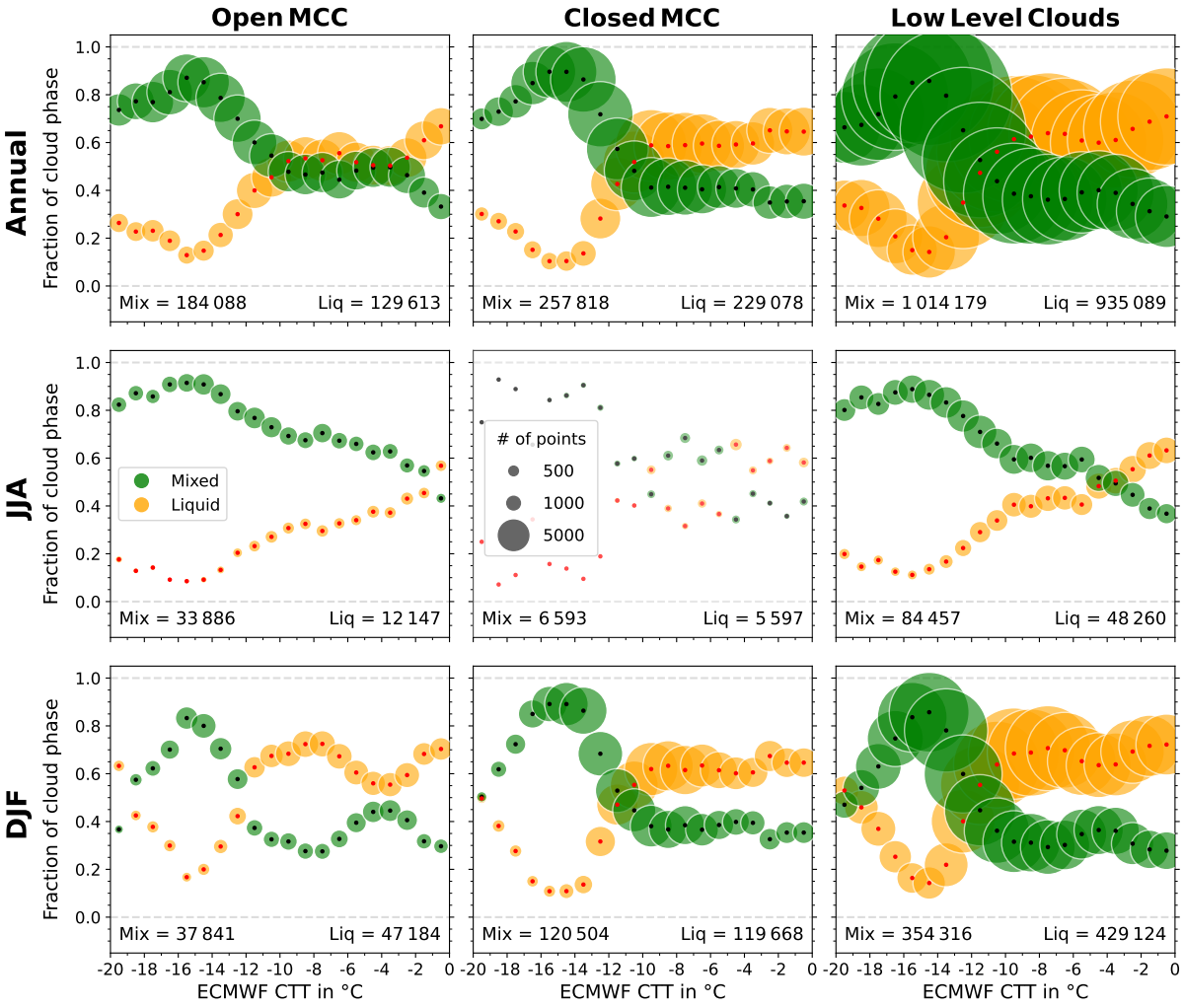

FIG. S2 Supercooled liquid and mixed fraction binned by CTT from -20 °C to 0 °C with a bin width of 1 °C (2007 - 2010) for (top) all seasons, (middle) austral winter and (bottom) austral summer in (left) open MCC, (middle) closed MCC, and (right) low-level clouds for clouds with an effective radius 0 µm $< R_e <$ 14 µm. As only 5.1 % of the annual closed MCC clouds occur in JJA the panel is displayed in more transparent color shading.

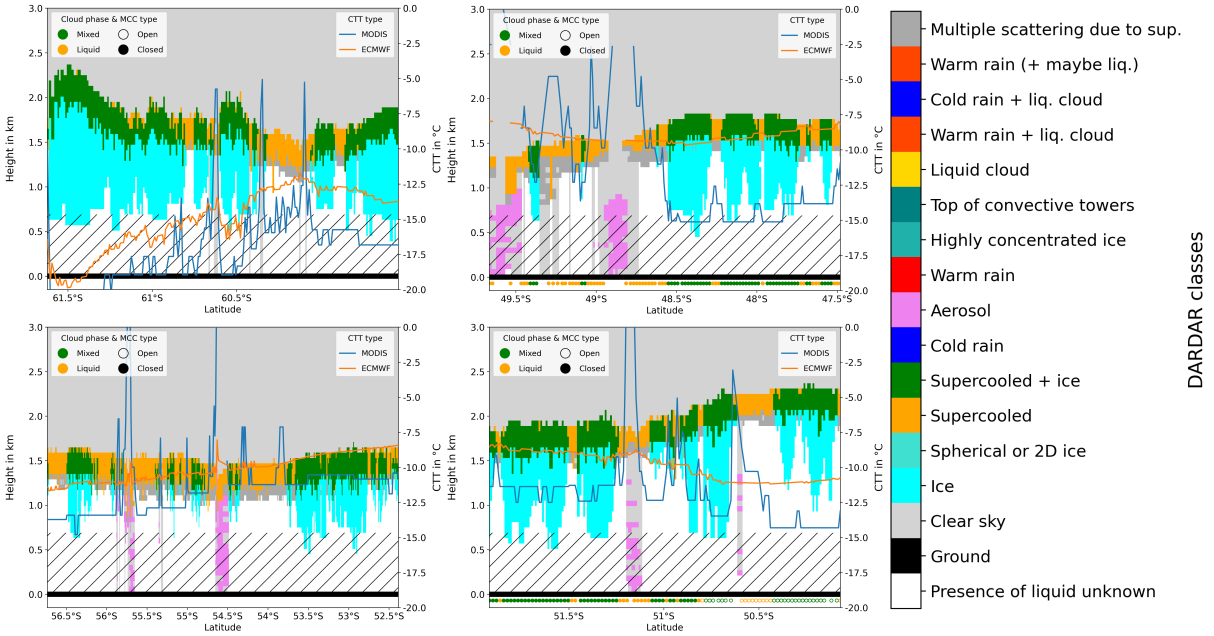

FIG. S3 Four example tracks of the DARDAR categorization on 1 December 2007. The blue line indicates the CTT of MODIS and the orange of ECMWF. The hatched area displays levels below 720 m. The colored circles below the ground show the newly defined vertically integrated cloud phase and the MCC type for every other data point.

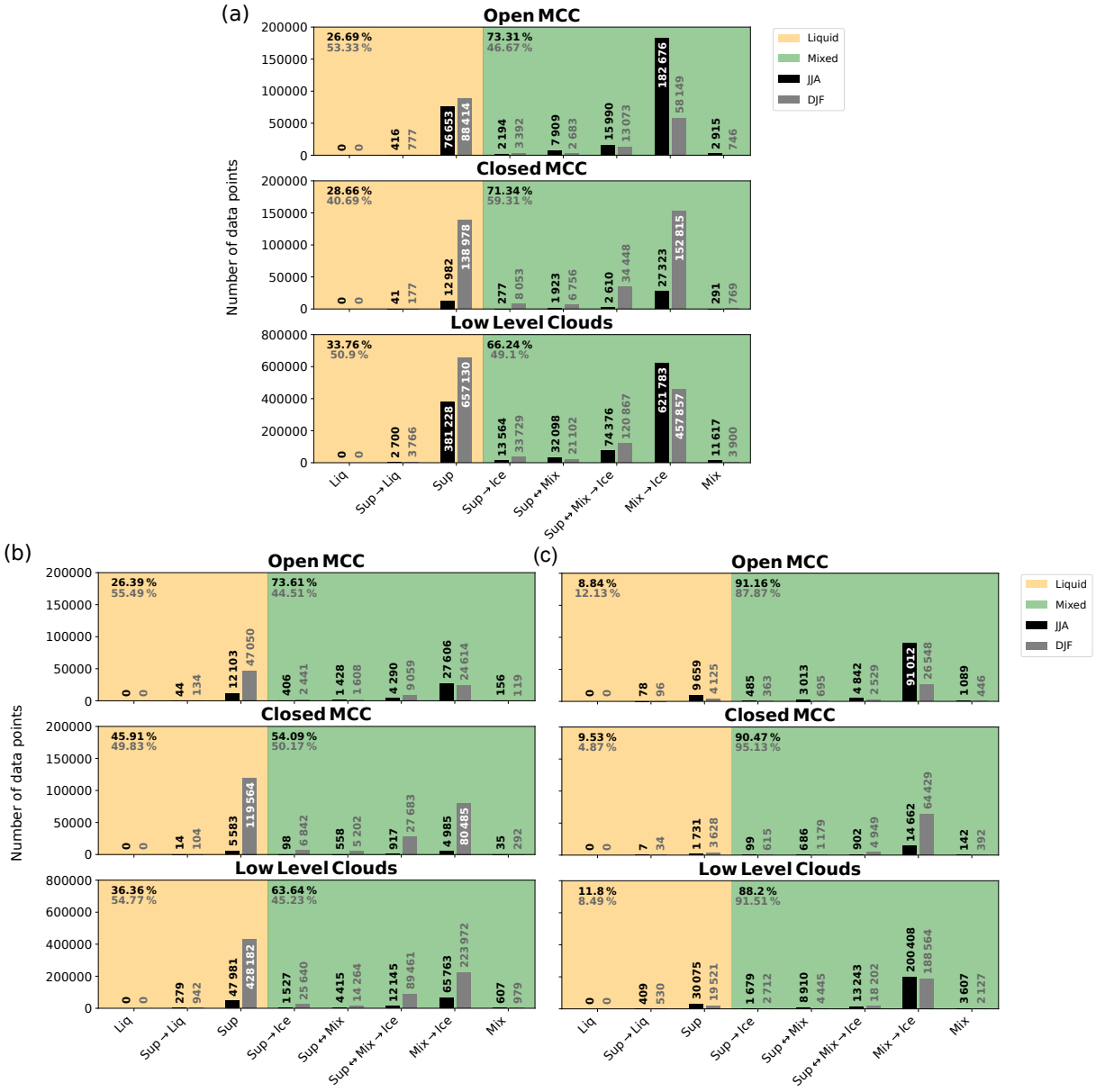

FIG. S4 (a) Histogram of data points of vertically resolved cloud phase types divided into two categories: liquid clouds (orange) and MPCs (green) for austral winter (black) and summer (grey) in the temperature range from -20 °C to 0 °C from 2007 to 2010. Overall percentage of liquid clouds and MPCs is indicated in each panel separately for JJA (black) and DJF (grey). "→" indicates the layer on top of the next. "↔" indicates interchangeable layers. (b) Same as (a) but only for clouds with an effective radius 0 µm < R_e <14 µm. (c) Same as (a) but only for clouds with an effective radius R_e >14 µm.

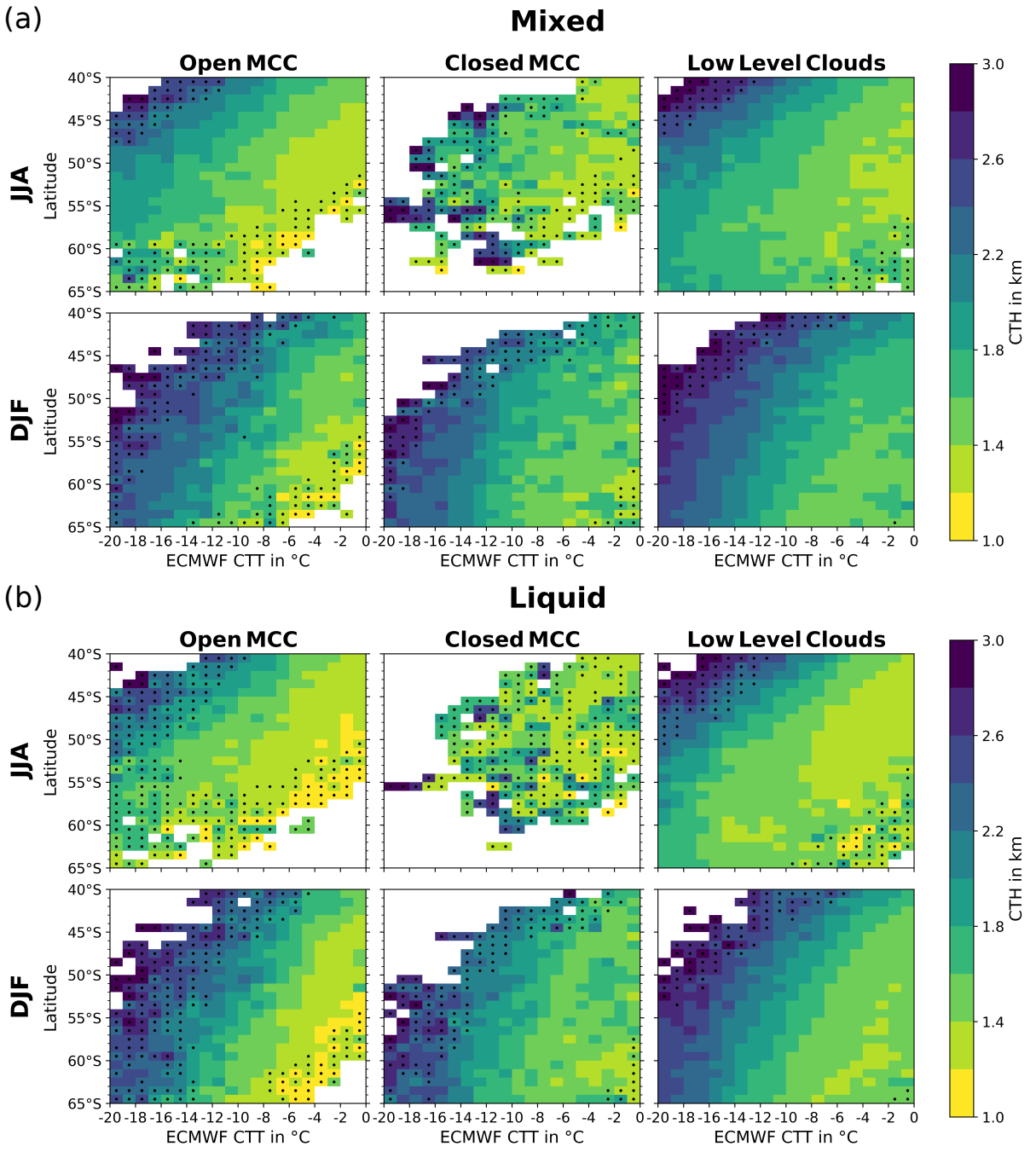

FIG. S5 Two-dimensional histograms of CTH against CTT and latitude for (left) open MCC, (middle) closed MCC, and (right) low-level clouds in (1. and 3. row) austral winter and (2. and 4. row) summer separately for (a) MPCs and (b) SLCs. Dotted bins indicate bins with less than 50 data points.

(a)

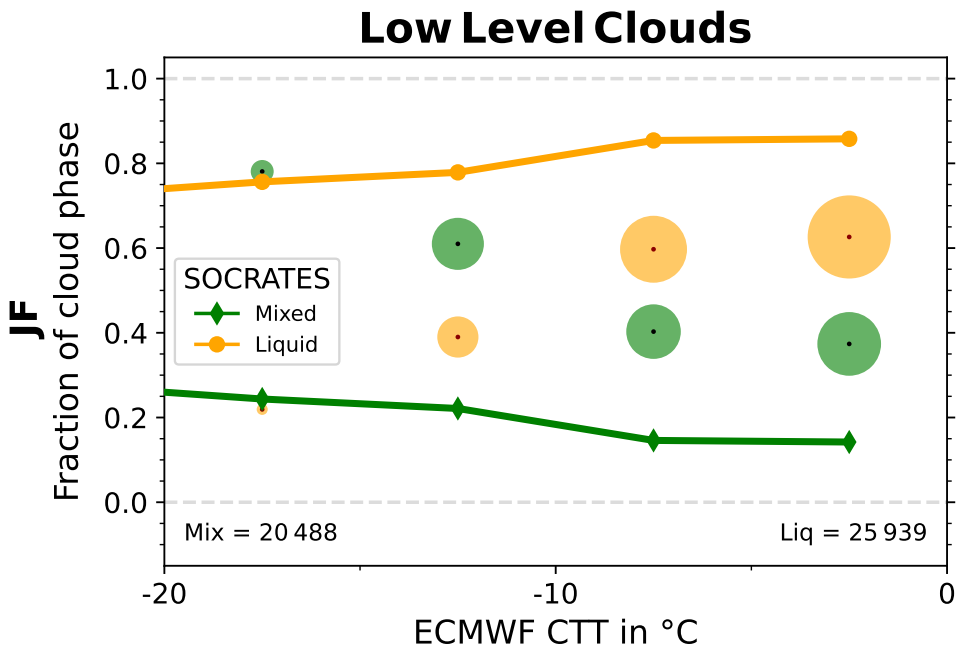

(b)

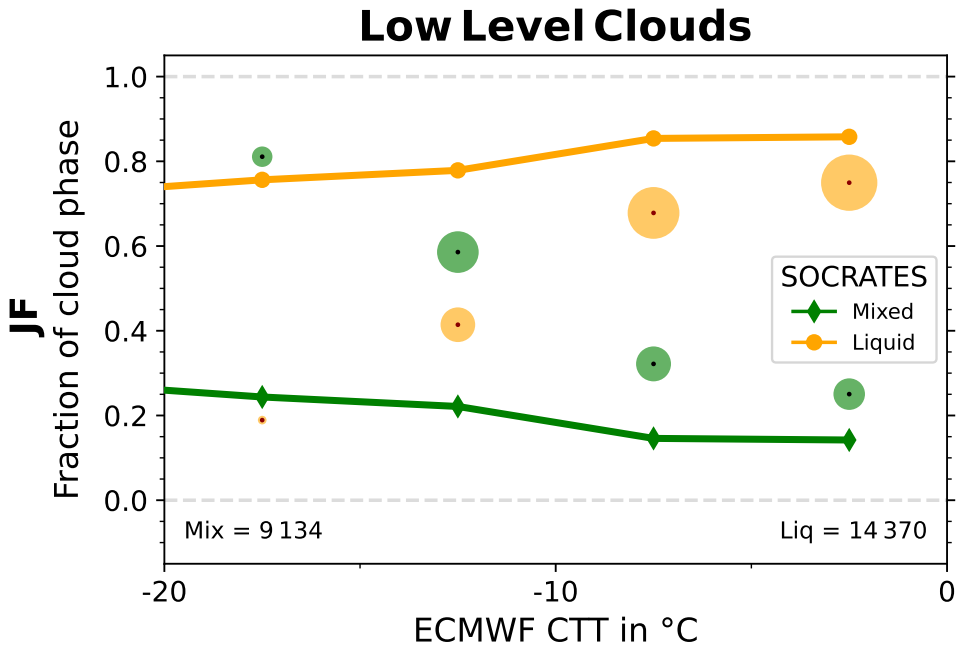

FIG. S6 (a) Supercooled liquid and mixed fraction binned by CTT from -20 °C to 0 °C with a bin width of 5 °C (2007 - 2010) for January and February in low-level clouds. The months and region (42° S to 62° S and from 133° W to 163° W) are set to match the SOCRATES campaign. SOCRATES data is adapted from Fig. 4 by *D'Alessandro et al.* (2021). (b) Same as (a) but only for clouds with an effective radius 0 µm $< R_e <$ 14 µm

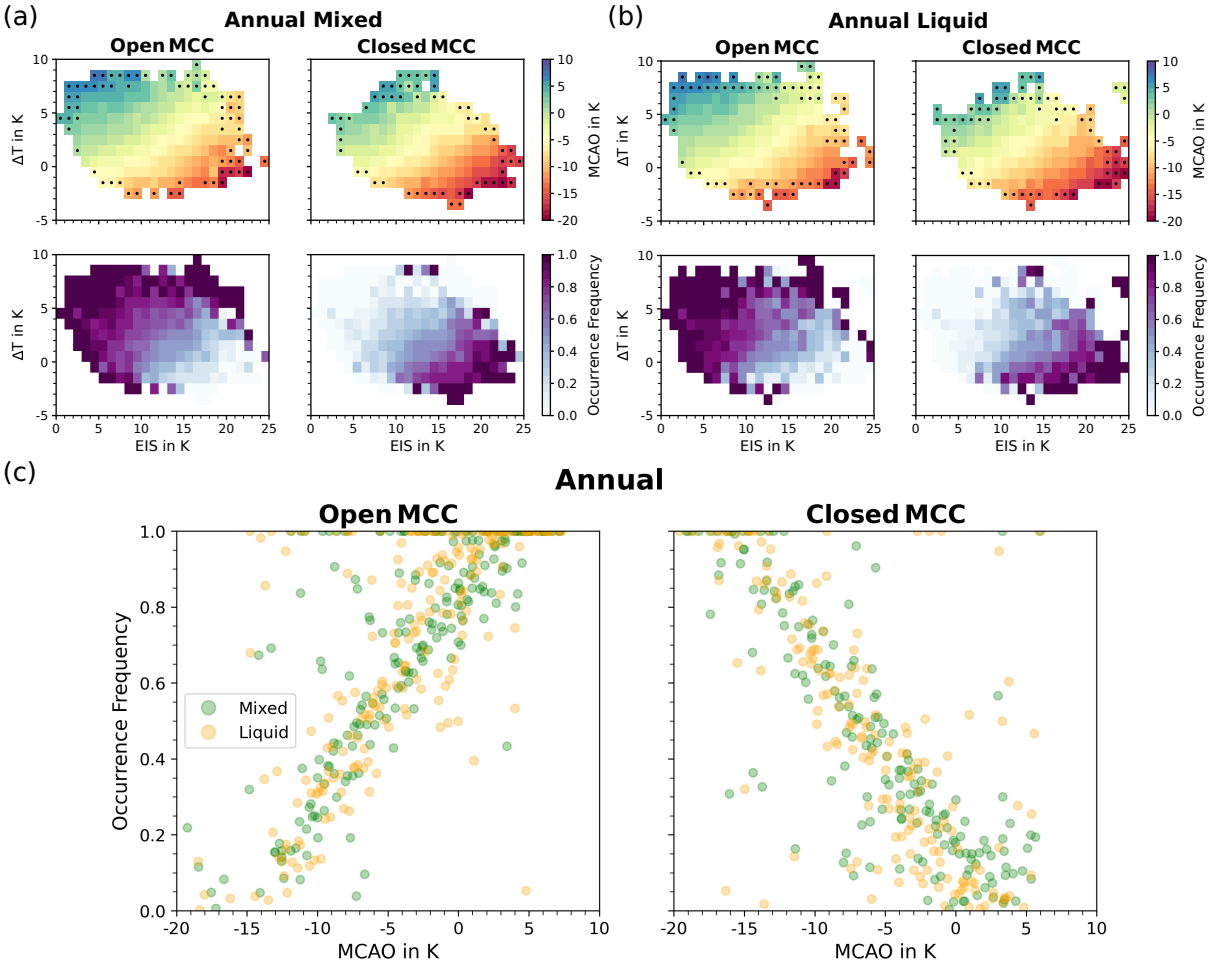

FIG. S7 (a) Two-dimensional histograms of (top) the MCAO and (bottom) occurrence frequency against ΔT and EIS separately for (left) open MCC and (right) closed MCC MPCs. Dotted bins indicate bins with less than 100 data points. (b) Same as (a) but for SLCs. (c) ΔT–EIS composites computed from the data in (a) for MPCs and (b) for SLCs separated in MPCs and SLCs for (left) open MCC and (right) closed MCC clouds binned by the MCAO index. This figure is produced in a similar way as from Fig. 8, and 9 by *McCoy et al.* (2017) but separately for MPCs and SLCs. [As MPCs and SLCs occur evenly across the MCAO index, the correlation between ice occurrence and vertical acceleration does not seem to be driven by surface fluxes.]

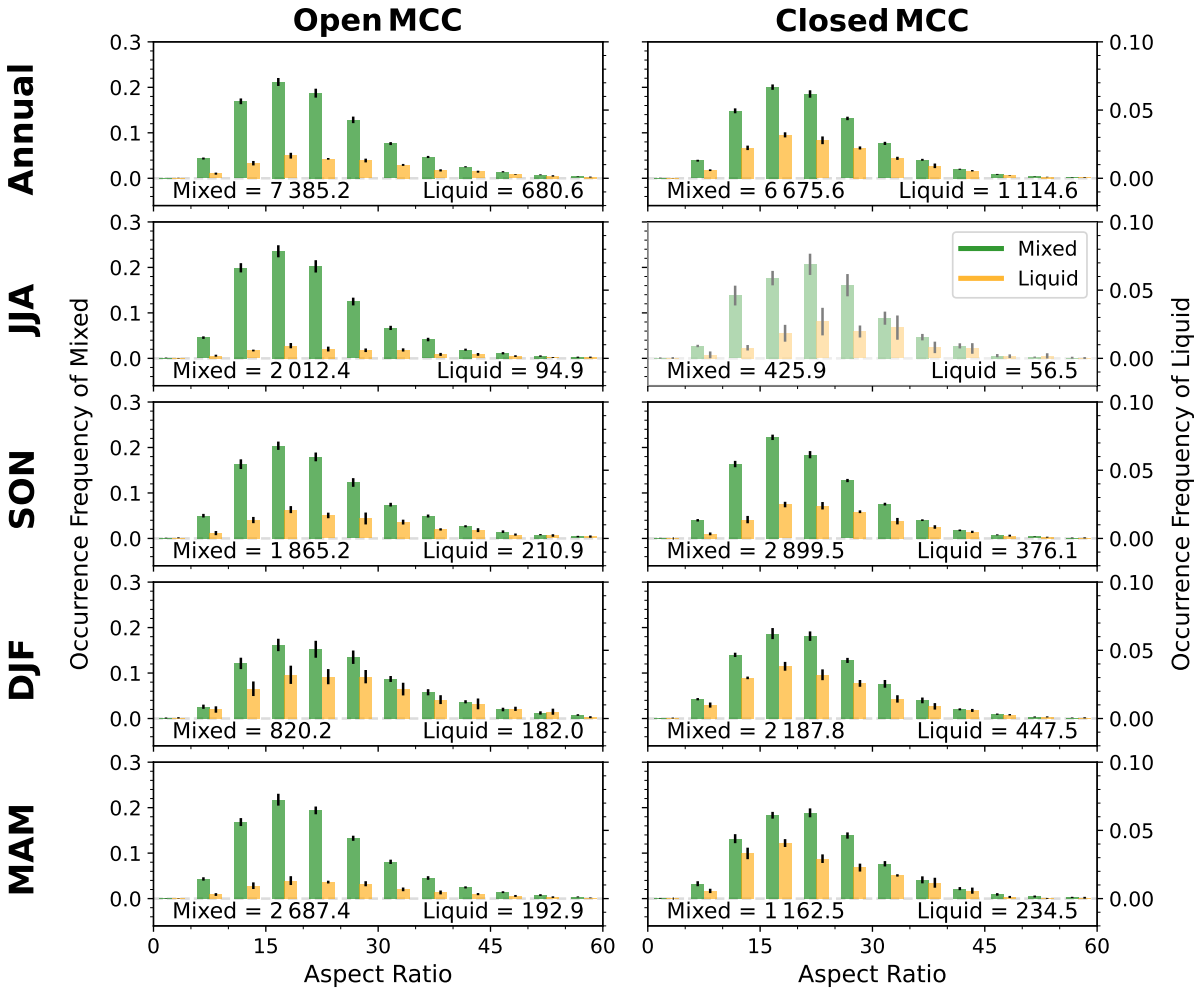

FIG. S8 Same as Fig. 22, but for aspect ratio.

TABLE S1 Same as Table 6, but the classified MCC type is based on most occurring MCC type in the 1°×1° gridded product of the CNN using the MODIS 0.55 µm reflectance band from *Yuan et al.* (2020) for the year 2007.

	Open	**Closed**	**Open**		**Closed**	
			MPC	SLC	MPC	SLC
Annual	26.81	22.43	25.59	31.44	22.14	24.17
JJA	26.15	21.65	25.73	27.79	21.29	24.76
SON	27.07	22.77	26.07	31.07	22.41	25.32
DJF	28.28	22.90	26.74	32.64	22.70	23.67
MAM	26.18	21.67	24.67	32.64	21.51	22.86

TABLE S2 Same as Table 7, but the classified MCC type is based on most occurring MCC type in the 1°×1° gridded product of the CNN using the MODIS 0.55 µm reflectance band from *Yuan et al.* (2020) for the year 2007.

		Open	**Closed**	**MPC**	**SLC**
	Open vs Closed	MPC vs SLC	MPC vs SLC	Open vs Closed	Open vs Closed
Annual	1.0	0.625	1.0	1.0	0.875
JJA	0.625	0.0	0.875	0.25	0.0
SON	0.625	0.0	1.0	0.0	0.0
DJF	0.75	0.125	0.25	0.5	0.625
MAM	0.625	0.125	0.5	0.375	0.5

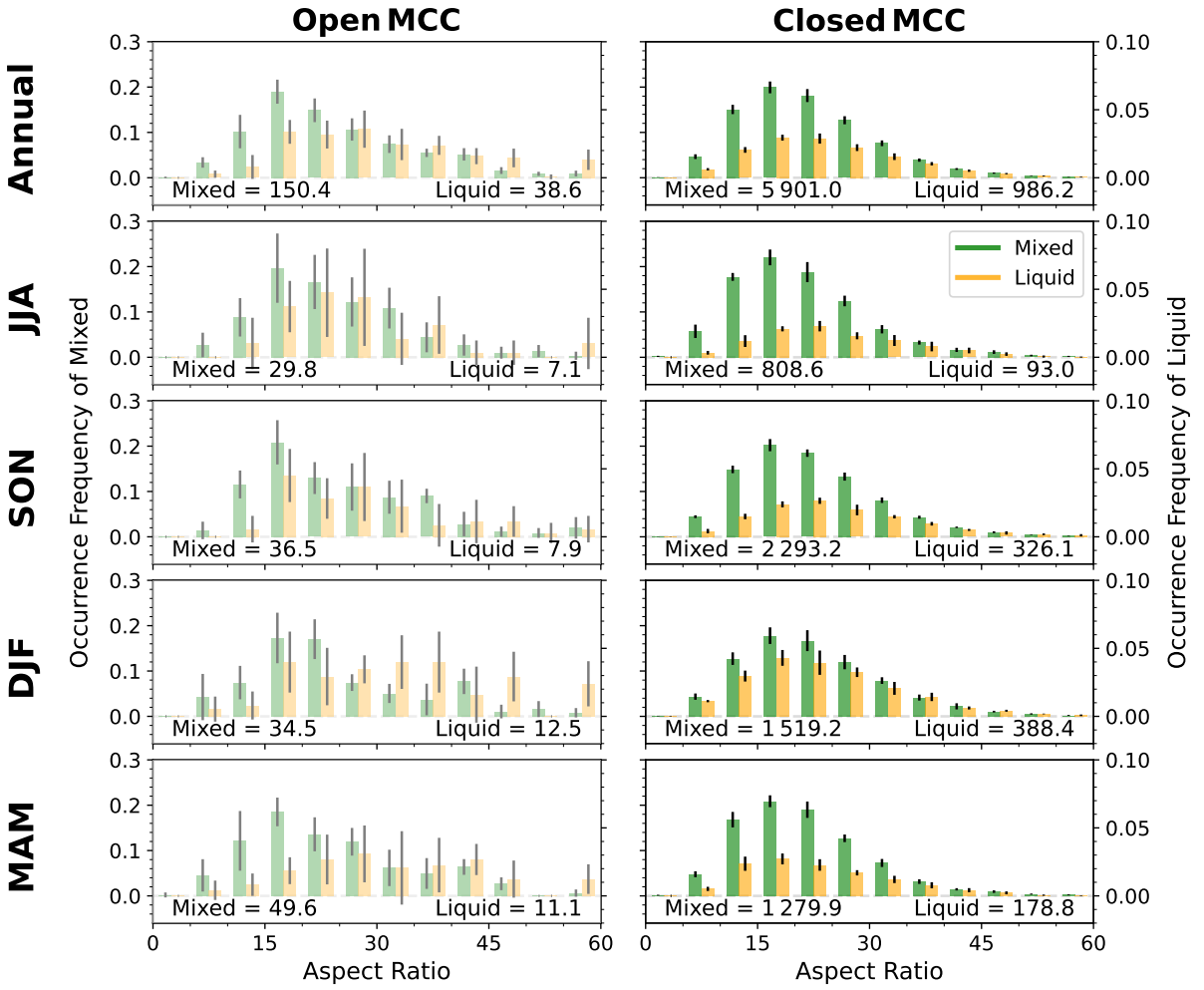

FIG. S9 Histogram of cloud phase occurrence frequency binned by aspect ratio with a bin width of 5 for CTT from −20 °C to 0 °C normalized by the sum of SLCs and MPCs, but the classified MCC type is based on most occurring MCC type in the 1°×1° gridded product of the CNN using the MODIS 0.55 µm reflectance band from *Yuan et al.* (2020) for the year 2007. Note different y-axes for SLCs and MPCs. Numbers below the histogram indicate the mean number of identified cells for MPCs and SLCs. As only very few open MCC clouds are identified, all open panels are displayed in more transparent color shading.

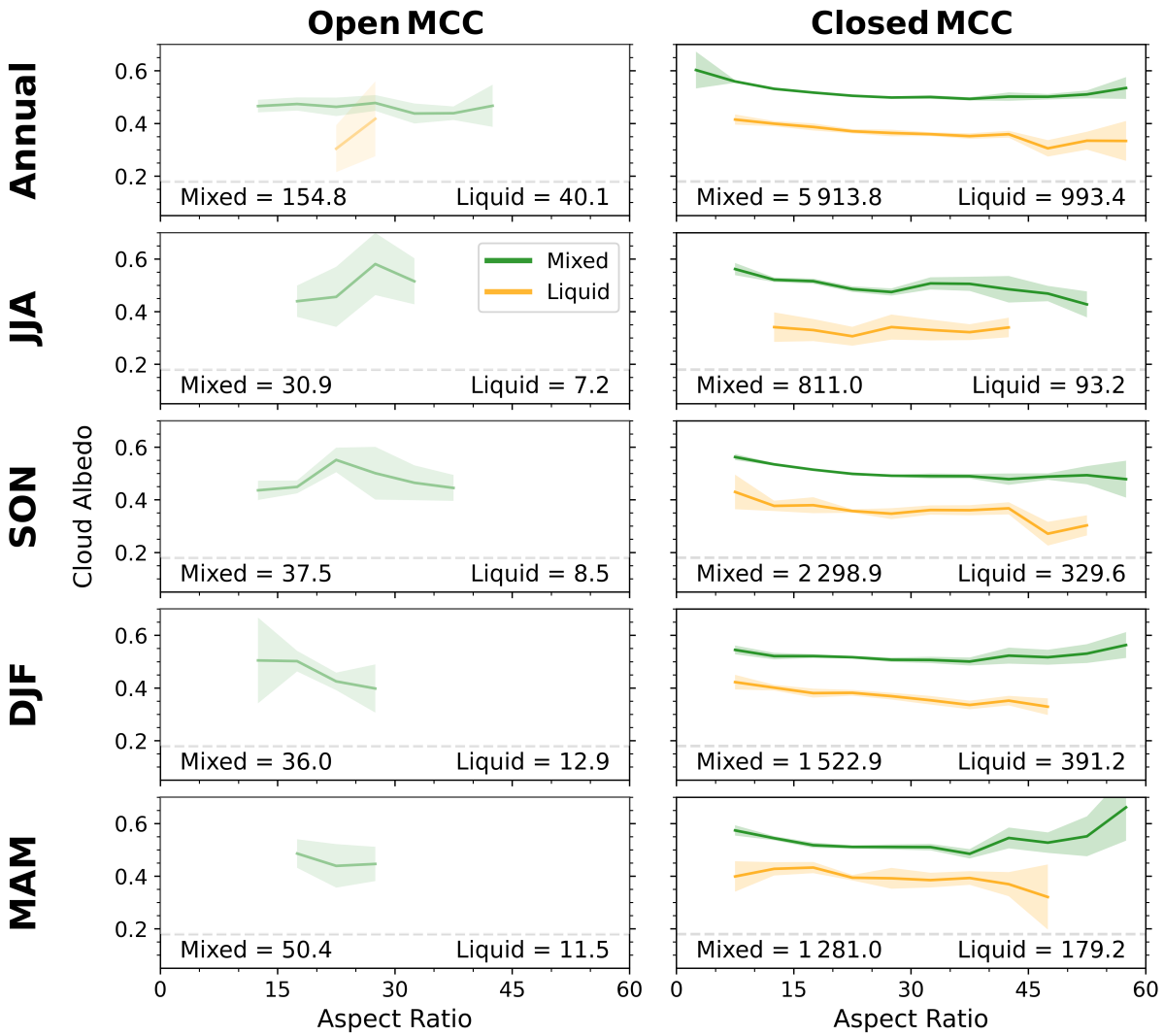

FIG. S10 Mean in-cloud albedo as a function of aspect ratio for SLCs and MPCs with CTT from −20 °C to 0 °C, but the classified MCC type is based on most occurring MCC type in the 1°×1° gridded product of the CNN using the MODIS 0.55 µm reflectance band from *Yuan et al.* (2020) for the year 2007. Numbers below the lines indicate the mean number of identified cells for MPCs and SLCs. As only very few open MCC clouds are identified, all open panels are displayed in more transparent color shading.

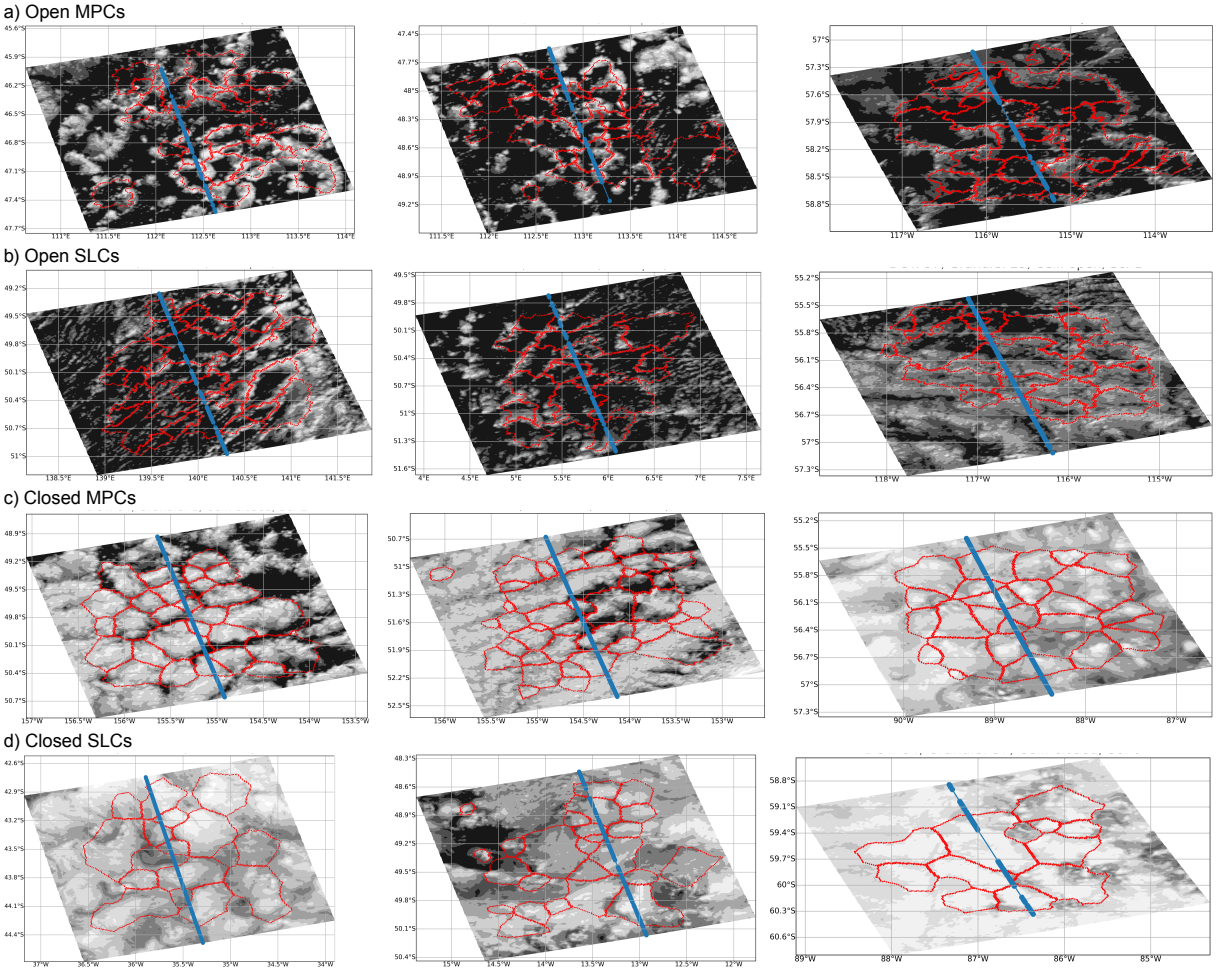

FIG. S11 Examples scenes with red outlines of segmented cells for (a) open MPCs, (b) open SLCs, (c) closed MPCs, and (d) closed SLCs.

B List of Abbreviations

CALIOP	Cloud-Aerosol Lidar with Orthogonal Polarization
CALIPSO	Cloud-Aerosol Lidar and Infrared Pathfinder Satellite Observations
CAPRICORN	Clouds, Aerosols, Precipitation, Radiation, and atmospherIc Composition Over the southeRN ocean campaign
CBH	cloud-base height
CNN	convolutional neural network
COT	cloud optical thickness
CTH	cloud-top height
CTT	cloud-top temperature
DARDAR	liDAR-raDAR
DJF	December to January
ECMWF	European Centre for Medium-Range Weather Forecasts
EIS	estimated inversion strength
INP	ice nucleating particle
IWP	ice water path
JJA	June to August
LW	longwave
LWP	liquid water path
MAM	March to May
MBL	marine-boundary layer
MCAO	marine cold air outbreak
MCC	mesoscale-cellular convective
MERRA-2	Modern-Era Retrospective analysis for Research and Applications version 2
MODIS	Moderate Resolution Imaging Spectroradiometer
MPC	mixed-phase cloud
NCEP	National Centers for Environmental Prediction
NH	Northern Hemisphere
PDF	probability density function

ReLu	rectified linear unit
SH	Southern Hemisphere
SLC	supercooled liquid cloud
SO	Southern Ocean
SOCRATES	Southern Ocean Clouds Radiation Aerosol Transport Experimental Study
SON	September to November
SST	sea surface temperature
SW	shortwave
WBF	Wegener-Bergeron-Findeisen

References

Abadi, M., A. Agarwal, P. Barham, E. Brevdo, Z. Chen, C. Citro, G. S. Corrado, A. Davis, J. Dean, M. Devin, S. Ghemawat, I. Goodfellow, A. Harp, G. Irving, M. Isard, Y. Jia, R. Jozefowicz, L. Kaiser, M. Kudlur, J. Levenberg, D. Mane, R. Monga, S. Moore, D. Murray, C. Olah, M. Schuster, J. Shlens, B. Steiner, I. Sutskever, K. Talwar, P. Tucker, V. Vanhoucke, V. Vasudevan, F. Viegas, O. Vinyals, P. Warden, M. Wattenberg, M. Wicke, Y. Yu, and X. Zheng (2016), TensorFlow: Large-Scale Machine Learning on Heterogeneous Distributed Systems, in *Proc. 12th USENIX Conf. Operating Systems Design and Implementation (chairs Keeton, K. & Roscoe, T.)*, USENIX Association, 2016, doi:10.48550/ARXIV.1603.04467. 62

Abel, S. J., I. A. Boutle, K. Waite, S. Fox, P. R. A. Brown, R. Cotton, G. Lloyd, T. W. Choularton, and K. N. Bower (2017), The Role of Precipitation in Controlling the Transition from Stratocumulus to Cumulus Clouds in a Northern Hemisphere Cold-Air Outbreak, *Journal of the Atmospheric Sciences*, *74*(7), 2293–2314, doi:10.1175/jas-d-16-0362.1. 2, 4, 5, 8, 13, 48, 75, 78, 83, 84, 87

Achtert, P., E. J. Oconnor, I. M. Brooks, G. Sotiropoulou, M. D. Shupe, B. Pospichal, B. J. Brooks, and M. Tjernström (2020), Properties of Arctic liquid and mixed-phase clouds from shipborne Cloudnet observations during ACSE 2014, *Atmospheric Chemistry and Physics*, *20*(23), 14,983–15,002, doi:10.5194/acp-20-14983-2020. 49, 51

Adhikari, L., Z. Wang, and others (2013), An A-Train satellite based stratiform mixed-phase cloud retrieval algorithm by combining active and passive sensor measurements, *British Journal of Environment and Climate Change*, *3*(4), 587–611. 28

Agee, E. M. (1987), Mesoscale cellular convection over the oceans, *Dynamics of Atmospheres and Oceans*, *10*(4), 317–341, doi:10.1016/0377-0265(87)90023-6. 5, 7

Agee, E. M., T. S. Chen, and K. E. Dowell (1973), A Review of Mesoscale Cellular Convection, *Bulletin American Meteorological Society*, *54*(10), 1004–1012, doi:10.1175/1520-0477(1973)054⟨1004:aromcc⟩2.0.co;2. 5, 7, 56

Ahn, E., Y. Huang, T. H. Chubb, D. Baumgardner, P. Isaac, M. de Hoog, S. T. Siems, and M. J. Manton (2017), In situ observations of wintertime low-altitude clouds over

the Southern Ocean, *Quarterly Journal of the Royal Meteorological Society*, *143*(704), 1381–1394, doi:10.1002/qj.3011. 8, 37

Ahn, E., Y. Huang, S. T. Siems, and M. J. Manton (2018), A Comparison of Cloud Microphysical Properties Derived From MODIS and CALIPSO With In Situ Measurements Over the Wintertime Southern Ocean, *Journal of Geophysical Research: Atmospheres*, *123*(19), 120–11, doi:10.1029/2018JD028535. 37

Arking, A. (1991), The Radiative Effects of Clouds and their Impact on Climate, *Bulletin of the American Meteorological Society*, *72*(6), 795–813, doi:10.1175/1520-0477(1991)072⟨0795:treoca⟩2.0.co;2. 1

Atkinson, B. W., and J. Wu Zhang (1996), Mesoscale shallow convection in the atmosphere, *Reviews of Geophysics*, *34*(4), 403–431, doi:10.1029/96RG02623. 1, 5, 7, 56, 68

Barbedo, J. G. A. (2018), Impact of dataset size and variety on the effectiveness of deep learning and transfer learning for plant disease classification, *Computers and Electronics in Agriculture*, *153*, 46–53, doi:https://doi.org/10.1016/j.compag.2018.08.013. 25

Baum, B. A., W. P. Menzel, R. A. Frey, D. C. Tobin, R. E. Holz, S. A. Ackerman, A. K. Heidinger, and P. Yang (2012), MODIS cloud-top property refinements for collection 6, *Journal of Applied Meteorology and Climatology*, *51*(6), 1145–1163, doi:10.1175/JAMC-D-11-0203.1. 27

Bergeron, T. (1935), On the physics of clouds and precipitation, *Proces Verbaux de l'Association de Météorologie, International Union of Geodesy and Geophysics*, pp. 156–178. 11

Berner, A. H., C. S. Bretherton, R. Wood, and A. Muhlbauer (2013), Marine boundary layer cloud regimes and POC formation in a CRM coupled to a bulk aerosol scheme, *Atmospheric Chemistry and Physics*, *13*(24), 12,549–12,572, doi:10.5194/acp-13-12549-2013. 8

Berner, A. H., C. S. Bretherton, and R. Wood (2015), Large eddy simulation of ship tracks in the collapsed marine boundary layer: A case study from the Monterey area ship track experiment, *Atmospheric Chemistry and Physics*, *15*(10), 5851–5871, doi:10.5194/acp-15-5851-2015. 15

Bony, S., and J. L. Dufresne (2005), Marine boundary layer clouds at the heart of tropical cloud feedback uncertainties in climate models, *Geophysical Research Letters*, *32*(20), 1–4, doi:10.1029/2005GL023851. 63, 77, 87

Bony, S., R. Colman, V. M. Kattsov, R. P. Allan, C. S. Bretherton, J. L. Dufresne, A. Hall, S. Hallegatte, M. M. Holland, W. Ingram, D. A. Randall, B. J. Soden, G. Tselioudis, and M. J. Webb (2006), How well do we understand and evaluate climate change feedback processes?, *Journal of Climate*, *19*(15), 3445–3482, doi:10.1175/JCLI3819.1. 2, 13, 63, 77, 87

Bony, S., B. Stevens, D. M. W. Frierson, C. Jakob, M. Kageyama, R. Pincus, T. G. Shepherd, S. C. Sherwood, P. A. Siebesma, A. H. Sobel, M. Watanabe, and M. J. Webb (2015), Clouds, circulation and climate sensitivity, *Nature Geoscience*, *8*(4), 261–268, doi:10.1038/ngeo2398. 63, 77, 87

Boucher, O., and U. Lohmann (1995), The sulfate-CCN-cloud albedo effect: A sensitivity study with two general circulation models, *Tellus B: Chemical and Physical Meteorology*, *47*(3), 281, doi:10.3402/tellusb.v47i3.16048. 4

Boucher, O., and H. Rodhe (1994), The sulfate-CCN-cloud albedo effect: a sensitivity study, *Tech. rep.*, Department of Meteorology, Stockholm University, Stockholm. 4

Bretherton, C. S. (2015), Insights into low-latitude cloud feedbacks from high-resolution models, *Philosophical Transactions of the Royal Society A: Mathematical, Physical and Engineering Sciences*, *373*(20140415), doi:10.1098/rsta.2014.0415. 49

Bretherton, C. S., and D. L. Hartmann (2009), Large-scale Controls on Cloudiness, in *Clouds in the Perturbed Climate System*, pp. 217–234, The MIT Press, doi:10.7551/mitpress/9780262012874.003.0010. 4

Bretherton, C. S., and M. C. Wyant (1997), Moisture Transport, Lower-Tropospheric Stability, and Decoupling of Cloud-Topped Boundary Layers, *Journal of the Atmospheric Sciences*, *54*(1), 148–167, doi:10.1175/1520-0469(1997)054. 3, 5

Bretherton, C. S., J. Uchida, and P. N. Blossey (2010), Slow Manifolds and Multiple Equilibria in Stratocumulus-Capped Boundary Layers, *Journal of Advances in Modeling Earth Systems*, *2*(14), 1–20, doi:10.3894/JAMES.2010.2.14. 49

Brümmer, B. (1999), Roll and Cell Convection in Wintertime Arctic Cold-Air Outbreaks, *Journal of the Atmospheric Sciences*, *56*(15), 2613–2636, doi:10.1175/1520-0469(1999)056⟨2613:RACCIW⟩2.0.CO;2. 2, 4, 7

Bühl, J., A. Ansmann, P. Seifert, H. Baars, and R. Engelmann (2013), Toward a quantitative characterization of heterogeneous ice formation with lidar/radar: Comparison of CALIPSO/CloudSat with ground-based observations, *Geophysical Research Letters*, *40*(16), 4404–4408, doi:10.1002/grl.50792. 43

Burrows, S. M., C. Hoose, U. Pöschl, and M. G. Lawrence (2013), Ice nuclei in marine air: Biogenic particles or dust?, *Atmospheric Chemistry and Physics*, *13*(1), 245–267, doi:10.5194/acp-13-245-2013. 44

Ceccaldi, M., J. Delanoë, R. J. Hogan, N. L. Pounder, A. Protat, and J. Pelon (2013), From CloudSat-CALIPSO to EarthCare: Evolution of the DARDAR cloud classification and its comparison to airborne radar-lidar observations, *Journal of Geophysical Research: Atmospheres*, *118*(14), 7962–7981, doi:10.1002/jgrd.50579. 15, 16, 39, 41

Chan, K. M., and R. Wood (2013), The seasonal cycle of planetary boundary layer depth determined using COSMIC radio occultation data, *Journal of Geophysical Research Atmospheres*, *118*(22), 12,422–12,434, doi:10.1002/2013JD020147. 54

Chen, T., W. B. Rossow, and Y. Zhang (2000), Radiative Effects of Cloud-Type Variations, *Journal of Climate*, *13*, 264–286. 1, 4

Chen, Y. F., F. S. Yang, E. Su, and C. C. Ho (2019), Automatic Defect Detection System Based on Deep Convolutional Neural Networks, *roceedings of the 2019 International Conference on Engineering, Science, and Industrial Applications (ICESI), Tokyo, Japan, 22–24 August 2019*, doi:10.1109/ICESI.2019.8863029. 20

Clement, A. C., R. Burgman, and J. R. Norris (2009), Observational and model evidence for positive low-level cloud feedback, *Science*, *325*(5939), 460–464, doi:10.1126/science.1171255. 78, 87

Cober, S. G., and G. A. Isaac (2012), Characterization of aircraft icing environments with Supercooled Large Drops for application to commercial aircraft certification, *Journal of Applied Meteorology and Climatology*, *51*(2), 265–284, doi:10.1175/JAMC-D-11-022.1. 18

D'Alessandro, J. J., G. M. McFarquhar, W. Wu, J. L. Stith, J. B. Jensen, and R. M. Rauber (2021), Characterizing the Occurrence and Spatial Heterogeneity of Liquid, Ice, and Mixed Phase Low-Level Clouds Over the Southern Ocean Using in Situ Observations Acquired During SOCRATES, *Journal of Geophysical Research: Atmospheres*, *126*(11), doi:10.1029/2020JD034482. 37, 47, 94

Danker, J., O. Sourdeval, I. L. McCoy, R. Wood, and A. Possner (2022a), Exploring relations between cloud morphology, cloud phase, and cloud radiative properties in Southern Ocean's stratocumulus clouds, *Atmospheric Chemistry and Physics*, *22*(15), 10,247–10,265, doi:10.5194/acp-22-10247-2022. iii, 27

Danker, J., O. Sourdeval, I. L. McCoy, R. Wood, and A. Possner (2022b), Supplement of Exploring relations between cloud morphology, cloud phase, and cloud radiative properties in Southern Ocean's stratocumulus clouds, *Supplement of Atmos. Chem. Phys*, *22*, 10,247–10,265, doi:10.5194/acp-22-10247-2022-supplement. iii

David, R. O., C. Marcolli, J. Fahrni, Y. Qiu, Y. A. Perez Sirkin, V. Molinero, F. Mahrt, D. Brühwiler, U. Lohmann, and Z. A. Kanji (2019), Pore condensation and freezing is responsible for ice formation below water saturation for porous particles, *Proceedings of the National Academy of Sciences of the United States of America*, *116*(17), 8184–8189, doi:10.1073/PNAS.1813647116/-/DCSUPPLEMENTAL. 9

de Boer, G., E. W. Eloranta, and M. D. Shupe (2009), Arctic mixed-phase stratiform cloud properties from multiple years of surface-based measurements at two high-latitude locations, *Journal of the Atmospheric Sciences*, *66*(9), 2874–2887, doi:10.1175/2009JAS3029.1. 12

Delanoë, J., and R. J. Hogan (2008), A variational scheme for retrieving ice cloud properties from combined radar, lidar, and infrared radiometer, *Journal of Geophysical Research Atmospheres*, *113*(7), 1–21, doi:10.1029/2007JD009000. 39, 49

Delanoë, J., and R. J. Hogan (2010), Combined CloudSat-CALIPSO-MODIS retrievals of the properties of ice clouds, *Journal of Geophysical Research*, *115*(D4), D00H29, doi:10.1029/2009JD012346. 15, 41

DeMott, P. J., T. C. Hill, C. S. McCluskey, K. A. Prather, D. B. Collins, R. C. Sullivan, M. J. Ruppel, R. H. Mason, V. E. Irish, T. Lee, C. Y. Hwang, T. S. Rhee, J. R. Snider, G. R. McMeeking, S. Dhaniyala, E. R. Lewis, J. J. Wentzell, J. Abbatt, C. Lee, C. M. Sultana, A. P. Ault, J. L. Axson, M. D. Martinez, I. Venero, G. Santos-Figueroa, M. D. Stokes, G. B. Deane, O. L. Mayol-Bracero, V. H. Grassian, T. H. Bertram, A. K. Bertram, B. F. Moffett, and G. D. Franc (2016), Sea spray aerosol as a unique source of ice nucleating particles, *Proceedings of the National Academy of Sciences of the United States of America*, *113*(21), 5797–5803, doi:10.1073/pnas.1514034112. 44

Dhillon, A., and G. K. Verma (2020), Convolutional neural network: a review of models, methodologies and applications to object detection, *Progress in Artificial Intelligence*, *9*, 85–112, doi:10.1007/s13748-019-00203-0. 24

Díaz, J. P., F. J. Expósito, J. C. Pérez, A. González, Y. Wang, L. Haimberger, and J. Wang (2019), Long-term trends in marine boundary layer properties over the Atlantic Ocean, *Journal of Climate*, *32*(10), 2991–3004, doi:10.1175/JCLI-D-18-0219.1. 63, 78, 88

Digabel, H., and C. Lantuéjoul (1978), Iterative algorithms, *Proc. 2nd European Symp. Quantitative Analysis of Microstructures in Material Science, Biology and Medicine*, *19*, 8. 29

Driedonks, A. G., and P. G. Duynkerke (1989), Current problems in the stratocumulus-topped atmospheric boundary layer, *Boundary-Layer Meteorology*, *46*(3), 275–303, doi:10.1007/BF00120843/METRICS. 3

Dye, J. E., and P. V. Hobbs (1968), The Influence of Environmental Parameters on the Freezing and Fragmentation of Suspended Water Drops, *Journal of the Atmospheric Sciences*, *25*(1), 82–96, doi:10.1175/1520-0469(1968)025⟨0082:TIOEPO⟩2.0.CO;2. 10

D'Alessandro, J. J., M. Diao, C. Wu, X. Liu, J. B. Jensen, and B. B. Stephens (2019), Cloud Phase and Relative Humidity Distributions over the Southern Ocean in Austral Summer Based on In Situ Observations and CAM5 Simulations, *Journal of Climate*, *32*(10), 2781–2805, doi:10.1175/JCLI-D-18-0232.1. 12

Eastman, R., I. L. McCoy, and R. Wood (2021), Environmental and internal controls on Lagrangian transitions from closed cell mesoscale cellular convection over subtropical oceans, *Journal of the Atmospheric Sciences*, *78*(8), 2367–2383, doi:10.1175/JAS-D-20-0277.1. 2, 8, 18, 59, 61, 78, 80, 87

Eastman, R., I. L. McCoy, and R. Wood (2022), Wind, Rain, and the Closed to Open Cell Transition in Subtropical Marine Stratocumulus, *Journal of Geophysical Research: Atmospheres*, *127*(20), doi:10.1029/2022jd036795. 2, 8, 61, 71, 78, 80, 87

Eirund, G. K., U. Lohmann, and A. Possner (2019a), Cloud Ice Processes Enhance Spatial Scales of Organization in Arctic Stratocumulus, *Geophysical Research Letters*, *46*(23), 14,109–14,117, doi:10.1029/2019GL084959. 9, 12, 13, 48, 56, 61, 75, 76, 83, 84

Eirund, G. K., A. Possner, and U. Lohmann (2019b), Response of Arctic mixed-phase clouds to aerosol perturbations under different surface forcings, *Atmospheric Chemistry and Physics*, *19*(15), 9847–9864, doi:10.5194/acp-19-9847-2019. 50

Feingold, G., I. Koren, H. Wang, H. Xue, and W. A. Brewer (2010), Precipitation-generated oscillations in open cellular cloud fields, *Nature*, *466*(7308), 849–852, doi:10.1038/nature09314. 2, 8

Feingold, G., I. Koren, T. Yamaguchi, and J. Kazil (2015), On the reversibility of transitions between closed and open cellular convection, *Atmospheric Chemistry and Physics*, *15*(13), 7351–7367, doi:10.5194/acp-15-7351-2015. 8

Field, P. R., and A. J. Heymsfield (2015), Importance of snow to global precipitation, *Geophysical Research Letters*, *42*(21), 9512–9520, doi:10.1002/2015GL065497. 8

Findeisen, W. (1938), Die kolloidmeteorologischen Vorgänge bei der Niederschlagsbildung, *Meteorologische Zeitschrift*, pp. 121–133, doi:10.1127/METZ/2015/0675. 11

Fletcher, J., S. Mason, and C. Jakob (2016a), The Climatology, Meteorology, and Boundary Layer Structure of Marine Cold Air Outbreaks in Both Hemispheres*, *Journal of Climate*, *29*(6), 1999–2014, doi:10.1175/JCLI-D-15-0268.1. 2, 4, 7

Fletcher, J. K., S. Mason, and C. Jakob (2016b), A climatology of clouds in marine cold air outbreaks in both hemispheres, *Journal of Climate*, *29*(18), 6677–6692, doi:10.1175/JCLI-D-15-0783.1. 4, 8, 16

Freud, E., and D. Rosenfeld (2012), Linear relation between convective cloud drop number concentration and depth for rain initiation, *Journal of Geophysical Research: Atmospheres*, *117*(D2), doi:10.1029/2011JD016457. 18

Gayet, J.-F., S. Asano, A. Yamazaki, A. Uchiyama, A. Sinyuk, O. Jourdan, and F. Auriol (2002), Two case studies of winter continental-type water and mixed-phase stratocumuli over the sea 1. Microphysical and optical properties, *Journal of Geophysical Research: Atmospheres*, *107*(D21), doi:10.1029/2001JD001106. 16

Geerts, B., S. E. Giangrande, G. M. McFarquhar, L. Xue, S. J. Abel, J. M. Comstock, S. Crewell, P. J. DeMott, K. Ebell, P. Field, T. C. Hill, A. Hunzinger, M. P. Jensen, K. L. Johnson, T. W. Juliano, P. Kollias, B. Kosovic, C. Lackner, E. Luke, C. Lüpkes, A. A. Matthews, R. Neggers, M. Ovchinnikov, H. Powers, M. D. Shupe, T. Spengler, B. E. Swanson, M. Tjernström, A. K. Theisen, N. A. Wales, Y. Wang, M. Wendisch, and P. Wu (2022), The COMBLE Campaign: A Study of Marine Boundary Layer Clouds in Arctic Cold-Air Outbreaks, *Bulletin of the American Meteorological Society*, *103*(5), E1371–E1389, doi:10.1175/BAMS-D-21-0044.1. 2

Gettelman, A., and S. C. Sherwood (2016), Processes Responsible for Cloud Feedback, doi:10.1007/s40641-016-0052-8. 78, 87

Gettelman, A., C. Hannay, J. T. Bacmeister, R. B. Neale, A. G. Pendergrass, G. Danabasoglu, J. F. Lamarque, J. T. Fasullo, D. A. Bailey, D. M. Lawrence, and M. J. Mills (2019), High Climate Sensitivity in the Community Earth System Model Version 2 (CESM2), *Geophysical Research Letters*, *46*(14), 8329–8337, doi:10.1029/2019GL083978. 2, 13

Glassmeier, F., and G. Feingold (2017), Network approach to patterns in stratocumulus clouds, *Proceedings of the National Academy of Sciences*, *114*(40), 10,578–10,583, doi:10.1073/pnas.1706495114. 5, 6, 7, 49, 54, 55

Goren, T., and D. Rosenfeld (2012), Satellite observations of ship emission induced transitions from broken to closed cell marine stratocumulus over large areas, *Journal of Geophysical Research Atmospheres*, *117*(17), 17,206, doi:10.1029/2012JD017981. 8

Grady, L. (2006), Random walks for image segmentation, *IEEE Transactions on Pattern Analysis and Machine Intelligence*, *28*(11), 1768–1783, doi:10.1109/TPAMI.2006.233. 29

Gu, J., Z. Wang, J. Kuen, L. Ma, A. Shahroudy, B. Shuai, T. Liu, X. Wang, G. Wang, J. Cai, and T. Chen (2018), Recent advances in convolutional neural networks, *Pattern Recognition*, *77*, 354–377, doi:10.1016/J.PATCOG.2017.10.013. 23

Gufan, A., Y. Lehahn, E. Fredj, C. Price, R. Kurchin, and I. Koren (2016), Segmentation and Tracking of Marine Cellular Clouds observed by Geostationary Satellites, *International Journal of Remote Sensing*, *37*(5), 1055–1068, doi:10.1080/2150704X.2016.1142681. 29, 31

Hallett, J., and S. C. Mossop (1974), Production of secondary ice particles during the riming process, *Nature*, *249*(5452), 26–28, doi:10.1038/249026a0. 9, 42, 45

Han, Q., W. B. Rossow, and A. A. Lacis (1994), Near-Global Survey of Effective Droplet Radii in Liquid Water Clouds Using ISCCP Data, *Journal of Climate*, *7*(4), 465–497, doi:10.1175/1520-0442(1994)007⟨0465:NGSOED⟩2.0.CO;2. 27

Han, Q., R. Welch, J. Chou, W. Rossow, and A. White (1995), Validation of Satellite Retrievals of Cloud Microphysics and Liquid Water Path Using Observations from FIRE, *Journal of the Atmospheric Sciences*, *52*(23), 4183–4195, doi:10.1175/1520-0469(1995)052⟨4183:VOSROC⟩2.0.CO;2. 18

Hande, L. B., and C. Hoose (2017), Partitioning the primary ice formation modes in large eddy simulations of mixed-phase clouds, *Atmospheric Chemistry and Physics*, *17*(22), 14,105–14,118, doi:10.5194/acp-17-14105-2017. 9

Hartmann, D. L., and D. A. Short (1980), On the Use of Earth Radiation Budget Statistics for Studies of Clouds and Climate, *Journal of the Atmospheric Sciences*, *37*(6), 1233–1250, doi:10.1175/1520-0469(1980)037. 4

Hartmann, D. L., M. E. Ockert-Bell, and M. L. Michelsen (1992), The Effect of cloud type on earths energy budget: Global Analysis, *Journal of Climate*, *5*, 1281–1304, doi: https://doi.org/10.1175/1520-0442(1992)005⟨1281:TEOCTO⟩2.0.CO;2. 1, 4

Heikenfeld, M., B. White, L. Labbouz, and P. Stier (2019), Aerosol effects on deep convection: the propagation of aerosol perturbations through convective cloud microphysics, *Atmos. Chem. Phys*, *19*, 2601–2627, doi:10.5194/acp-19-2601-2019. 31

Helfand, H. M., and E. Kalnay (1983), A Model to Determine Open or Closed Cellular Convection, *Journal of the Atmospheric Sciences*, *40*(3), 631–650, doi:10.1175/1520-0469(1983)040⟨0631:amtdoo⟩2.0.co;2. 5, 7

Hu, Y., S. Rodier, K.-m. Xu, W. Sun, J. Huang, B. Lin, P. Zhai, and D. Josset (2010), Occurrence, liquid water content, and fraction of supercooled water clouds from combined CALIOP/IIR/MODIS measurements, *Journal of Geophysical Research*, *115*(19), D00H34, doi:10.1029/2009JD012384. 37

Huang, S., W. Hu, J. Chen, Z. Wu, D. Zhang, and P. Fu (2021a), Overview of biological ice nucleating particles in the atmosphere, *Environment International*, *146*, 106,197, doi:10.1016/j.envint.2020.106197. 44

Huang, Y., S. T. Siems, M. J. Manton, A. Protat, and J. Delanoë (2012), A study on the low-altitude clouds over the Southern Ocean using the DARDAR-MASK, *Journal of Geophysical Research Atmospheres*, *117*(17), 1–15, doi:10.1029/2012JD017800. 37, 39

Huang, Y., T. H. Chubb, D. Baumgardner, M. DeHoog, S. T. Siems, and M. J. Manton (2017), Evidence for secondary ice production in Southern Ocean open cellular convection, *Quarterly Journal of the Royal Meteorological Society*, *143*(704), 1685–1703, doi:10.1002/qj.3041. 8, 17, 37, 75, 84

Huang, Y., S. T. Siems, and M. J. Manton (2021b), Wintertime In Situ Cloud Microphysical Properties of Mixed-Phase Clouds Over the Southern Ocean, *Journal of Geophysical Research: Atmospheres*, *126*(11), doi:10.1029/2021JD034832. 15

Janssens, M., J. Vilà-Guerau de Arellano, M. Scheffer, C. Antonissen, A. P. Siebesma, and F. Glassmeier (2021), Cloud Patterns in the Trades Have Four Interpretable Dimensions, *Geophysical Research Letters*, *48*(5), doi:10.1029/2020GL091001. 31

Jensen, M. P., V. P. Ghate, D. Wang, D. K. Apoznanski, M. J. Bartholomew, S. E. Giangrande, K. L. Johnson, and M. M. Thieman (2021), Contrasting characteristics of

open- and closed-cellular stratocumulus cloud in the eastern North Atlantic, *Atmospheric Chemistry and Physics*, *21*(19), 14,557–14,571, doi:10.5194/acp-21-14557-2021. 6, 8, 49, 54, 55

Kay, J. E., and A. Gettelman (2009), Cloud influence on and response to seasonal Arctic sea ice loss, *Journal of Geophysical Research*, *114*(D18), D18,204, doi:10.1029/2009JD011773. 17

Keeler, J. M., B. F. Jewett, R. M. Rauber, G. M. McFarquhar, R. M. Rasmussen, L. Xue, C. Liu, and G. Thompson (2016), Dynamics of cloud-top generating cells in winter cyclones. Part I: Idealized simulations in the context of field observations, *Journal of the Atmospheric Sciences*, *73*(4), 1507–1527, doi:10.1175/JAS-D-15-0126.1. 50

Khanal, S., and Z. Wang (2018), Uncertainties in MODIS-Based Cloud Liquid Water Path Retrievals at High Latitudes Due to Mixed-Phase Clouds and Cloud Top Height Inhomogeneity, *Journal of Geophysical Research: Atmospheres*, *123*(19), 154–11, doi:10.1029/2018JD028558. 27, 51

Kiela, D., and L. Bottou (2014), Learning Image Embeddings using Convolutional Neural Networks for Improved Multi-Modal Semantics, in *Proceedings of the 2014 Conference on empirical methods in natural language processing (EMNLP)*, pp. 36–45. 20

Klein, S. A., and D. L. Hartmann (1993), The Seasonal Cycle of Low Stratiform Clouds, *Journal of Climate*, *6*(8), 1587–1606, doi:10.1175/1520-0442(1993)006⟨1587:TSCOLS⟩2.0.CO;2. 4, 5, 68, 69

Kolstad, E. W., and T. J. Bracegirdle (2008), Marine cold-air outbreaks in the future: An assessment of IPCC AR4 model results for the Northern Hemisphere, *Climate Dynamics*, *30*(7-8), 871–885, doi:10.1007/s00382-007-0331-0. 78, 87

Korolev, A., and G. Isaac (2003), Phase transformation of mixed-phase clouds, *Meteorol. Soc*, *129*, 19–38, doi:10.1256/qj.01.203. 12

Korolev, A., and J. Milbrandt (2022), How Are Mixed-Phase Clouds Mixed?, *Geophysical Research Letters*, *49*(18), doi:10.1029/2022GL099578. 12

Korolev, A., I. Heckman, M. Wolde, A. S. Ackerman, A. M. Fridlind, L. A. Ladino, R. Paul Lawson, J. Milbrandt, and E. Williams (2020), A new look at the environmental conditions favorable to secondary ice production, *Atmospheric Chemistry and Physics*, *20*(3), 1391–1429, doi:10.5194/ACP-20-1391-2020. 10

Korolev, A. V., and T. Leisner (2020), Review of experimental studies on secondary ice production, *Atmospheric Chemistry and Physics Discussions*, *20*(June), 1–42, doi:10.5194/acp-20-11767-2020. 9, 11

Korolev, A. V., M. P. Bailey, J. Hallett, and G. A. Isaac (2004), Laboratory and In Situ Observation of Deposition Growth of Frozen Drops, *Journal of Applied Meteorology*, *43*(4), 612–622, doi:10.1175/1520-0450(2004)043⟨0612:LAISOO⟩2.0.CO;2. 10

Korolev, A. V., G. M. McFarquhar, P. R. Field, C. N. Franklin, P. Lawson, Z. Wang, E. Williams, S. J. Abel, D. Axisa, S. Borrmann, J. Crosier, J. Fugal, M. Krämer, U. Lohmann, O. Schlenczek, M. Schnaiter, and M. Wendisch (2017), Mixed-Phase Clouds: Progress and Challenges, *Meteorological Monographs*, *58*, 1–5, doi:10.1175/amsmonographs-d-17-0001.1. 2, 9, 11, 12

Krizhevsky, A., I. Sutskever, and G. E. Hinton (2012), ImageNet classification with deep convolutional neural networks, *Proceedings of the 25th International Conference on Neu-ral Information Processing Systems (Lake Tahoe, NV, Dec. 2012)*, pp. 1097–1105, doi:10.1145/3065386. 20

Krueger, A. F., and S. Fritz (1961), Cellular Cloud Patterns revealed by Tiros I, *Tellus*, *13*(1), 1–7, doi:10.1111/j.2153-3490.1961.tb00061.x. 5

Lang, F., Y. Huang, S. T. Siems, and M. J. Manton (2018), Characteristics of the Marine Atmospheric Boundary Layer Over the Southern Ocean in Response to the Synoptic Forcing, *Journal of Geophysical Research: Atmospheres*, *123*(15), 7799–7820, doi:10.1029/2018JD028700. 54

Lang, F., Y. Huang, A. Protat, S. C. H. Truong, S. T. Siems, and M. J. Manton (2021), Shallow Convection and Precipitation Over the Southern Ocean: A Case Study During the CAPRICORN 2016 Field Campaign, *Journal of Geophysical Research: Atmospheres*, *126*(9), doi:10.1029/2020JD034088. 8, 37, 75, 84

Lang, F., L. Ackermann, Y. Huang, S. C. H. Truong, S. T. Siems, and M. J. Manton (2022), A climatology of open and closed mesoscale cellular convection over the Southern Ocean derived from Himawari-8 observations, *Atmospheric Chemistry and Physics*, *22*(3), 2135–2152, doi:10.5194/acp-22-2135-2022. 19, 50, 68, 71, 73, 77, 86

Lang, F., S. T. Siems, Y. Huang, and L. Ackermann (2023), On the relationship between mesoscale cellular convection and meteorological forcing: Comparing the Southern Ocean against the North Pacific, *EGUsphere [preprint]*, doi:10.5194/egusphere-2023-518. 68, 71, 73, 77, 86

LeCun, Y., Y. Bengio, and G. Hinton (2015), Deep learning, doi:10.1038/nature14539. 19, 22

LeNail, A. (2019), NN-SVG: Publication-Ready Neural Network Architecture Schematics, *Journal of Open Source Software*, *4*(33), 747, doi:10.21105/JOSS.00747. 23

Leon, D. C., Z. Wang, and D. Liu (2008), Climatology of drizzle in marine boundary layer clouds based on 1 year of data from CloudSat and Cloud-Aerosol Lidar and Infrared Pathfinder Satellite Observations (CALIPSO), *Journal of Geophysical Research Atmospheres*, *114*(8), 0–14, doi:10.1029/2008JD009835. 3

Libbrecht, K. G. (2005), The physics of snow crystals, *Reports on Progress in Physics*, *68*(4), 855–895, doi:10.1088/0034-4885/68/4/R03. 11, 42, 46

Lilly, D. K. (1968), Models of cloud-topped mixed layers under a strong inversion, *Quarterly Journal of the Royal Meteorological Society*, *94*(401), 292–309, doi:10.1002/QJ.49709440106. 3

Liou, K. N. (1992), *Oxford Monographs on Geology and Geophysics: Theory, Observation and Modeling*, Oxford University Press. 4

Listowski, C., J. Delanoë, A. Kirchgaessner, T. Lachlan-Cope, and J. King (2019), Antarctic clouds, supercooled liquid water and mixed phase, investigated with DARDAR: Geographical and seasonal variations, *Atmospheric Chemistry and Physics*, *19*(10), 6771–6808, doi:10.5194/acp-19-6771-2019. 15, 17, 41, 42

Liu, Y., J. R. Key, S. A. Ackerman, G. G. Mace, and Q. Zhang (2012), Arctic cloud macrophysical characteristics from CloudSat and CALIPSO, *Remote Sensing of Environment*, *124*, 159–173, doi:10.1016/j.rse.2012.05.006. 16

Lock, A. P. (2009), Factors influencing cloud area at the capping inversion for shallow cumulus clouds, *Quarterly Journal of the Royal Meteorological Society*, *135*(641), 941–952, doi:10.1002/QJ.424. 3

Loeb, N. G., B. A. Wielicki, F. G. Rose, and D. R. Doelling (2007), Variability in global top-of-atmosphere shortwave radiation between 2000 and 2005, *Geophysical Research Letters*, *34*(3), L03,704, doi:10.1029/2006GL028196. 51

Lohmann, U., F. Lüönd, and F. Mahrt (2016), *An Introduction to Clouds*, 1–391 pp., Cambridge University Press, doi:10.1017/CBO9781139087513. 1, 9, 10

Mace, G. G., and A. Protat (2018), Clouds over the Southern Ocean as observed from the R/V investigator during CAPRICORN. Part I: Cloud occurrence and phase partitioning, *Journal of Applied Meteorology and Climatology*, *57*(8), 1783–1803, doi: 10.1175/JAMC-D-17-0194.1. 17

Mace, G. G., A. Protat, and S. Benson (2021), Mixed-Phase Clouds Over the Southern Ocean as Observed From Satellite and Surface Based Lidar and Radar, *Journal of Geophysical Research: Atmospheres*, *126*(16), doi:10.1029/2021JD034569. 37, 39

Magono, C. (1962), The Temperature Conditions for the Growth of Natural and Artificial Snow Crystals, *Journal of the Meteorological Society of Japan*, *40*(4), 185–192, doi: 10.2151/jmsj1923.40.4_185. 42, 46

Marchand, R., G. G. Mace, T. Ackerman, and G. L. Stephens (2008), Hydrometeor detection using Cloudsat - An earth-orbiting 94-GHz cloud radar, *Journal of Atmospheric and Oceanic Technology*, *25*(4), 519–533, doi:10.1175/2007JTECHA1006.1. 16, 39

Marcolli, C. (2014), Atmospheric Chemistry and Physics Deposition nucleation viewed as homogeneous or immersion freezing in pores and cavities, *Atmos. Chem. Phys*, *14*, 2071–2104, doi:10.5194/acp-14-2071-2014. 9

Marcolli, C., F. Mahrt, and B. Kärcher (2021), Soot PCF: Pore condensation and freezing framework for soot aggregates, *Atmospheric Chemistry and Physics*, *21*(10), 7791–7843, doi:10.5194/ACP-21-7791-2021. 9

Martini, M. N., W. I. Gustafson, Q. Yang, and H. Xiao (2014), Impact of resolution on simulation of closed mesoscale cellular convection identified by dynamically guided watershed segmentation, *Journal of Geophysical Research Atmospheres*, *119*(22), 674–12, doi:10.1002/2014JD021962. 29, 31, 83

Mason, S., C. Jakob, A. Protat, and J. Delanoë (2014), Characterizing observed midtopped cloud regimes associated with Southern Ocean shortwave radiation biases, *Journal of Climate*, *27*(16), 6189–6203, doi:10.1175/JCLI-D-14-00139.1. 41

Matus, A. V., and T. S. L'Ecuyer (2017), The role of cloud phase in Earth's radiation budget, *Journal of Geophysical Research*, *122*(5), 2559–2578, doi:10.1002/2016JD025951. 2, 12

McCluskey, C. S., T. C. Hill, R. S. Humphries, A. M. Rauker, S. Moreau, P. G. Strutton, S. D. Chambers, A. G. Williams, I. McRobert, J. Ward, M. D. Keywood, J. Harnwell, W. Ponsonby, Z. M. Loh, P. B. Krummel, A. Protat, S. M. Kreidenweis, and P. J.

DeMott (2018), Observations of Ice Nucleating Particles Over Southern Ocean Waters, *Geophysical Research Letters*, *45*(21), 989–11, doi:10.1029/2018GL079981. 9

McCluskey, C. S., P. J. DeMott, P. L. Ma, and S. M. Burrows (2019), Numerical Representations of Marine Ice-Nucleating Particles in Remote Marine Environments Evaluated Against Observations, *Geophysical Research Letters*, *46*(13), 7838–7847, doi:10.1029/2018GL081861. 44, 45

McCoy, D. T., D. L. Hartmann, and D. P. Grosvenor (2014a), Observed Southern Ocean cloud properties and shortwave reflection. Part I: Calculation of SW flux from observed cloud properties, *Journal of Climate*, *27*(23), 8836–8857, doi:10.1175/JCLI-D-14-00287.1. 51

McCoy, D. T., D. L. Hartmann, and D. P. Grosvenor (2014b), Observed Southern Ocean cloud properties and shortwave reflection. Part II: Phase changes and low cloud feedback, *Journal of Climate*, *27*(23), 8858–8868, doi:10.1175/JCLI-D-14-00288.1. 51

McCoy, D. T., D. L. Hartmann, M. D. Zelinka, P. Ceppi, and D. P. Grosvenor (2015), Mixed-phase cloud physics and Southern Ocean cloud feedback in climate models, *Journal of Geophysical Research*, *120*(18), 9539–9554, doi:10.1002/2015JD023603. 2, 12

McCoy, I. L., R. Wood, and J. K. Fletcher (2017), Identifying Meteorological Controls on Open and Closed Mesoscale Cellular Convection Associated with Marine Cold Air Outbreaks, *Journal of Geophysical Research: Atmospheres*, *122*(21), 678–11, doi:10.1002/2017JD027031. 1, 2, 4, 7, 8, 41, 42, 50, 51, 59, 61, 62, 68, 70, 71, 72, 73, 76, 77, 78, 83, 85, 86, 87, 95

McCoy, I. L., D. T. McCoy, R. Wood, P. Zuidema, and F. A. Bender (2023), The Role of Mesoscale Cloud Morphology in the Shortwave Cloud Feedback, *Geophysical Research Letters*, *50*(2), doi:10.1029/2022GL101042. 2, 8, 62

McFarquhar, G. M., and S. G. Cober (2004), Single-scattering properties of mixed-phase Arctic clouds at solar wavelengths: Impacts on radiative transfer, *Journal of Climate*, *17*(19), 3799–3813, doi:10.1175/1520-0442(2004)017⟨3799:SPOMAC⟩2.0.CO;2. 16

McFarquhar, G. M., et al. (2021), Observations of Clouds, Aerosols, Precipitation, and Surface Radiation over the Southern Ocean: An Overview of CAPRICORN, MARCUS, MICRE, and SOCRATES, *Bulletin of the American Meteorological Society*, *102*(4), E894–E928, doi:10.1175/BAMS-D-20-0132.1. 37

Mellado, J. P. (2017), Cloud-Top Entrainment in Stratocumulus Clouds, *Annual Review of Fluid Mechanics*, *49*(1), 145–169, doi:10.1146/annurev-fluid-010816-060231. 3, 79

Menzel, W. P., R. A. Frey, and B. A. Baum (2010), Cloud Top Properties and Cloud Phase Algorithm Theoretical Basis Document, *Tech. Rep. October*, Cooperative Institute for Meteorological Satellite Studies, University of Wisconsin - Madison, Madison. 20, 36

Mignani, C., J. M. Creamean, L. Zimmermann, C. Alewell, and F. Conen (2019), New type of evidence for secondary ice formation at around -15 °C in mixed-phase clouds, *Atmospheric Chemistry and Physics*, *19*(2), 877–886, doi:10.5194/acp-19-877-2019. 10, 11, 41, 42, 46

Miller, S. D., Y.-J. Noh, and A. K. Heidinger (2014), Liquid-top mixed-phase cloud detection from shortwave-infrared satellite radiometer observations: A physical basis, *Journal of Geophysical Research*, *119*(13), 8245–8267, doi:10.1002/2013JD021262. 27

Mioche, G., O. Jourdan, M. Ceccaldi, and J. Delanoë (2015), Variability of mixed-phase clouds in the Arctic with a focus on the Svalbard region: A study based on spaceborne active remote sensing, *Atmospheric Chemistry and Physics*, *15*(5), 2445–2461, doi:10.5194/acp-15-2445-2015. 16

Moen, E., D. Bannon, T. Kudo, W. Graf, M. Covert, and D. Van Valen (2019), Deep learning for cellular image analysis, *Nature Methods*, *16*(12), 1233–1246, doi:10.1038/s41592-019-0403-1. 24

Moeng, C.-H., S. Shen, and D. A. Randall (1992), Physical Processes within the Nocturnal Stratus-topped Boundary Layer, *Journal of the Atmospheric Sciences*, *49*(24), 2384–2401, doi:10.1175/1520-0469(1992)049⟨2384:PPWTNS⟩2.0.CO;2. 3

Moeng, C.-H., W. R. Cotton, B. Stevens, C. Bretherton, H. A. Rand, A. Chlond, M. Khairoutdinov, S. Krueger, W. S. Lewellen, M. K. MacVean, J. R. M. Pasquier, A. P. Siebesma, and R. I. Sykes (1996), Simulation of a Stratocumulus-Topped Planetary Boundary Layer: Intercomparison among Different Numerical Codes, *Bulletin of the American Meteorological Society*, *77*(2), 261–278, doi:10.1175/1520-0477(1996)077⟨0261:SOASTP⟩2.0.CO;2. 3

Mohrmann, J. K. C., R. Wood, T. Yuan, H. Song, R. Eastman, and L. Oreopoulos (2021), Identifying meteorological influences on marine low-cloud mesoscale morphology using satellite classifications, *Atmospheric Chemistry and Physics*, *21*(12), 9629–9642, doi:10.5194/acp-21-9629-2021. 59, 68, 69, 70, 71, 72, 73, 77, 86

Morrison, A. E., S. T. Siems, and M. J. Manton (2011), A three-year climatology of cloud-top phase over the Southern Ocean and North Pacific, *Journal of Climate*, *24*(9), 2405–2418, doi:10.1175/2010JCLI3842.1. 12, 37, 41

Morrison, A. L., J. E. Kay, H. Chepfer, R. Guzman, and V. Yettella (2018), Isolating the Liquid Cloud Response to Recent Arctic Sea Ice Variability Using Spaceborne Lidar Observations, *Journal of Geophysical Research: Atmospheres*, *123*(1), 473–490, doi:10.1002/2017JD027248. 42

Morrison, H., J. A. Curry, and V. I. Khvorostyanov (2005), A New Double-Moment Microphysics Parameterization for Application in Cloud and Climate Models. Part I: Description, *Journal of the Atmospheric Sciences*, *62*(6), 1665–1677, doi:10.1175/JAS3446.1. 12

Morrison, H., G. De Boer, G. Feingold, J. Y. Harrington, M. D. Shupe, and K. Sulia (2012), Resilience of persistent Arctic mixed-phase clouds, doi:10.1038/ngeo1332. 3, 12

Muchnik, V. M., and J. S. Rudko (1961), Peculiarities of freezing supercooled water drops, *Trudy Ukrainsk Hydro Meteorological Institute*, *26*, 64–73. 10

Muhlbauer, A., I. L. McCoy, and R. Wood (2014), Climatology of stratocumulus cloud morphologies: microphysical properties and radiative effects, *Atmospheric Chemistry and Physics*, *14*(13), 6695–6716, doi:10.5194/acp-14-6695-2014. 7, 8, 19, 21, 41, 49, 51, 59, 61, 68, 69, 70, 71, 72, 73, 77, 83, 86

Mülmenstädt, J., O. Sourdeval, J. Delanoë, and J. Quaas (2015), Frequency of occurrence of rain from liquid-, mixed-, and ice-phase clouds derived from A-Train satellite retrievals, *Geophysical Research Letters*, *42*(15), 6502–6509, doi:10.1002/2015GL064604. 12, 39

Mülmenstädt, J., M. Salzmann, J. E. Kay, M. D. Zelinka, P. L. Ma, C. Nam, J. Kretzschmar, S. Hörnig, and J. Quaas (2021), An underestimated negative cloud feedback from cloud lifetime changes, *Nature Climate Change*, *11*(6), 508–513, doi:10.1038/s41558-021-01038-1. 78, 87

Murray, B. J., K. S. Carslaw, and P. R. Field (2021), Opinion: Cloud-phase climate feedback and the importance of ice-nucleating particles, *Atmospheric Chemistry and Physics*, *21*(2), 665–679, doi:10.5194/acp-21-665-2021. 78, 87, 88

Myers, T. A., and J. R. Norris (2016), Reducing the uncertainty in subtropical cloud feedback, *Geophysical Research Letters*, *43*(5), 2144–2148, doi:10.1002/2015GL067416. 78, 87

Myers, T. A., R. C. Scott, M. D. Zelinka, S. A. Klein, J. R. Norris, and P. M. Caldwell (2021), Observational constraints on low cloud feedback reduce uncertainty of climate

sensitivity, *Nature Climate Change*, *11*(6), 501–507, doi:10.1038/s41558-021-01039-0. 78, 87

Nakajima, T., and M. D. King (1990), Determination of the Optical Thickness and Effective Particle Radius of Clouds from Reflected Solar Radiation Measurements. Part I: Theory, *Journal of the Atmospheric Sciences*, *47*(15), 1878–1893, doi:10.1175/1520-0469(1990)047⟨1878:DOTOTA⟩2.0.CO;2. 27

Niu, J., L. D. Carey, P. Yang, and T. H. Vonder Haar (2008), Optical properties of a vertically inhomogeneous mid-latitude mid-level mixed-phase altocumulus in the infrared region, *Atmospheric Research*, *88*(3-4), 234–242, doi:10.1016/j.atmosres.2007.11.020. 37

Noh, Y.-J., S. D. Miller, A. K. Heidinger, G. G. Mace, A. Protat, and S. P. Alexander (2019), Satellite-Based Detection of Daytime Supercooled Liquid-Topped Mixed-Phase Clouds Over the Southern Ocean Using the Advanced Himawari Imager, *Journal of Geophysical Research: Atmospheres*, *124*(5), 2677–2701, doi:10.1029/2018JD029524. 17

Norris, J. R. (1998), Low Cloud Type over the Ocean from Surface Observations. Part I: Relationship to Surface Meteorology and the Vertical Distribution of Temperature and Moisture., *Journal of Climate*, *11*(3), 369–382, doi:10.1175/1520-0442(1998)011. 4

Norris, J. R., and S. A. Klein (2000), Low Cloud Type over the Ocean from Surface Observations. Part III: Relationship to Vertical Motion and the Regional Surface Synoptic Environment., *Journal of Climate*, *13*(1), 245–256, doi:10.1175/1520-0442(2000)013. 4

Norris, J. R., R. J. Allen, A. T. Evan, M. D. Zelinka, C. W. O'Dell, and S. A. Klein (2016), Evidence for climate change in the satellite cloud record, *Nature 2016 536:7614*, *536*(7614), 72–75, doi:10.1038/nature18273. 78, 87

Noteboom, S. (2007), Open Cell Convection and Closed Cell Convection, *Tech. rep.*, Wageningen Universiteit, De Bilt, Netherlads. 7

Oraltay, R. G., and J. Hallett (1989), Evaporation and melting of ice crystals: A laboratory study, *Atmospheric Research*, *24*(1-4), 169–189, doi:10.1016/0169-8095(89)90044-6. 10

Pang, B., E. Nijkamp, and Y. N. Wu (2020), Deep Learning With TensorFlow: A Review, *Journal of Educational and Behavioral Statistics*, *45*(2), 227–248, doi:10.3102/1076998619872761/FORMAT/EPUB. 22, 26, 81

Parvati, K., B. S. Prakasa Rao, and M. Mariya Das (2008), Image segmentation using gray-scale morphology and marker-controlled watershed transformation, *Discrete Dynamics in Nature and Society*, *2008*, doi:10.1155/2008/384346. 29

Perez, L., and J. Wang (2017), The Effectiveness of Data Augmentation in Image Classification using Deep Learning, *Convolutional Neural Networks Vis. Recognit.* 25

Platnick, S., and S. Twomey (1994), Determining the Susceptibility of Cloud Albedo to Changes in Droplet Concentration with the Advanced Very High Resolution Radiometer, *Journal of Applied Meteorology*, *33*(3), 334–347, doi:10.1175/1520-0450(1994)033⟨0334:DTSOCA⟩2.0.CO;2. 16

Platnick, S., M. D. King, S. A. Ackerman, W. P. Menzel, B. A. Baum, J. C. Riedi, and R. A. Frey (2003), The MODIS cloud products: Algorithms and examples from terra, *IEEE Transactions on Geoscience and Remote Sensing*, *41*(2 PART 1), 459–472, doi:10.1109/TGRS.2002.808301. 27

Platnick, S., P. A. Hubanks, K. G. Meyer, and M. D. King (2015), MODIS Atmosphere L3 Monthly Product. NASA MODIS Adaptive Processing System, *Goddard Space Flight Center, USA*, doi:http://dx.doi.org/10.5067/MODIS/MOD08_M3.006. 15, 19, 26, 36, 76, 85

Platnick, S., K. G. Meyer, M. D. King, G. Wind, N. Amarasinghe, B. Marchant, G. T. Arnold, Z. Zhang, P. A. Hubanks, R. E. Holz, P. Yang, W. L. Ridgway, and J. C. Riedi (2017), The MODIS cloud optical and microphysical products: Collection 6 updates and examples from Terra and Aqua, *IEEE Trans Geosci Remote Sens*, *55*(1), 502–525, doi:10.1109/TGRS.2016.2610522. 27

Pruppacher, H. R., J. D. Klett, and P. K. Wang (1998), Microphysics of clouds and precipitation. 9

Qu, X., A. Hall, S. A. Klein, and A. M. Deangelis (2015), Positive tropical marine low-cloud cover feedback inferred from cloud-controlling factors, *Geophysical Research Letters*, *42*(18), 7767–7775, doi:10.1002/2015GL065627. 78, 87

Raasch, S., and M. Schröter (2001), Broadening of Convective Cells During Cold Air Outbreaks: A Numerical Study Using a Parallelized Large-Eddy Simulation Model, in *NIC Symposium*, vol. 9, edited by H. Rollnik and D. Wolf, pp. 433–441. 71

Ramanathan, V., D. Cess, E. F. Harrison, P. Minnis, B. R. Barkstrom, E. Ahmad, and D. L. Hartmann (1989), Cloud-radiative forcing and climate: Results from the earth radiation budget experiment, *Science*, *243*(4887), 57–63, doi:DOI:10.1126/science.243.4887.57. 1, 4

Randall, D. A., and M. J. Suarez (1984), On the Dynamics of Stratocumulus Formation and Dissipation, *Journal of the Atmospheric Sciences*, *41*(20), 3052–3057, doi:10.1175/1520-0469(1984)041. 5

Randall, D. A., J. A. Coakley, C. W. Fairall, R. A. Kropfli, and D. H. Lenschow (1984), Outlook for Research on Subtropical, *American Meteorological Society*, *65*(12), 1290–1301. 1, 3, 4, 5

Rangno, A. L. (2008), Fragmentation of freezing drops in shallow maritime frontal clouds, *Journal of the Atmospheric Sciences*, *65*(4), 1455–1466, doi:10.1175/2007JAS2295.1. 10

Rangno, A. L., and P. V. Hobbs (2005), Microstructures and precipitation development in cumulus and small cumulonimbus clouds over the warm pool of the tropical Pacific Ocean, *Quarterly Journal of the Royal Meteorological Society*, *131*(606), 639–673, doi:10.1256/qj.04.13. 18

Reichel, C. (2022), *Identifying open and closed stratocumulus clouds by their reflectance using a convolutional neural network (M.Sc. thesis)*, 0 -90 pp., Johann-Wolfgang Goethe University Frankfurt, Frankfurt am Main. 19, 21, 22, 24, 25, 65, 67, 77, 86

Riley, E. M., and B. E. Mapes (2009), Unexpected peak near -15 °C in CloudSat echo top climatology, *Geophysical Research Letters*, *36*(9), L09,819, doi:10.1029/2009GL037558. 10, 41

Rosenfeld, D., Y. J. Kaufman, and I. Koren (2006), Switching cloud cover and dynamical regimes from open to closed Benard cells in response to the suppression of precipitation by aerosols, *Atmospheric Chemistry and Physics*, *6*(9), 2503–2511, doi:10.5194/acp-6-2503-2006. 8

Rosenfeld, D., H. Wang, and P. J. Rasch (2012), The roles of cloud drop effective radius and LWP in determining rain properties in marine stratocumulus, *Geophysical Research Letters*, *39*(13), n/a–n/a, doi:10.1029/2012GL052028. 18

Said, K. A. M., A. B. Jambek, and N. Sulaiman (2016), A study of image processing using morphological opening and closing processes, *International Journal of Control Theory and Applications*, *9*(31), 15–21. 31

Schaefer, V. J. (1946), The Production of Ice Crystals in a Cloud of Supercooled Water Droplets, *Science*, *104*(2707), 457–459, doi:10.1126/science.104.2707.457. 9

Schuddeboom, A. J., and A. J. McDonald (2021), The Southern Ocean Radiative Bias, Cloud Compensating Errors, and Equilibrium Climate Sensitivity in CMIP6 Models,

Journal of Geophysical Research: Atmospheres, *126*(22), doi:10.1029/2021JD035310. 77, 87

Sedlar, J., and M. Tjernström (2009), Stratiform cloud - Inversion characterization during the arctic melt season, *Boundary-Layer Meteorology*, *132*(3), 455–474, doi:10.1007/S10546-009-9407-1/METRICS. 3

Seinfeld, J. H., and S. N. Pandis (2006), *Atmospheric chemistry and physics : from air pollution to climate change*, 2nd ed., John Wiley & Sons, Hoboken, New Jersey. 9

Shcherbakov, V., J. F. Gayet, O. Jourdan, A. Minikin, J. Ström, and A. Petzold (2005), Assessment of cirrus cloud optical and microphysical data reliability by applying statistical procedures, *Journal of Atmospheric and Oceanic Technology*, *22*(4), 409–420, doi:10.1175/JTECH1710.1. 16

Shupe, M. D., and J. M. Intrieri (2004), Cloud radiative forcing of the Arctic surface: The influence of cloud properties, surface albedo, and solar zenith angle, *Journal of Climate*, *17*(3), 616–628, doi:10.1175/1520-0442(2004)017⟨0616:CRFOTA⟩2.0.CO;2. 12

Shupe, M. D., P. Kollias, S. Y. Matrosov, and T. L. Schneider (2004), Deriving Mixed-Phase Cloud Properties from Doppler Radar Spectra, *Journal of Atmospheric and Oceanic Technology*, *21*(4), 660–670, doi:10.1175/1520-0426(2004)021⟨0660:DMCPFD⟩2.0.CO;2. 12

Shupe, M. D., S. Y. Matrosov, and T. Uttal (2006), Arctic mixed-phase cloud properties derived from surface-based sensors at SHEBA, *Journal of the Atmospheric Sciences*, *63*(2), 697–711, doi:10.1175/JAS3659.1. 12, 51

Shupe, M. D., J. S. Daniel, G. de Boer, E. W. Eloranta, P. Kollias, C. N. Long, E. P. Luke, D. D. Turner, and J. Verlinde (2008), A focus on mixed-phase clouds, *Bulletin of the American Meteorological Society*, *89*(10), 1549–1562, doi:10.1175/2008BAMS2378.1. 9, 12, 37

Silber, I., A. M. Fridlind, J. Verlinde, A. S. Ackerman, Y. S. Chen, D. H. Bromwich, S. H. Wang, M. Cadeddu, and E. W. Eloranta (2019), Persistent Supercooled Drizzle at Temperatures Below -25 °C Observed at McMurdo Station, Antarctica, *Journal of Geophysical Research: Atmospheres*, *124*(20), 10,878–10,895, doi:10.1029/2019JD030882. 17

Silber, I., P. S. McGlynn, J. Y. Harrington, and J. Verlinde (2021a), Habit-Dependent Vapor Growth Modulates Arctic Supercooled Water Occurrence, *Geophysical Research Letters*, *48*(10), doi:10.1029/2021GL092767. 11, 42, 43, 45, 46

Silber, I., A. M. Fridlind, J. Verlinde, A. S. Ackerman, G. V. Cesana, and D. A. Knopf (2021b), The prevalence of precipitation from polar supercooled clouds, *Atmospheric Chemistry and Physics*, *21*(5), 3949–3971, doi:10.5194/acp-21-3949-2021. 43

Simonyan, K., and A. Zisserman (2015), Very Deep Convolutional Networks for Large-Scale Image Recognition, in *Published as a conference paper at International Conference on Learning Representations (ICLR) 2015*. 20

Soekhoe, D., P. van der Putten, and A. Plaat (2016), On the impact of data set size in transfer learning using deep neural networks, in *Lecture Notes in Computer Science (including subseries Lecture Notes in Artificial Intelligence and Lecture Notes in Bioinformatics)*, vol. 9897 LNCS, pp. 50–60, Springer Verlag, doi:10.1007/978-3-319-46349-0_5. 25

Solomon, A., M. D. Shupe, P. O. Persson, and H. Morrison (2011), Moisture and dynamical interactions maintaining decoupled Arctic mixed-phase stratocumulus in the presence of a humidity inversion, *Atmospheric Chemistry and Physics*, *11*(19), 10,127–10,148, doi:10.5194/ACP-11-10127-2011. 3

Stephens, G. L., D. M. Winker, J. Pelon, C. Trepte, D. G. Vane, C. Yuhas, T. S. L'Ecuyer, and M. Lebsock (2018), Cloudsat and calipso within the a-train: Ten years of actively observing the earth system, *Bulletin of the American Meteorological Society*, *99*(3), 569–581, doi:10.1175/BAMS-D-16-0324.1. 27

Stevens, R. G., K. Loewe, C. Dearden, A. Dimitrelos, A. Possner, G. K. Eirund, T. Raatikainen, A. A. Hill, B. J. Shipway, J. M. Wilkinson, S. Romakkaniemi, J. Tonttila, A. Laaksonen, H. Korhonen, P. J. Connolly, U. Lohmann, C. Hoose, A. M. Ekman, K. S. Carslaw, and P. R. Field (2018), A model intercomparison of CCN-limited tenuous clouds in the high Arctic, *Atmospheric Chemistry and Physics*, *18*(15), 11,041–11,071, doi:10.5194/acp-18-11041-2018. 12

Storelvmo, T., I. Tan, and A. V. Korolev (2015), Cloud Phase Changes Induced by CO2 Warming—a Powerful yet Poorly Constrained Cloud-Climate Feedback, doi:10.1007/s40641-015-0026-2. 78, 87

Stubenrauch, C. J., W. B. Rossow, S. Kinne, S. A. Ackerman, G. V. Cesana, H. Chepfer, L. Di Girolamo, B. Getzewich, A. Guignard, A. K. Heidinger, B. C. Maddux, W. P. Menzel, P. Minnis, C. Pearl, S. Platnick, C. Poulsen, J. C. Riedi, S. Sun-Mack, A. Walther, D. M. Winker, S. Zeng, and G. Zhao (2013), Assessment of Global

Cloud Datasets from Satellites: Project and Database Initiated by the GEWEX Radiation Panel, *Bulletin of the American Meteorological Society*, *94*(7), 1031–1049, doi: 10.1175/BAMS-D-12-00117.1. 1

Sullivan, S. C., C. Hoose, A. Kiselev, T. Leisner, and A. Nenes (2018), Initiation of secondary ice production in clouds, *Atmospheric Chemistry and Physics*, *18*(3), 1593–1610, doi:10.5194/acp-18-1593-2018. 9, 11, 42, 46

Sun, C., A. Shrivastava, S. Singh, and A. Gupta (2017), Revisiting Unreasonable Effectiveness of Data in Deep Learning Era, in *Proceedings of the IEEE international conference on computer vision*. 25

Sun, F., A. Hall, and X. Qu (2011), On the relationship between low cloud variability and lower tropospheric stability in the Southeast Pacific, *Atmospheric Chemistry and Physics*, *11*(17), 9053–9065, doi:10.5194/ACP-11-9053-2011. 4

Sun, Z., and K. P. Shine (1994), Studies of the radiative properties of ice and mixed-phase clouds, *Quarterly Journal of the Royal Meteorological Society*, *120*(515), 111–137, doi: 10.1002/qj.49712051508. 2, 12

Sundararajan, R., and M. Tjernström (2000), Observations and simulations of a non-stationary coastal atmospheric boundary layer, *Quarterly Journal of the Royal Meteorological Society*, *126*(563), 445–476, doi:10.1002/QJ.49712656305. 5

Takahashi, T., Y. Nagao, and Y. Kushiyama (1995), Possible High Ice Particle Production during Graupel–Graupel Collisions, *Journal of the Atmospheric Sciences*, *52*(24), 4523–4527, doi:10.1175/1520-0469(1995)052⟨4523:PHIPPD⟩2.0.CO;2. 10, 42, 46

Tan, I., and T. Storelvmo (2019), Evidence of Strong Contributions From Mixed-Phase Clouds to Arctic Climate Change, *Geophysical Research Letters*, *46*(5), 2894–2902, doi: 10.1029/2018GL081871. 2, 12, 78, 87, 88

Taylor, P. C., S. Kato, K. Xu, and M. Cai (2015), Covariance between Arctic sea ice and clouds within atmospheric state regimes at the satellite footprint level, *Journal of Geophysical Research: Atmospheres*, *120*(24), 12,656–12,678, doi:10.1002/2015JD023520. 42

Tornow, F., A. S. Ackerman, and A. M. Fridlind (2021), Preconditioning of overcast-to-broken cloud transitions by riming in marine cold air outbreaks, *Atmospheric Chemistry and Physics*, *21*(15), 12,049–12,067, doi:10.5194/acp-21-12049-2021. 13, 48, 75, 83, 84

Trenberth, K. E., J. T. Fasullo, and J. T. Kiehl (2009), Earth's global energy budget, *Bulletin of the American Meteorological Society*, *90*(3), 311–323, doi:10.1175/2008BAMS2634.1. 1

Twohy, C. H., P. J. DeMott, L. M. Russell, D. W. Toohey, B. Rainwater, R. Geiss, K. J. Sanchez, S. Lewis, G. C. Roberts, R. S. Humphries, C. S. McCluskey, K. A. Moore, P. W. Selleck, M. D. Keywood, J. P. Ward, and I. M. McRobert (2021), Cloud-Nucleating Particles over the Southern Ocean in a Changing Climate, *Earth's future*, *9*(3), 21, doi:10.1029/2020EF001673. 78, 88

Twomey, S. (1974), Pollution and the planetary albedo, *Atmospheric Environment (1967)*, *8*(12), 1251–1256, doi:10.1016/0004-6981(74)90004-3. 4

Twomey, S. (1977), The Influence of Pollution on the Shortwave Albedo of Clouds, *Journal of the Atmospheric Sciences*, *34*(7), 1149–1152, doi:10.1175/1520-0469(1977)034⟨1149:TIOPOT⟩2.0.CO;2. 4

Vali, G. (1985), Nucleation terminology, *Bulletin of the American Meteorological Society*, *66*(11), 1426–1427. 9

Vali, G., P. J. DeMott, O. Möhler, and T. F. Whale (2015), Technical Note: A proposal for ice nucleation terminology, *Atmospheric Chemistry and Physics*, *15*(18), 10,263–10,270, doi:10.5194/acp-15-10263-2015. 9

Van Der Dussen, J. J., S. R. De Roode, and A. P. Siebesma (2016), How large-scale subsidence affects stratocumulus transitions, *Atmos. Chem. Phys*, *16*, 691–701, doi:10.5194/acp-16-691-2016. 3, 5

van der Walt, S., J. L. Schönberger, J. Nunez-Iglesias, F. Boulogne, J. D. Warner, N. Yager, E. Gouillart, and T. Yu (2014), Scikit-image: Image processing in python, *PeerJ*, *2014*(1), e453, doi:10.7717/PEERJ.453/FIG-5. 31

Vergara-Temprado, J., B. J. Murray, T. W. Wilson, D. O'Sullivan, J. Browse, K. J. Pringle, K. Ardon-Dryer, A. K. Bertram, S. M. Burrows, D. Ceburnis, P. J. Demott, R. H. Mason, C. D. O'Dowd, M. Rinaldi, and K. S. Carslaw (2017), Contribution of feldspar and marine organic aerosols to global ice nucleating particle concentrations, *Atmospheric Chemistry and Physics*, *17*(5), 3637–3658, doi:10.5194/acp-17-3637-2017. 44

Villanueva, D., F. Senf, and I. Tegen (2021), Hemispheric and Seasonal Contrast in Cloud Thermodynamic Phase From A-Train Spaceborne Instruments, *Journal of Geophysical Research: Atmospheres*, *126*(6), 1–12, doi:10.1029/2020JD034322. 18

Vincent, L., and P. Soille (1991), Watersheds in Digital Spaces: An Efficient Algorithm Based on Immersion Simulations, *IEEE TRANSACTIONS ON PATTERN ANALYSIS AND MACHINE INTELLIGENCE*, *13*(6), 583. 29

Vonnegut, B. (1947), The Nucleation of Ice Formation by Silver Iodide, *Journal of Applied Physics*, *18*(7), 593–595, doi:10.1063/1.1697813. 9

Wall, C. J., T. Kohyama, and D. L. Hartmann (2017), Low-cloud, boundary layer, and sea ice interactions over the Southern Ocean during winter, *Journal of Climate*, *30*(13), 4857–4871, doi:10.1175/JCLI-D-16-0483.1. 42

Wall, C. J., T. Storelvmo, J. R. Norris, and I. Tan (2022), Observational Constraints on Southern Ocean Cloud-Phase Feedback, *Journal of Climate*, *35*(15), 5087–5102, doi:10.1175/JCLI-D-21-0812.1. 78, 87

Wang, H., and G. Feingold (2009a), Modeling Mesoscale Cellular Structures and Drizzle in Marine Stratocumulus. Part II: The Microphysics and Dynamics of the Boundary Region between Open and Closed Cells, *Journal of the Atmospheric Sciences*, *66*(11), 3257–3275, doi:10.1175/2009jas3120.1. 8

Wang, H., and G. Feingold (2009b), Modeling mesoscale cellular structures and drizzle in marine stratocumulus. Part I: Impact of drizzle on the formation and evolution of open cells, *Journal of the Atmospheric Sciences*, *66*(11), 3237–3256, doi:10.1175/2009JAS3022.1. 8, 56

Wang, Y., G. M. McFarquhar, R. M. Rauber, C. Zhao, W. Wu, J. A. Finlon, D. M. Stechman, J. Stith, J. B. Jensen, M. Schnaiter, E. Järvinen, F. Waitz, J. Vivekanandan, M. Dixon, B. Rainwater, and D. W. Toohey (2020), Microphysical Properties of Generating Cells Over the Southern Ocean: Results From SOCRATES, *Journal of Geophysical Research: Atmospheres*, *125*(13), doi:10.1029/2019JD032237. 49

Wang, Z., D. Vane, G. Stephens, and D. Reinke (2013), CloudSat Project: Level 2 combined radar and lidar cloud scenario classification product process description and interface control document, *California Institute of Technology, Calif*, p. 61. 12

Warren, S. G., C. J. Hahn, J. London, R. M. Chervin, and R. L. Jenne (1986), Global Distribution of Total Cloud Cover and Cloud Type Amounts Over Land, *NCAR Technical Notes*, doi:10.5065/D6GH9FXB. 3

Warren, S. G., C. H. Hahn, J. London, R. M. Chervin, and R. L. Jenne (1988), Global Distribution of Total Cloud Cover and Cloud Type Amounts Over the Ocean, *NCAR Technical Notes*, doi:10.5065/D6QC01D1. 3

Wegener, A. (1911), *Thermodynamik der Atmosphäre*, 1–331 pp., J. A. Barth, Leipzig. 11

Welch, B. L. (1938), The Significance of the Difference Between Two Means when the Population Variances are Unequal, *Biometrika*, *29*(3/4), 350, doi:10.2307/2332010. 35

Welch, B. L. (1947), The Generalization of 'Student's' Problem when Several Different Population Variances are Involved, *Biometrika*, *34*(1/2), 28–35. 35

Westbrook, C. D., and A. J. Illingworth (2011), Evidence that ice forms primarily in supercooled liquid clouds at temperatures >-27 °C, *Geophysical Research Letters*, *38*(14), doi:10.1029/2011GL048021. 9, 12

Wood, R. (2005), Drizzle in Stratiform Boundary Layer Clouds. Part I: Vertical and Horizontal Structure, *Journal of the Atmospheric Sciences*, *62*(9), 3011–3033, doi:10.1175/JAS3529.1. 3

Wood, R. (2007), Cancellation of Aerosol Indirect Effects in Marine Stratocumulus through Cloud Thinning, *Journal of the Atmospheric Sciences*, *64*(7), 2657–2669, doi:10.1175/JAS3942.1. 3

Wood, R. (2012), Stratocumulus Clouds, *Monthly Weather Review*, *140*(8), 2373–2423, doi:10.1175/MWR-D-11-00121.1. 1, 2, 3, 4, 5, 68

Wood, R., and C. S. Bretherton (2004), Boundary layer depth, entrainment, and decoupling in the cloud-capped subtropical and tropical marine boundary layer, *Journal of Climate*, *17*(18), 3576–3588, doi:10.1175/1520-0442(2004)017⟨3576:BLDEAD⟩2.0.CO;2. 2, 68

Wood, R., and C. S. Bretherton (2006), On the relationship between stratiform low cloud cover and lower-tropospheric stability, *Journal of Climate*, *19*(24), 6425–6432, doi:10.1175/JCLI3988.1. 4, 5

Wood, R., and D. L. Hartmann (2006), Spatial variability of liquid water path in marine low cloud: The importance of mesoscale cellular convection, *Journal of Climate*, *19*(9), 1748–1764, doi:10.1175/JCLI3702.1. 1, 4, 5, 7, 14, 18, 28, 54, 56, 57, 59, 61, 69, 70, 71, 77, 79, 80, 83, 86

Wood, R., K. K. Comstock, C. S. Bretherton, C. Cornish, J. Tomlinson, D. R. Collins, and C. W. Fairall (2008), Open cellular structure in marine stratocumulus sheets, *Journal of Geophysical Research*, *113*(12), 1–16, doi:10.1029/2007JD009371. 49

Wood, R., C. S. Bretherton, D. Leon, A. D. Clarke, P. Zuidema, G. Allen, and H. Coe (2011), An aircraft case study of the spatial transition from closed to open mesoscale

cellular convection over the Southeast Pacific, *Atmospheric Chemistry and Physics*, *11*(5), 2341–2370, doi:10.5194/acp-11-2341-2011. 5, 8, 50

Xiao, H., C. M. Wu, and C. R. Mechoso (2010), Buoyancy reversal, decoupling and the transition from stratocumulus to shallow cumulus topped marine boundary layers, *Climate Dynamics*, *37*(5), 971–984, doi:10.1007/S00382-010-0882-3/FIGURES/8. 5

Xu, G., M. Schnaiter, and E. Järvinen (2022), Accurate Retrieval of Asymmetry Parameter for Large and Complex Ice Crystals From In-Situ Polar Nephelometer Measurements, *Journal of Geophysical Research: Atmospheres*, *127*(3), 1–19, doi:10.1029/2021JD036071. 16

Xue, H., G. Feingold, and B. Stevens (2008), Aerosol Effects on Clouds, Precipitation, and the Organization of Shallow Cumulus Convection, *Journal of the Atmospheric Sciences*, *65*(2), 392–406, doi:10.1175/2007JAS2428.1. 5, 8

Yamaguchi, T., and G. Feingold (2015), On the relationship between open cellular convective cloud patterns and the spatial distribution of precipitation, *Atmospheric Chemistry and Physics*, *15*(3), 1237–1251, doi:10.5194/acp-15-1237-2015. 2, 8, 78, 87

Yorks, J. E., P. A. Selmer, A. Kupchock, E. P. Nowottnick, K. E. Christian, D. Rusinek, N. Dacic, and M. J. McGill (2021), Aerosol and cloud detection using machine learning algorithms and space-based lidar data, *Atmosphere*, *12*(5), doi:10.3390/atmos12050606. 31

Young, G., P. J. Connolly, C. Dearden, and T. W. Choularton (2018), Relating large-scale subsidence to convection development in Arctic mixed-phase marine stratocumulus, *Atmospheric Chemistry and Physics*, *18*(3), 1475–1494, doi:10.5194/acp-18-1475-2018. 5, 50, 79

Yuan, T., H. Song, R. Wood, J. K. C. Mohrmann, K. G. Meyer, L. Oreopoulos, and S. Platnick (2020), Applying Deep Learning to NASA MODIS Data to Create a Community Record of Marine Low Cloud Mesoscale Morphology, *Atmospheric Measurement Techniques Discussions*, pp. 1–16, doi:10.5194/amt-2020-61. 19, 59, 72, 73, 79, 80, 81, 97, 98, 99

Zaremba, T. J., R. M. Rauber, G. M. McFarquhar, P. J. DeMott, J. J. D'Alessandro, and W. Wu (2021), Ice in Southern Ocean Clouds With Cloud Top Temperatures Exceeding -5 °C, *Journal of Geophysical Research: Atmospheres*, *126*(14), 1–13, doi:10.1029/2021JD034574. 37, 75, 84

Zelinka, M. D., S. A. Klein, and D. L. Hartmann (2012), Computing and partitioning cloud feedbacks using cloud property histograms. Part II: Attribution to changes in cloud amount, altitude, and optical depth, *Journal of Climate*, *25*(11), 3736–3754, doi: 10.1175/JCLI-D-11-00249.1. 2, 13

Zelinka, M. D., S. A. Klein, K. E. Taylor, T. Andrews, M. J. Webb, J. M. Gregory, and P. M. Forster (2013), Contributions of different cloud types to feedbacks and rapid adjustments in CMIP5, *Journal of Climate*, *26*(14), 5007–5027, doi:10.1175/JCLI-D-12-00555.1. 2, 13

Zelinka, M. D., T. A. Myers, D. T. McCoy, S. Po-Chedley, P. M. Caldwell, P. Ceppi, S. A. Klein, and K. E. Taylor (2020), Causes of Higher Climate Sensitivity in CMIP6 Models, *Geophysical Research Letters*, *47*(1), doi:10.1029/2019GL085782. 2, 13, 77, 78, 87

Zhang, D., T. Luo, D. Liu, and Z. Wang (2014), Spatial scales of altocumulus clouds observed with collocated CALIPSO and CloudSat measurements, *Atmospheric Research*, *148*, 58–69, doi:10.1016/j.atmosres.2014.05.023. 43

Zhang, D., D. Liu, T. Luo, Z. Wang, and Y. Yin (2015), Aerosol impacts on cloud thermodynamic phase change over East Asia observed with CALIPSO and CloudSat measurements, *Journal of Geophysical Research: Atmospheres*, *120*(4), 1490–1501, doi: 10.1002/2014JD022630. 43

Zhang, D., Z. Wang, T. Luo, Y. Yin, and C. Flynn (2017), The occurrence of ice production in slightly supercooled Arctic stratiform clouds as observed by ground-based remote sensors at the ARM NSA site, *Journal of Geophysical Research*, *122*(5), 2867–2877, doi:10.1002/2016JD026226. 18

Zhang, D., Z. Wang, P. Kollias, A. M. Vogelmann, K. Yang, and T. Luo (2018), Ice particle production in mid-level stratiform mixed-phase clouds observed with collocated A-Train measurements, *Atmospheric Chemistry and Physics*, *18*(6), 4317–4327, doi: 10.5194/acp-18-4317-2018. 18

Zhou, X., A. S. Ackerman, A. M. Fridlind, and P. Kollias (2018), Simulation of mesoscale cellular convection in marine stratocumulus. Part I: Drizzling conditions, *Journal of the Atmospheric Sciences*, *75*(1), 257–274, doi:10.1175/JAS-D-17-0070.1. 9, 50

Zhou, X., R. L. Atlas, I. L. McCoy, C. S. Bretherton, C. G. Bardeen, A. Gettelman, P. Lin, and Y. Ming (2021), Evaluation of Cloud and Precipitation Simulations in CAM6 and AM4 Using Observations Over the Southern Ocean, *Earth and Space Science*, *8*(2), doi:10.1029/2020EA001241. 56, 57, 61, 83

Acknowledgments

First and foremost, I want to express my greatest gratitude to my supervisor Anna Possner. Not only for providing me with this exciting and interesting research topic, but especially for the support, motivation, and discussions throughout this thesis. Thank you so much for your guidance and, nonetheless, for granting me the freedom to pursue my own ideas. I sincerely appreciate working with you! I also thank my second supervisor Corinna Hoose, especially for accepting to review this thesis on such a short notice.

Further, I wish to thank Odran Sourdeval for helping me with the technical details of satellite retrievals. In particular, you shaped this dissertation by introducing me to the DARDAR product. I am very grateful to have had the opportunity to spend one week with you at the University of Lille and for the cultural experience of northern French cuisine. I also want to thank, Robert Wood and Isabel McCoy, for allowing me to use the MCC data set and for the discussions about my results and conclusions. Moreover, I am glad to have had the possibility to meet you two and Ryan Eastman in person at the AGU 2022 in Chicago, even though this thesis was mostly remote due to COVID-19. I especially enjoyed the great discussion with Isabel, Ryan, and Anna, during the AGU, providing me with new ideas and motivation for the final months of this dissertation.

Special thanks to all members of our group: Veeramanikandan Ramadoss, Christopher Reichel, Kevin Pfannkuch, Luise Schulte, and Lianet Hernández Pardo. Veera, I genuinely appreciate you joining the group and sharing the office with me, making the building less lonely. I only wish it could have lasted longer. I am really glad we had at least the weekly remote coffee breaks. But even more, I enjoyed being back at the office and having lunch with all of you. Talking about vacations, discussing science or political topics, and forgetting time. I thank all of you for the great and friendly working atmosphere!

The people, I am more than grateful for are my family! Without you, I would not be where I am today! I especially thank my parents, Bettina and Dieter Kern, for their support, encouragement, and help throughout my life, and my sister, Bianca Kern, who always reminds me of what I have already accomplished (when I forget). Last but not least, I thank my husband Finn Danker. You always have an open ear and are supportive, give me advice when I need it, and celebrate with me when things work out! Finally, I thank my son, Jonas, while probably being the least actively helpful, you always calm me and make me smile and for letting me sleep through most nights!